On the geometry of fracture and frustration
Koning, V.

Cover Page

The handle http://hdl.handle.net/1887/29873 holds various files of this Leiden University dissertation.

Author: Koning, Vinzenz
Title: On the geometry of fracture and frustration
Issue Date: 2014-11-26

ON THE GEOMETRY OF FRACTURE AND FRUSTRATION

PROEFSCHRIFT

ter verkrijging van
de graad van Doctor aan de Universiteit Leiden,
op gezag van Rector Magnificus prof. mr. C.J.J.M. Stolker,
volgens besluit van het College voor Promoties
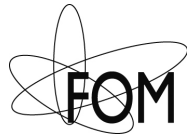te verdedigen op woensdag 26 november 2014
klokke 11:15 uur

door

VINZENZ KONING

GEBOREN TE HAARLEMMERMEER IN 1988

P R O M O T I E C O M M I S S I E

Promotor:	prof. dr. M. L. van Hecke
Copromotor:	dr. V. Vitelli
Overige leden:	prof. dr. A. Achúcarro
	prof. dr. C. W. J. Beenakker
	prof. dr. E. R. Eliel
	prof. dr. A. Fernandez-Nieves (Georgia Institute of Technology)
	dr. L. Giomi
	prof. dr. W. T. M. Irvine (University of Chicago)

CONTENTS

INTRODUCTION

1.1 GEOMETRIC FRUSTRATION

Whether it concerns biological matter such as membranes, DNA and viruses, or synthesised anisotropic colloidal particles, the deformations inherent to soft matter almost inevitably call for a geometric description. Therefore, the use of geometry has always been essential in our understanding of the physics of soft matter. However, only recently has geometry turned into an instrument for the design and engineering of novel materials. Key concepts are geometrical frustration and the topological defects that are often a consequence of this frustration [81, 72, 37, 6].

Geometrical frustration refers to the impossibility of local order to propagate throughout a chosen space. This impossibility is of geometric nature and could for instance be due to the topology of the space. Probably your first and most familiar encounter with this phenomenon was while playing (association) football. The mathematically inclined amongst you may have wandered off during the game and wondered: "Why does the ball contain hexagonal *and* pentagonal panels?" The ball cannot contain hexagonal panels only: a perfect tiling of hexagons (an example of local order) cannot be achieved on the spherical surface (the space considered). There exists a constraint on the number of faces, F, edges, E, and vertices, V. The constraint is named after Euler and reads [65]

$$F - E + V = \chi, \tag{1}$$

where χ is the Euler characteristic. The Euler characteristic is a quantity insensitive to continuous deformations of the surface of the ball such as twisting and bending. We call such quantities topological. Only if one would perform violent operations such as cutting a hole in the sphere and glueing a handle to the hole would a surface of differently topology be created [65, 69]. For a surface with one handle $\chi = 0$, just as for a torus or a coffee mug. The Euler characteristic χ equals 2 for the spherical surface of the ball. Thus, Euler's polyhedral formula (eq. (1)) ensures

the need of 12 pentagonal patches besides the hexagonal ones, no matter how well inflated the ball is. To see this, write the number of faces F as the sum of the number of hexagons, H, and pentagons, P, i.e. $F = H + P$. One edge is shared by two faces, hence $E = \frac{1}{2}(6H + 5P)$. Moreover, each vertex is shared among three faces, hence $V = \frac{1}{3}(6H + 5P)$. Substituting the expressions for F, E and V into eq. (1) yields $P = 12$. These pentagons are the defects. Similarly, protein shells of spherical viruses which enclose the genetic material consist of pentavalent and hexavalent subunits [9, 52]. Another condensed matter analog of the geometrically frustrated football is the 'colloidosome'. Colloidosomes are spherical colloidal crystals [21, 4, 34] that are of considerable interest as microcapsules for delivery and controlled release of drugs [21].

Figure 1: *Left panel:* Geometric frustration in a football. A perfect tiling of hexagonal panels cannot be achieved everywhere, resulting in black pentagonal panels (defects). *Right panel:* Geometric frustration on the globe. The lines of latitude shrink to a point at the north and south poles (defects). Adapted from ref. [1].

Another common example of geometric frustration are the lines of latitude on the surface of a globe. The points where these lines shrink to a point, that is, the North and South Poles, are the defects. Just like the pentagons on the football, the defects on the globe are also required by a topological constraint, namely the Poincare-Hopf theorem [69]:

$$\sum_a s_a = \chi. \tag{2}$$

The lines of latitude circle once around both poles. Hence, there are two defects with a unit winding number, s. (See section 1.5 for a more precise definition.) Similar to the lines of longitude and latitude on the globe, a coating of a nanoparticle with a monolayer of ordered tilted molecules also has two polar defects [58, 57, 70, 105, 20]. Recently, Stellacci and co-workers have been able to functionalise the defects to assemble linear chains of nanoparticles [20]. A nematic liquid crystal coating possesses four defects at the vertices of a regular tetrahedron in the ground state [57]. Attaching chemical linkers to these defects could result in a three-dimensional diamond structure [70], rather than a one-dimensional chain. Functionalisation of the defects, thus resulting from ordered structures confined to curved spaces, offers an intriguing route to directed assembly.

The types of order that we will discuss in this introductory chapter are crystalline and nematic liquid crystalline (1.2). After introducing mathematical preliminaries in section 1.3, we will discuss the elasticity of crystals and liquid crystals (section 1.4) and give a classification of the defects in these phases of matter (section 1.5). We will elucidate the role of geometry in this subject. In particular, we will explicitly show that, in contrast to the two examples given in the introduction, a topological constraint is not necessary for geometric frustration. In section 1.6 we will review coupling between defects and curvature. Nematic order on the sphere is discussed in section 1.7.

This thesis is outlined thoroughly in section 1.8. Subsections 1.8.1 and 1.8.2 (corresponding to Part I and II, respectively) are about nematic liquid crystals confined to various geometries. In some aspects a nematic liquid crystal behaves like a liquid. Indeed, one can capture a nematic in the form of droplets or in containers of various shapes, just as one can do that for liquid water. At the same time nematic liquid crystals exhibit, just as crystals, anisotropy: in a nematic the molecules self-organise. Our goal in Part I and II is to explore avenues to control this molecular assembly geometrically by tuning the shape of the boundary of the nematic liquid crystal. Our interest in part III (subsection 1.8.3) is the integrity and failure of curved materials. It may, for instance, be very relevant to know under which conditions a colloidosome fractures. Part III discusses crack growth in curved elastic films.

1.2 LIQUID CRYSTALS

Besides the familiar solid, liquid and gas phases, there exist other fascinating forms of matter, which display phenomena with order intermediate between conventional isotropic fluids and crystalline solids. These are therefore called liquid crystalline or mesomorphic phases [18, 95]. Let us consider the difference between a solid crystal and a liquid crystal. In a solid crystal all the constituents are located in a periodic fashion, such that only specific translations return the same lattice. Moreover, the bonds connecting neighbouring crystal sites define a discrete set of vectors which are the same throughout the system. In a crystal, there is thus both bond-orientational and translational order. In liquid crystals there is orientational order, as the anisotropic constituent molecules define a direction in space, but the translational order is partially or fully lost. The latter phase, in which there is no translational order whatsoever, is called a nematic liquid crystal. The mobility of the translationally disordered molecules is responsible for the fluidic properties of nematic liquid crystals.

1.3 DIFFERENTIAL GEOMETRY OF SURFACES

1.3.1 *Preliminaries*

For a thorough introduction to the differential geometry of surfaces, please consult refs. [97, 17, 37]. In this section we will introduce the topic briefly and establish the notation. Points on a curved surface embedded in the three dimensional world we live in can be described by a three-component vector $\mathbf{R}\left(\mathbf{x}\right)$ as a function of the coordinates $\mathbf{x} = \left(x^1, x^2\right)$. Vectors tangent to this surface are given by

$$\mathbf{t}_\alpha = \partial_\alpha \mathbf{R}, \tag{3}$$

where $\partial_\alpha = \frac{\partial}{\partial x^\alpha}$ is the partial derivative with respect to x^α. These are in in general neither normalised nor orthogonal. However, it does provide a basis in which to express an arbitrary tangent vector $\mathbf{n}$ in:

$$\mathbf{n} = n^\alpha \mathbf{t}_\alpha. \tag{4}$$

Here we have used the Einstein summation convention, *i.e.*, an index occurring twice in a single term is summed over, provided that one of the them is a lower (covariant) index and the other is an upper (contravariant) index. We reserve Greek characters α, β, $\gamma, \ldots$ as indices for components of vectors and tensors tangent to the surface. The so-called metric tensor reads

$$g_{\alpha\beta} = \mathbf{t}_\alpha \cdot \mathbf{t}_\beta, \tag{5}$$

and its inverse is defined by

$$g^{\alpha\beta} g_{\beta\gamma} = \delta^\alpha_\gamma, \tag{6}$$

where δ^α_γ is equal to one if $\alpha = \gamma$ and zero otherwise. We can lower and raise indices with the metric tensor and inverse metric tensor, respectively, in the usual way, *e.g.*

$$g_{\alpha\beta} n^\alpha = n_\beta \tag{7}$$

It is straightforward to see that the inner product between two vectors $\mathbf{n}$ and $\mathbf{m}$ is

$$\mathbf{n} \cdot \mathbf{m} = n^\alpha \mathbf{t}_\alpha \cdot m^\beta \mathbf{t}_\beta = g_{\alpha\beta} n^\alpha m^\beta = n^\alpha m_\alpha. \tag{8}$$

The area of the parallelogram generated by the infinitesimal vectors $dx^1 \mathbf{t}_1$ and $dx^2 \mathbf{t}_2$, is given by the magnitude of their cross product, and yields the area element

$$
\begin{aligned}
dS &= \left| dx^1 \mathbf{t}_1 \times dx^2 \mathbf{t}_2 \right| \\
&= \sqrt{(\mathbf{t}_1 \times \mathbf{t}_2)^2} dx^1 dx^2 \\
&= \sqrt{|\mathbf{t}_1|^2 |\mathbf{t}_2|^2 - (\mathbf{t}_1 \cdot \mathbf{t}_2)^2} dx^1 dx^2 \\
&= \sqrt{g_{11} g_{22} - g_{12} g_{21}} dx^1 dx^2 \\
&= \sqrt{g} d^2 x,
\end{aligned}
\tag{9}
$$

where $g = \det(g_{\alpha\beta})$, the determinant of the metric tensor, and $d^2 x$ is shorthand for $dx^1 dx^2$. More generally, the magnitude of the cross product of two vectors $\mathbf{m}$ and $\mathbf{n}$ is

$$|\mathbf{m} \times \mathbf{n}| = \left| \gamma_{\alpha\beta} m^\alpha n^\beta \right|, \tag{10}$$

which introduces the antisymmetric tensor

$$\gamma_{\alpha\beta} = \sqrt{g} \epsilon_{\alpha\beta}, \tag{11}$$

where $\epsilon_{\alpha\beta}$ is the Levi-Civita symbol satisfying $\epsilon_{12} = -\epsilon_{21} = 1$ and is zero otherwise.

Since we will encounter tangent unit vectors, *e.g.* indicating the orientation of some physical quantity, it is convenient to decompose this vector in a set of orthonormal tangent vectors, $\mathbf{e}_1\left(\mathbf{x}\right)$ and $\mathbf{e}_2\left(\mathbf{x}\right)$, such that

$$\mathbf{e}_i \cdot \mathbf{e}_j = \delta_{ij} \quad \text{and} \quad \mathbf{N} \cdot \mathbf{e}_i = 0, \tag{12}$$

alternative to the basis defined in eq. 3. Here $\mathbf{N}$ is the vector normal to the surface. We use the Latin letters i, j and k for the components of vectors expressed in this orthonormal basis. As they are locally Cartesian, they do not require any administration of the position of the index. Besides the area element, we need a generalisation of the partial derivative. This generalisation is the covariant derivative, D_α, the projection of the derivative onto the surface. The covariant derivative of $\mathbf{n}$ expressed in the orthonormal basis reads in component form [37]

$$\begin{aligned} D_\alpha n_i &= \mathbf{e}_i \cdot \partial_\alpha \mathbf{n} \\ &= \mathbf{e}_i \cdot \partial_\alpha n_j \mathbf{e}_j + \mathbf{e}_i \cdot \partial_\alpha \mathbf{e}_j n_j \\ &= \partial_\alpha n_i + \epsilon_{ij} A_\alpha n_j, \end{aligned} \tag{13}$$

where $\epsilon_{ij} A_\alpha = \mathbf{e}_i \cdot \partial_\alpha \mathbf{e}_j$ is called the spin-connection. The final line is justified because the derivative of any unit vector is perpendicular to this unit vector. More generally, the covariant derivative of the vector $\mathbf{n}$ along x^α is [17]

$$D_\alpha n^\beta = \partial_\alpha n^\beta + \Gamma^\beta_{\alpha\gamma} n^\gamma, \tag{14}$$

where the Christoffel symbols are

$$\Gamma^\alpha_{\beta\gamma} = \frac{1}{2} g^{\alpha\delta} \left(\partial_\gamma g_{\beta\delta} + \partial_\beta g_{\delta\gamma} - \partial_\delta g_{\beta\gamma} \right). \tag{15}$$

Finally, with the antisymmetric tensor and the area element in hand we can state a useful formula in integral calculus, namely Stokes' theorem

$$\int d^2 x \sqrt{g} \gamma^{\alpha\beta} D_\alpha n_\beta = \oint dx^\alpha n_\alpha. \tag{16}$$

1.3.2 *Curvature*

The curvature is the deviation from flatness and therefore a measure of the rate of change of the tangent vectors along the normal,

or, put the other way around, a measure of the rate of change of the normal along the tangent vectors. This can be cast in a curvature tensor defined as

$$K_{\alpha\beta} = \mathbf{N} \cdot \partial_\beta \mathbf{t}_\alpha = -\mathbf{t}_\beta \cdot \partial_\alpha \mathbf{N}. \tag{17}$$

From this tensor we extract the intrinsic Gaussian curvature

$$G = \det\left(K_\beta^\alpha\right) = \frac{1}{2}\gamma^{\alpha\gamma}\gamma^{\beta\delta}K_{\alpha\beta}K_{\gamma\delta} = \kappa_1\kappa_2, \tag{18}$$

and extrinsic mean curvature

$$H = \frac{1}{2}\mathrm{Tr}\left(K_\beta^\alpha\right) = \frac{1}{2}g^{\alpha\beta}K_{\alpha\beta} = \frac{1}{2}\left(\kappa_1 + \kappa_2\right), \tag{19}$$

where $\kappa_1 = \mathbf{N} \cdot \partial_1 \tilde{\mathbf{e}}_1$ and $\kappa_2 = \mathbf{N} \cdot \partial_2 \tilde{\mathbf{e}}_2$ are the extremal or principal curvatures, the curvature in the principal directions $\tilde{\mathbf{e}}_1$ and $\tilde{\mathbf{e}}_2$. These eigenvalues and eigenvectors can be obtained by diagonalising the matrix associated with the curvature tensor. If at a point on a surface κ_1 and κ_2 have the same sign, the Gaussian curvature is positive and from the outsiders' point of view the surface curves away in the same direction whichever way you go, as is the case on mountaintops, or peaks and in valleys. In contrast, if at a point on a surface κ_1 and κ_2 have opposite signs the Gaussian curvature is negative, the saddle-like surface curves away in opposite directions. The magnitude of κ_1 and κ_2 is equal to the inverse of the radius of the tangent circle in the principal direction (Fig. 2). It turns out that the Gaussian curvature and the spin-connection are related. We will see how in a moment by considering the normal (third) component of the curl (denoted by $\nabla\times$) of the spin-connection

$$\begin{aligned}
(\nabla \times \mathbf{A})_3 &= \epsilon_{3jk}\partial_j\left(\mathbf{e}_1 \cdot \partial_k\mathbf{e}_2\right) \\
&= \epsilon_{3jk}\partial_j\mathbf{e}_1 \cdot \partial_k\mathbf{e}_2 \\
&= \epsilon_{3jk}\left(\mathbf{N} \cdot \partial_j\mathbf{e}_1\right)\left(\mathbf{N} \cdot \partial_k\mathbf{e}_2\right),
\end{aligned} \tag{20}$$

where we have used the product rule and the antisymmetry of ϵ_{ijk} in the second equality sign. The final line is justified by the fact that the derivative of a unit vector is perpendicular to itself and therefore we have *e.g.* $\partial_j\mathbf{e}_1 = \left(\mathbf{N} \cdot \partial_j\mathbf{e}_1\right)\mathbf{N} + \left(\mathbf{e}_2 \cdot \partial_j\mathbf{e}_1\right)\mathbf{e}_2$. If we now with the aid of eqs. (17) and (18) note that

$$G = \left(\mathbf{N} \cdot \partial_1\mathbf{e}_1\right)\left(\mathbf{N} \cdot \partial_2\mathbf{e}_2\right) - \left(\mathbf{N} \cdot \partial_1\mathbf{e}_2\right)\left(\mathbf{N} \cdot \partial_2\mathbf{e}_1\right), \tag{21}$$
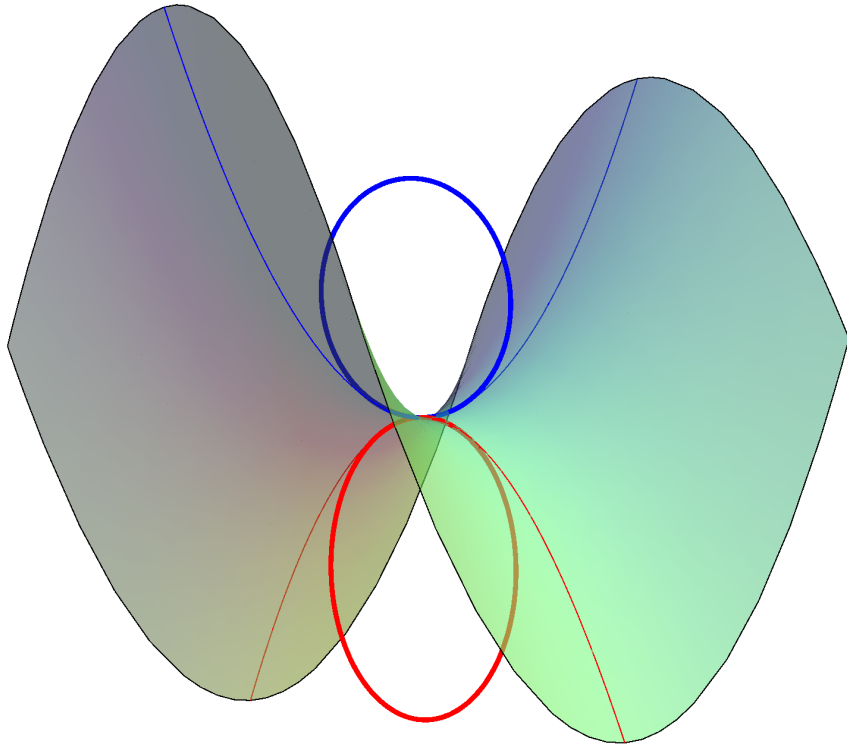
Figure 2: A saddle surface has negative Gaussian curvature, as κ_1 and κ_2 have different signs. The magnitudes of the curvatures κ_1 and κ_2 are given by the inverse radii of the tangent circles drawn in blue and red.

we easily see that the normal component of the curl of the spin-connection equals the Gaussian curvature:

$$(\nabla \times \mathbf{A}) \cdot \mathbf{N} = G, \tag{22}$$

or alternatively [73]

$$\gamma^{\alpha\beta} D_\alpha A_\beta = G. \tag{23}$$

This geometric interpretation of $\mathbf{A}$ will show its importance in section 1.4, where we will comment on its implications on the geometric frustration in curved nematic liquid crystal films.

Finally, a popular choice of parametrisation of the surface is the Monge gauge or height representation in which $\mathbf{x} = (x, y)$ and $\mathbf{R} = (x, y, f(x, y))$, where $f(x, y)$ is the height of the surface

above the xy-plane. In this representation the Gaussian curvature reads

$$G = \frac{\det \partial_\alpha \partial_\beta f}{g}, \tag{24}$$

where the determinant of the metric is given by

$$g = 1 + (\partial_x f)^2 + (\partial_y f)^2. \tag{25}$$

1.4 ELASTICITY ON CURVED SURFACES AND IN CONFINED GEOMETRIES

1.4.1 *Elasticity of a two-dimensional nematic liquid crystal*

In a nematic liquid crystal the molecules (assumed to be anisotropic) tend to align parallel to a common axis. The direction of this axis is labeled with a unit vector, $\mathbf{n}$, called the director (see Fig. 3). The states $\mathbf{n}$ and $-\mathbf{n}$ are equivalent. Any spatial distortion of a uniform
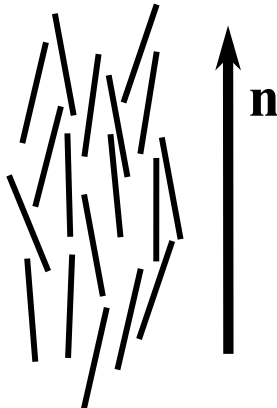
Figure 3: The director $\mathbf{n}$ specifies the average local orientation of the nematic molecules.

director field costs energy. If we assume that these deformations are small on the molecular length scale, l,

$$|\partial_i n_j| \ll \frac{1}{l}, \tag{26}$$

we can construct a phenomenological continuum theory. The resulting Frank free energy F for a two dimensional flat nematic liquid crystal reads [18, 39, 40]

$$F = \frac{1}{2} \int d^2 x \left[k_1 \left(\partial_i n_i \right)^2 + k_3 \left(\epsilon_{ij} \partial_i n_j \right)^2 \right], \tag{27}$$

where the splay and bend elastic constants, k_1 and k_3 respectively, measure the energy of the two independent distortions shown in Fig. 4. To simplify the equations, one often makes the assumption
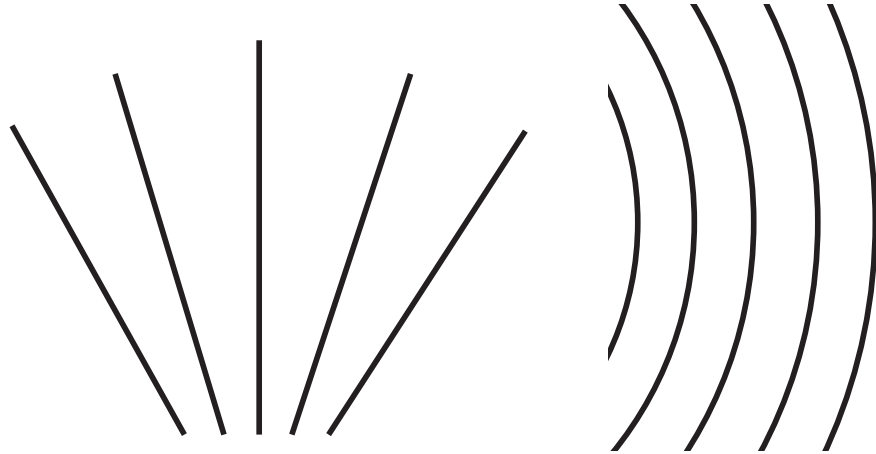
Figure 4: Conformations with (left panel) a non-vanishing divergence of the director and (right panel) a non-vanishing curl of the director.

of isotropic elasticity. In this approximation the Frank elastic constants are equal, $k_1 = k_3 = k$, and up to boundary terms the free energy reduces to [39]

$$F = \frac{1}{2}k \int d^2x \partial_i n_j \partial_i n_j. \tag{28}$$

When the coupling of the director to the curvature tensor $K_{\alpha\beta}$ [82, 38, 36, 26, 62, 84, 67, 66, 68] is ignored, the elastic free energy on a curved surface generalises to [58, 78, 70, 104, 105]

$$F = \frac{1}{2}k \int d^2x \sqrt{g} D_\alpha n^\beta D^\alpha n_\beta. \tag{29}$$

In this equation the area element has become $dS = d^2x\sqrt{g}$ and partial derivatives have been promoted to covariant derivatives. Because the director is of unit length, we can conveniently specify it in terms of its angle with a local orthonormal reference frame, $\Theta(\mathbf{x})$, as follows

$$\mathbf{n} = \cos\Theta\, \mathbf{e_1} + \sin\Theta\, \mathbf{e_2}. \tag{30}$$

Then, since $\partial_\alpha n_1 = -\sin\Theta\, \partial_\alpha\Theta = -n_2\partial_\alpha\Theta$ and similarly $\partial_\alpha n_2 = \cos\Theta\, \partial_\alpha\Theta = n_1\partial_\alpha\Theta$ we see that

$$\partial_\alpha n_i = -\epsilon_{ij}n_j\partial_\alpha\Theta, \tag{31}$$

with which we find the covariant derivative to be

$$D_\alpha n_i = -\epsilon_{ij} n_j \left(\partial_\alpha \Theta - A_\alpha \right). \tag{32}$$

Therefore, we can rewrite the elastic energy as [73]

$$F = \frac{1}{2} k \int d^2 x \sqrt{g} \left(\partial_\alpha \Theta - A_\alpha \right) \left(\partial^\alpha \Theta - A^\alpha \right), \tag{33}$$

where we have used that $\left(-\epsilon_{ij} n_j \right) \left(-\epsilon_{ij} n_j \right) = \delta_{jk} n_j n_k = \cos^2 \left(\Theta \right) + \sin^2 \left(\Theta \right) = 1$. This form of the free energy clearly shows that nematic order on a curved surface is geometrically frustrated. The topological constraints of the introductory section are merely a special example of the frustration of local order due to the geometric properties of the system. Note that for a curved surface without such a topological constraint (*e.g.* a Gaussian bump) the ground state can be a deformed director field. Since the curl of the spin-connection equals the Gaussian curvature (eq. (23)), if the Gaussian curvature is nonzero, the spin-connection is irrotational and cannot be written as the gradient of a scalar field, $A_\alpha \neq \partial_\alpha \Theta$, just like the magnetic field cannot be described by a scalar field either. Therefore, F in eq. (33) is nonzero and we can conclude that there is geometric frustration present in the system.

1.4.2 *Elasticity of a two-dimensional solid*

Similar to the construction of the continuum elastic energy of a nematic liquid crystal, we can write down the elastic energy of a linear elastic solid as an integral of terms quadratic in the deformations, *i.e.* strain. This strain is found in the following way. Consider a point $\mathbf{x} = (x, y, 0)$ on an initially flat solid. This point is displaced to $\mathbf{x}'(\mathbf{x}) = (x', y', f)$ in the deformed solid, and so we may define a displacement vector $\mathbf{u}(\mathbf{x}) = \mathbf{x}' - \mathbf{x} = u_x \mathbf{e}_x + u_y \mathbf{e}_y + f \mathbf{e}_z$. The square of the line element in the deformed plate is then given by $ds'^2 = (dx + du_x)^2 + (dx + du_x)^2 + df^2$. Noting that $du_x = \partial_i u_x dx_i$ with $x_i = x, y$ and similarly for u_y and f we find [44]

$$ds'^2 = ds^2 + 2u_{ij} dx_i dx_j. \tag{34}$$

Thus, the strain tensor $u_{ij}(\mathbf{x})$ encodes how infinitesimal distances change in the deformed body with respect to the resting state of the solid and reads

$$u_{ij} = \frac{1}{2} \left(\partial_i u_j + \partial_j u_i + A_{ij} \right), \tag{35}$$

where we have omitted non-linear terms of second order in $\partial_i u_j$ and where the tensor field $A_{ij}(\mathbf{x})$ is now defined as

$$A_{ij} \equiv \partial_i f \partial_j f. \tag{36}$$

We will assume that curvature plays its part only through this coupling of gradients of the displacement field to the geometry of the surface, and we will therefore adopt the flat space metric. This is a valid approximation for moderately curved solids, as we comment on at the end of the section [107, 6]. To leading order in gradients of the height function, A_{ij} is related to the curvature by (see eq. (24))

$$-\frac{1}{2}\epsilon_{ik}\epsilon_{jl}\partial_k\partial_l A_{ij} = \det\left(\partial_i\partial_j f\right) = G. \tag{37}$$

Isotropy of the solid leaves two independent scalar combinations of u_{ij} that contribute to the stretching energy [44]:

$$F = \frac{1}{2}\int dS \left(2\mu u_{ij}^2 + \lambda u_{ii}^2\right). \tag{38}$$

The elastic constants λ and μ are called the Lamé coefficients. Minimisation of this energy with respect to u_j leads to the force balance equation:

$$\partial_i\sigma_{ij} = 0, \tag{39}$$

where the stress tensor $\sigma_{ij}(\mathbf{x})$ is defined by Hooke's law

$$\sigma_{ij} = 2\mu u_{ij} + \lambda\delta_{ij}u_{kk}. \tag{40}$$

The force balance equation can be solved by introducing the Airy stress function, $\chi(\mathbf{x})$, which satisfies

$$\sigma_{ij} = \epsilon_{ik}\epsilon_{jl}\partial_k\partial_l\chi, \tag{41}$$

since this automatically gives

$$\partial_i\sigma_{ij} = \epsilon_{jk}\partial_k\left[\partial_1,\partial_2\right]\chi = 0 \tag{42}$$

by the commutation of the partial derivatives. If one does not adopt the flat space metric, the covariant generalisation of the force balance equation is not satisfied, because the the commutator of the covariant derivatives, known as the Riemann curvature tensor, does not vanish. It is actually proportional to the Gaussian curvature and indicates why the range of validity of this approach is limited to moderately curved surfaces [107, 6]. Finally, for small $\partial_i u_j$ the bond angle field, $\Theta(\mathbf{x})$, is given by

$$\Theta = \frac{1}{2}\epsilon_{ij}\partial_i u_j. \tag{43}$$

1.4.3 *Elasticity of a three-dimensional nematic liquid crystal*

Besides splay and bend, there are two other deformations possible in a three-dimensional nematic liquid crystal. They are twist and saddle-splay, measured by elastic moduli K_2 and K_{24}. Twist refers to a helical type of deformation for which the rotation of $\mathbf{n}$ has a component along $\mathbf{n}$. The analog of eq. (27) reads

$$
\begin{aligned}
F[\mathbf{n}\,(\mathbf{x})] = \frac{1}{2} \int dV \Big(&K_1 \left(\nabla \cdot \mathbf{n} \right)^2 \\
&+ K_2 \left(\mathbf{n} \cdot \nabla \times \mathbf{n} \right)^2 + K_3 \left(\mathbf{n} \times \nabla \times \mathbf{n} \right)^2 \Big) \\
&- K_{24} \int \mathbf{dS} \cdot \left(\mathbf{n} \nabla \cdot \mathbf{n} + \mathbf{n} \times \nabla \times \mathbf{n} \right).
\end{aligned}
\tag{44}
$$

The integration of the splay, twist and bend energy density is over the volume to which the nematic is confined. The saddle-splay energy per unit volume is a pure divergence term, hence the saddle-splay energy can be written as the surface integral in eq. (44). In addition to the energy in eq. (44), there is an energetic contribution coming from the interfacial interactions, often larger in magnitude. Therefore, the anchoring of the nematic molecules at the boundary can be taken as a constraint. In one of the possible anchoring conditions the director is forced to be tangential to the surface, yet free to rotate in the plane. In this case of planar degenerate boundary conditions, we derive in chapter 4 that the saddle-splay energy reduces to

$$
F_{24} = K_{24} \int dS \left(\kappa_1 n_1^2 + \kappa_2 n_2^2 \right),
\tag{45}
$$

thus coupling the director to the curvature of the boundary surface.

1.5 TOPOLOGICAL DEFECTS

Topological defects are characterised by a small region where the order is not defined. Topological defects in translationally ordered media, such as crystals, are called *dislocations*. Defects in the orientational order, such as in nematic liquid crystals and again crystals, are called *disclinations*. The defects are topological when they cannot be removed by a continuous deformation of the order parameter. As we will see momentarily, they are classified according to a topological quantum number or topological charge, a quantity

that may only take on a discrete set of values and which can be measured on any circuit surrounding the defect.

1.5.1 *Disclinations in a nematic*

Consider for concreteness a two-dimensional nematic liquid crystal. A singularity in the director field is an example of a disclination. Such a point defect can be classified by its winding number, strength, or topological charge, s, which is the number of times the director rotates by 2π, when following one closed loop in counterclockwise direction around the singularity:

$$\oint d\Theta = \oint dx^\alpha \partial_\alpha \Theta = 2\pi s. \tag{46}$$

We can express eq. (46) in differential form by invoking Stokes' theorem:

$$\gamma^{\alpha\beta} D_\alpha \partial_\beta \Theta = q\delta\left(\mathbf{x} - \mathbf{x}_a\right), \tag{47}$$

where we use an alternative labelling, $q = 2\pi s$, of the charge of the defect, which is located at $\mathbf{x}_a$. The delta-function obeys

$$\delta\left(\mathbf{x} - \mathbf{x}_a\right) = \frac{\delta\left(x^1 - x_a^1\right)\delta\left(x^2 - x_a^2\right)}{\sqrt{g}}, \tag{48}$$

such that the integral over the surface yields one. The far-field contribution of the defect to the angular director in a flat plane reads

$$\Theta = s\phi + c, \tag{49}$$

as it forms a solution to the Euler-Lagrange equation of the elastic free energy:

$$\partial^2 \Theta = 0. \tag{50}$$

Here, ϕ is the azimuthal angle and c is just a phase. Examples are presented in Fig. 5. Note that since the states $\mathbf{n}$ and $-\mathbf{n}$ are equivalent, defects with half-integer strength are also possible. In fact, it is energetically favourable for an $s = 1$ defect to unbind into two $s = \frac{1}{2}$ defects [70, 75].

These defects can be detected experimentally by crossed-polarised microscopy. The image will appear black there where the director

(a) $s = 1$, $c = 0$

(b) $s = 1$, $c = \frac{\pi}{4}$

(c) $s = 1$, $c = \frac{\pi}{2}$

(d) $s = \frac{1}{2}$, $c = 0$
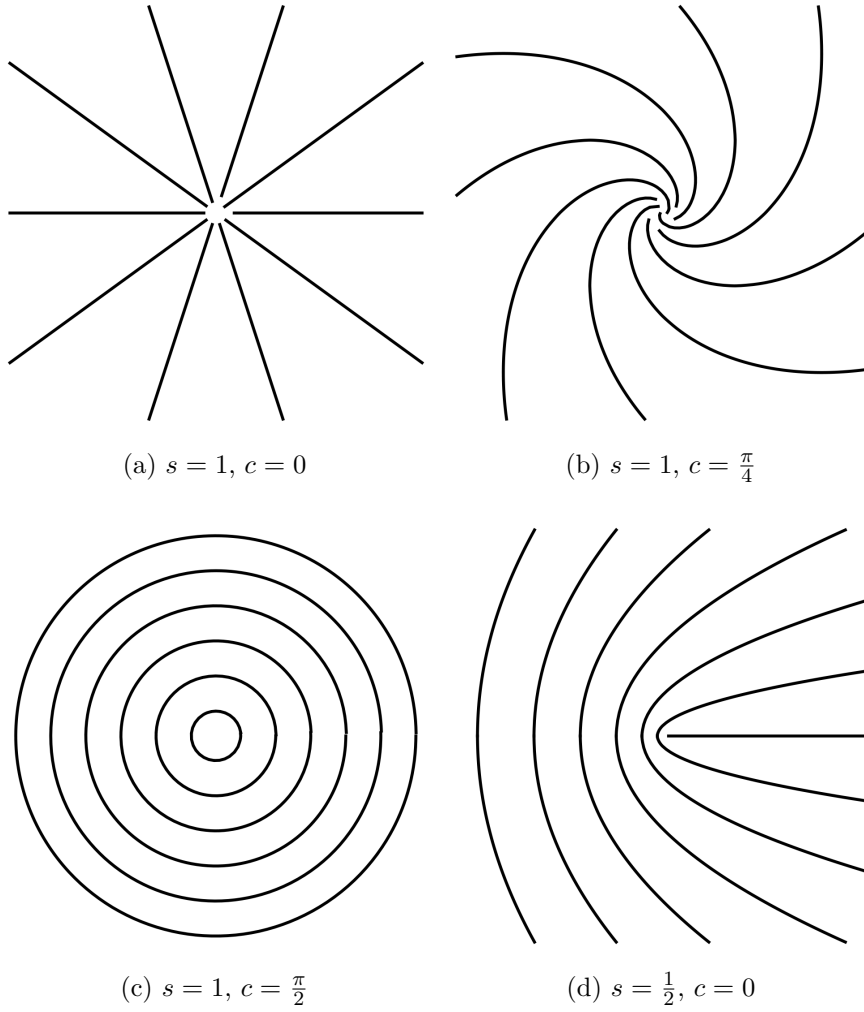
Figure 5: Director configurations, $n_1 = \cos\Phi$, $n_2 = \sin\Phi$, for disclinations of strength s and constant c.

is aligned with one of the polarisers (and thus perpendicular to the other polariser). Therefore, there are two black (and two coloured) brushes meeting at an $s = \pm 1/2$ defect. There are four black (and four coloured) brushes meeting at an $s = \pm 1$ defect.

1.5.2 *Disclinations in a crystal*

Though energetically more costly, disclinations also arise in two-dimensional crystals. At these points, the coordination number deviates from its ordinary value, which is six for a crystal on a triangular lattice. Just like in nematic liquid crystals, disclinations in crystals are labelled by a topological charge, q, which is the angle

over which the vectors specifying the lattice directions rotate when following a counterclockwise circuit around the disclination. If we parametrise these lattice direction vectors with $\Theta\left(\mathbf{x}\right)$, the bond-angle field, this condition reads mathematically

$$\oint d\Theta = q. \tag{51}$$

Thus for disclinations in a triangular lattice with five-fold and seven-fold symmetry, as displayed in Fig. 6, $q = \frac{\pi}{3}$ and $q = -\frac{\pi}{3}$ respectively. Analogous to eq. (47), the flat-space differential form
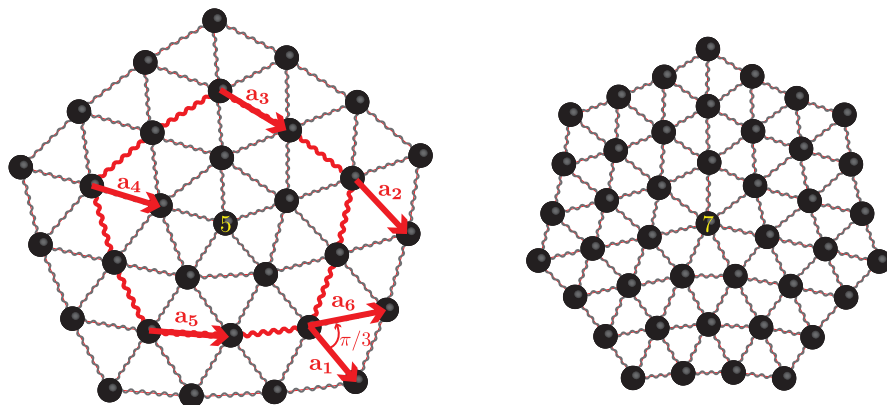
Figure 6: (Left panel) Five-fold and (right panel) seven-fold disclination. When following a closed counterclockwise loop (red) around the five-fold disclination, the initial lattice vector $\mathbf{a}_1$ rotates via $\mathbf{a}_2$, $\mathbf{a}_3$, $\mathbf{a}_4$ and $\mathbf{a}_5$ over an angle of $\pi/3$ to $\mathbf{a}_6$.

of eq. (51) for a disclination located at $\mathbf{x}_a$ reads

$$\epsilon_{ij}\partial_i\partial_j\Theta = q\delta\left(\mathbf{x} - \mathbf{x}_a\right). \tag{52}$$

1.5.3 *Dislocations*

Besides disclinations, dislocations can occur in crystals. Dislocations are characterised by a Burgers vector $\mathbf{b}$. This vector measures the change in the displacement vector, if we make a counterclockwise loop surrounding the dislocation,

$$\oint d\mathbf{u} = \mathbf{b}. \tag{53}$$

Just as the strength of disclinations can only take values from a discrete set, the Burgers vector of a dislocation is equal to some integer multiple of a lattice vector. Also note that a dislocation
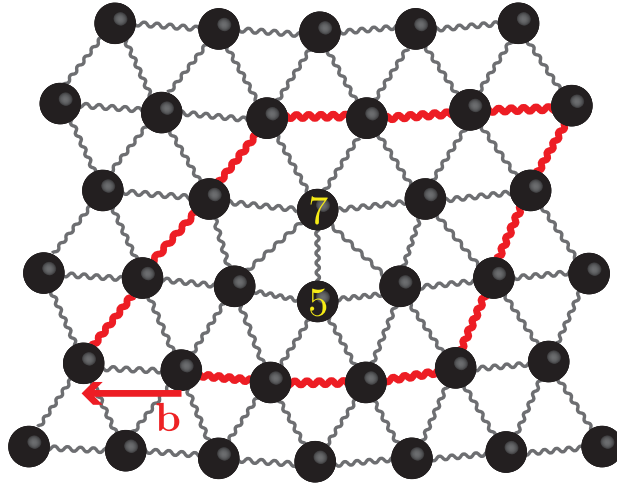
Figure 7: Dislocation in a triangular lattice. The Burgers vector spec-
ifies by how much a clockwise circuit (marked in red, bold)
around the dislocation fails to close. A dislocation can be
viewed as disclination dipole with a moment perpendicular
to its Burgers vector.

can be viewed as a pair of closely spaced disclinations of opposite
charge [71], as can be seen in Fig. 7.

The flat-space differential form of eq. (53) for a dislocation at
$\mathbf{x}_a$ is

$$\epsilon_{ij}\partial_i\partial_j u_k = b_k \delta\left(\mathbf{x} - \mathbf{x}_a\right), \tag{54}$$

which again can be obtained by using Stokes' theorem.

1.6 INTERACTION BETWEEN CURVATURE AND DEFECTS

1.6.1 *Coupling in liquid crystals*

It is possible to recast the free energy in terms of the locations
of the topological defects rather than the director or displacement
field, if smooth (*i.e.* non-singular) deformations are ignored. In
this case the energy in eq. (33) is minimised with respect to Θ,
which leads to

$$D^\alpha\left(\partial_\alpha\Theta - A_\alpha\right) = 0. \tag{55}$$

This needs to supplemented with an equation for the effective
charge distribution:

$$\gamma^{\alpha\beta} D_\alpha\left(\partial_\beta\Theta - A_\beta\right) = \rho - G, \tag{56}$$

obtained by combining eq. (23) for the curvature and eq. (47) for the defect density $\rho\left(\mathbf{x}\right)$,

$$\rho = \sum_a q_a \delta\left(\mathbf{x} - \mathbf{x}_a\right). \tag{57}$$

Eq. (55) is automatically satisfied if one chooses [104]

$$\partial_\alpha \Theta - A_\alpha = \gamma_\alpha{}^\beta \partial_\beta \chi, \tag{58}$$

where $\chi\left(\mathbf{x}\right)$ is an auxiliary function. At the same time, substituting eq. (58) into eq. (56) leads to

$$-D^2 \chi = \rho - G. \tag{59}$$

The source in this Poisson equation contains both topological point charges as well as the Gaussian curvature with opposite sign. The analog of the electrostatic potential is χ. The role of the electric field is played by $\partial_\alpha \chi$. Indeed, substituting eq. (58) in eq. (33), shows that the energy density is proportional to the square of the electric field:

$$F = \frac{1}{2}k \int dS \partial_\alpha \chi \partial^\alpha \chi. \tag{60}$$

Next, we formally solve eq. (59)

$$\chi = -\int dS' \Gamma_L\left(\mathbf{x}, \mathbf{x}'\right)\left(\rho\left(\mathbf{x}'\right) - G\left(\mathbf{x}'\right)\right), \tag{61}$$

where $\Gamma_L\left(\mathbf{x}, \mathbf{x}'\right)$ is the Green function of the Laplace-Beltrami operator, $D^2 = D_\alpha D^\alpha$, satisfying

$$D^2 \Gamma_L\left(\mathbf{x}, \mathbf{x}'\right) = \delta\left(\mathbf{x} - \mathbf{x}'\right). \tag{62}$$

Integrating eq.(60) by parts and substituting our expressions for χ and the Laplacian of χ (eqs. (61) and (59) respectively) results (up to boundary terms) in

$$F = -\frac{k}{2} \int dS \int dS' \left(\rho\left(\mathbf{x}\right) - G\left(\mathbf{x}\right)\right) \Gamma_L\left(\mathbf{x}, \mathbf{x}'\right) \left(\rho\left(\mathbf{x}'\right) - G\left(\mathbf{x}'\right)\right), \tag{63}$$

from which we again deduce the analogy with two-dimensional electrostatics. In this analogy the defects are electric point sources with their electric charge equal to the topological charge q and the Gaussian curvature with its sign reversed is a background charge

distribution. Therefore the defects will be attracted towards regions of Gaussian curvature with the same sign as the topological charge [58, 7, 104, 106, 113, 35, 84, 100]. Such screening will be perfect if $S = \rho$ everywhere, since $F = 0$ then. However, unless the surface contains singularities in the Gaussian curvature, like the apex of a cone, perfect screening will be impossible, as the topological charge is quantised whereas the Gaussian curvature is typically smoothly distributed.

1.6.2 *Coupling in crystals*

Note that an *arbitrary* field χ solves eq. (42). However, χ must be physically possible and we therefore need to accompany eq. (42) with another equation, which we will obtain by considering the inversion of eq. (40) [44, 85]:

$$u_{ij} = \frac{1+\nu}{Y}\sigma_{ij} - \frac{\nu}{Y}\sigma_{kk}\delta_{ij} \tag{64}$$

$$= \frac{1+\nu}{Y}\epsilon_{ik}\epsilon_{jl}\partial_k\partial_l\chi - \frac{\nu}{Y}\partial^2\chi\delta_{ij} \tag{65}$$

where the two-dimensional Young's modulus, Y, and Poisson ratio, ν, are given by

$$Y = \frac{4\mu\left(\mu+\lambda\right)}{2\mu+\lambda}, \tag{66}$$

$$\nu = \frac{\lambda}{2\mu+\lambda}. \tag{67}$$

Applying $\epsilon_{ik}\epsilon_{jl}\partial_k\partial_l$ to eq. (65) gives

$$\frac{1}{Y}\partial^4\chi = \epsilon_{ik}\epsilon_{jl}\partial_k\partial_l u_{ij}. \tag{68}$$

By invoking eqs. (35), (43), the differential expressions for the defects, namely eqs. (54) and (52), as well as eq. (37) for the curvature, one can rewrite the right hand side to arrive at the crystalline analog of eq. (59):

$$\frac{1}{Y}\partial^4\chi = \rho - G, \tag{69}$$

where the defect distribution, ρ, of disclinations with charge q_a and dislocations with Burgers vector $\mathbf{b}^b$ reads

$$\rho = \sum_a q_a\delta\left(\mathbf{x} - \mathbf{x}_a\right) + \sum_b \epsilon_{ij}b_i^b\partial_j\delta\left(\mathbf{x} - \mathbf{x}_b\right). \tag{70}$$

We can also rewrite the free energy (up to boundary terms) in terms of the Airy stress function as follows:

$$F = \frac{1}{2Y} \int dS \left(\partial^2 \chi\right)^2.$$
(71)

If we integrate this by parts twice and use eq. (69) to eliminate χ and $\partial^4 \chi$, we find (up to boundary terms)

$$F = \frac{Y}{2} \int dS \int dS' \left(\rho\left(\mathbf{x}\right) - G\left(\mathbf{x}\right)\right) \Gamma_B \left(\mathbf{x}, \mathbf{x}'\right) \left(\rho\left(\mathbf{x}'\right) - G\left(\mathbf{x}'\right)\right)$$
(72)

where Γ_B is the Greens function of the biharmonic operator

$$\partial^4 \Gamma_B \left(\mathbf{x}, \mathbf{x}'\right) = \delta\left(\mathbf{x} - \mathbf{x}'\right).$$
(73)

Eq. (72) is the crystalline analog of eq. (63). Again, the defects can screen the Gaussian curvature. The interaction, however, is different than the Coulomb interaction in the liquid crystalline case. If the surface is allowed to bend, disclinations will induce buckling, illustrated in Fig. 8 with paper models. In these cones, the integrated Gaussian curvature is determined by the angular deficit of the disclination

$$\int dS G = q.$$
(74)

If there are no topological defects (implying that $\rho = 0$ in eq. (69)), but the curvature still provides a source of stress of the Airy stress function χ^G:

$$\frac{1}{Y} \partial^4 \chi^G = -G.$$
(75)

One can solve this equation in two steps. First, we make use of an auxiliary function U obeying

$$\partial^2 U = G.$$
(76)

This leaves the following equation to be solved (*i.e.* the second step)

$$\frac{1}{Y} \partial^2 \chi^G = -U + U_H,$$
(77)

where U_H is a harmonic function (*i.e.* satisfying $\partial^2 U_H = 0$) introduced to fulfil the boundary conditions [107].
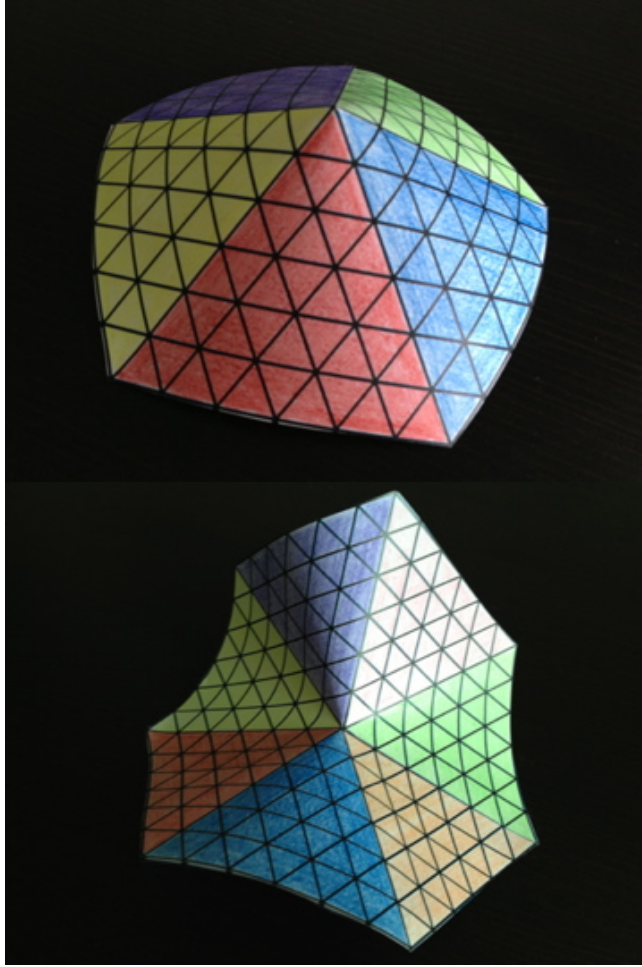
Figure 8: Paper models illustrating the coupling between disclinations and curvature. *Top panel:* 5-fold (*Bottom panel*: 7-fold) coordinated particle in a triangular lattice. Positively (negatively) charged disclinations and positive (negative) Gaussian curvature attract.

Surprisingly, charge-neutral dislocations and pleats can also screen the curvature [73, 85, 107, 32, 34]. Pleats are formed by arrays of dislocations and allow for an extra piece of crystal, just like their fabric analogs. Since the opening angle of pleats, approximately equal to $n_d a$ with a the lattice spacing and n_d the dislocation line density can be arbitrarily small, pleats can actually provide a finer screening than quantised disclinations.

1.7 NEMATIC ORDER ON THE SPHERE

As a naive guess for the ground state of a two-dimensional nematic liquid crystal phase on the surface of the sphere, one could imagine the excess of topological charge to be located at the poles, like in the case of tilted molecules on the sphere. However, the order parameter, the director, has the symmetry of a headless arrow instead of a vector. Therefore, this makes it possible for the two $s = 1$ defects to unbind into four $s = \frac{1}{2}$ defects relaxing at the vertices of a regular tetrahedron [57]. The baseball-like nematic texture is illustrated in Fig. 9. The repulsive nature of defects with

Figure 9: The baseball-like ground state of a two-dimensional spherical nematic coating has four $s = \frac{1}{2}$ at the vertices of a tetrahedron in the one-constant approximation. Reprinted figure with permission from ref. [105]. Copyright 2006 by the American Physical Society.

like charges can be seen from the free energy, which, as shown in the previous section, can be reformulated entirely in terms of the defects rather than the director [70, 57]:

$$F = -\frac{\pi k}{2} \sum_{i \neq j} s_i s_j \log\left(1 - \cos\theta_{ij}\right) + E\left(R\right) \sum_j s_j^2. \tag{78}$$

Here, θ_{ij} is the angular separation between defects i and j, *i.e.* $\theta_{ij} = \frac{d_{ij}}{R}$, with d_{ij} being the geodesic distance. The first term yields the long-range interaction of the charges. The second term accounts for the defect self-energy

$$E\left(R\right) = \pi k \log\left(\frac{R}{b}\right) + E_c, \tag{79}$$

where we have imposed a cut-off b representing the defect core size, which has energy E_c. This cut-off needs to be introduced in order to prevent the free energy from diverging. Heuristically, this logarithmically diverging term in the free energy is responsible for the splitting of the two $s = 1$ defects into four $s = \frac{1}{2}$ defects. Two $s = 1$ defects contribute $\left(2 \times 1^2\right) \pi k \log\left(\frac{R}{b}\right) = 2\pi k \log\left(\frac{R}{b}\right)$ to the free energy, whereas four $s = \frac{1}{2}$ defects contribute only $\left(4 \times \left(\frac{1}{2}\right)^2\right) \pi k \log\left(\frac{R}{b}\right) = \pi k \log\left(\frac{R}{b}\right)$.

In addition to this ground state, other defect structures have been observed in computer simulations [23, 90, 88, 3]. If there is a strong anisotropy in the elastic moduli, the four defects are found to lie on a great circle rather than the vertices of a regular tetrahedron [88, 3].

1.8 THIS THESIS

1.8.1 *Spherical nematic shells (part I)*

An experimental model system of spherical nematics is a nematic double emulsion droplet [24, 54, 56, 49, 55, 86, 50, 41, 51]. This is a structure in which a water droplet is captured by a larger nematic liquid crystal droplet, which in turn is dispersed in an outer fluid (Fig. 10). There are some crucial differences between a two-dimensional spherical nematic and a nematic double emulsion droplet. Not only is the nematic coating of a finite thickness, this thickness can be inhomogeneous as a result of buoyancy-driven displacement (or other mechanisms) of the inner droplet out of the centre of the nematic droplet.

Like point disclinations in two dimensions, there exist disclination *lines* in a three-dimensional nematic liquid crystal, which are categorised in similar fashion. However, charge-one lines, and integral lines in general, do not exist. Such lines lose their singular cores [12, 63] by 'escaping in the third dimension'. In shells, such
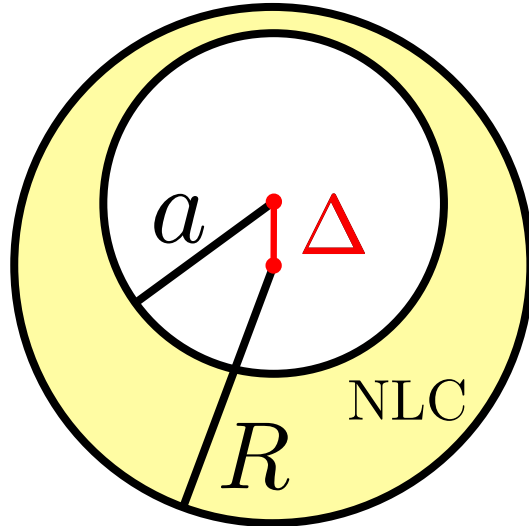
Figure 10: Schematic of a nematic double emulsion droplet of radius R. The inner water droplet of radius a is displaced by an amount Δ along the vertical direction, thereby making the top of the shell thinner.

an escape leads to another type of defect, namely point defects at the interface, known as boojums (Fig. 11).

In a spherical nematic layer of *finite* thickness, the baseball structure with four $s = \frac{1}{2}$ disclination lines spanning the shell, becomes energetically less favourable than two antipodal pairs of boojums beyond a critical thickness [105]. Instead of unbinding, the singular lines escape in the third dimension, leaving two pairs of boojums on the bounding surfaces. This divalent configuration is separated from the tetravalent configuration by a large energy barrier. As a consequence, both configurations are observed in droplets in the same emulsion. Also, trivalent shells with two $s = \frac{1}{2}$ disclination lines and one pair of boojums coexist. In chapter 2 (based on ref. [56]) we study the energetics of thin trivalent shells and find the optimal isosceles arrangement of the defects.

If, in addition, the shell thickness is inhomogeneous, the energy landscape becomes even more complex. As a consequence of the inhomogeneity the defects cluster in the thinnest part of the shell, where the length of the disclination lines (or distance between boojums forming a pair) are shorter. Since the self-energy of the disclination is proportional to its length, it is attracted towards this region of the shell. In chapter 3 (based on refs. [56, 41]), an investigation of thick and inhomogeneous divalent shells shows that
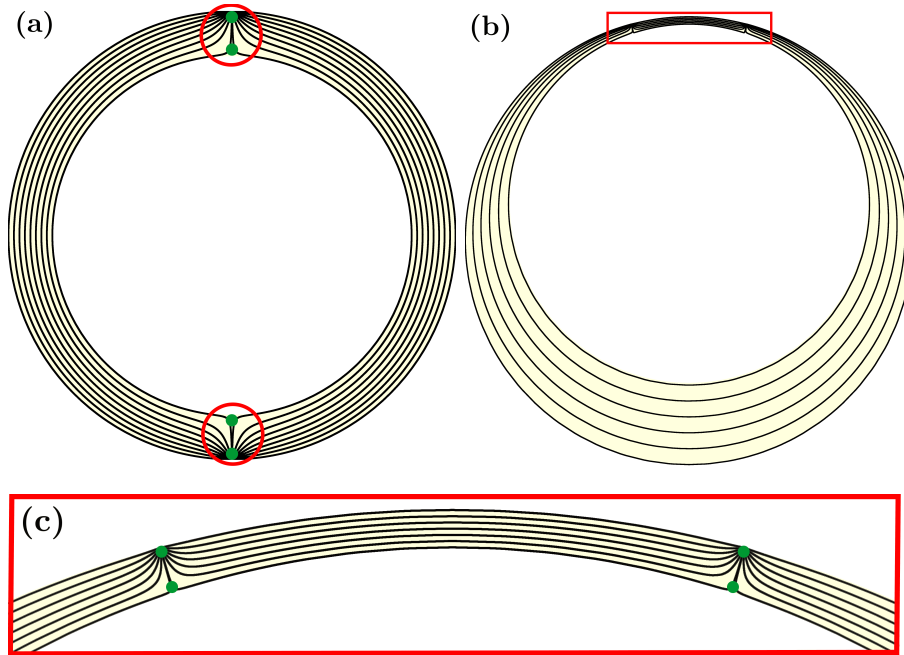
Figure 11: (a) Schematic of the deconfined defect configuration in a homogeneous shell. Two pairs (each encircled in red) of boojums, indicated by green dots, are located at the top and bottom of the shell. (b) Schematic of the confined defect configuration in an inhomogeneous shell. All boojums are located at the thinnest, top part of the shell, inside the red rectangle. (c) Zoom of the thinnest section of the inhomogeneous shell in (b).

pairs of surface defects can make abrupt transitions between the state in which the defects are confined in the thinnest part of the shell, and the deconfined state, in which the interdefect repulsion places them diametrically. These confinement and deconfinement transitions occur when the thickness or thickness inhomogeneity is varied.

1.8.2 *Toroidal nematics (part II)*

The torus has an Euler characteristic equal to zero. Hence, in a nematic droplet of toroidal shape no defects need to be present. The director field to be expected naively in such a geometry is one which follows the tubular axis, as shown in Fig. 12. This achiral director configuration contains only bend energy. In chapter 4 we show, however, that if the toroid becomes too fat it is favourable

to reduce bend deformations by twisting. The price of twisting is screened by saddle-splay deformations provided that $K_{24} > 0$ [77, 42]. The twisted configuration is chiral. Chirality stems from the Greek word for hand, and is indeed in this context easily explained: your right hand cannot be turned into a left hand by moving and rotating it. It is only when viewed in the mirror that your right hand appears to be a left hand and vica versa. Indeed, for small aspect ratios and small values of $(K_2 - K_{24})/K_3$ nematic toroids display either a right- or left-handedness despite the achiral nature of nematics. This phenomenon is recognised as spontaneous chiral symmetry breaking. Typical corresponding plots of the energy as a function of the amount of twist are shown in Fig. 12.
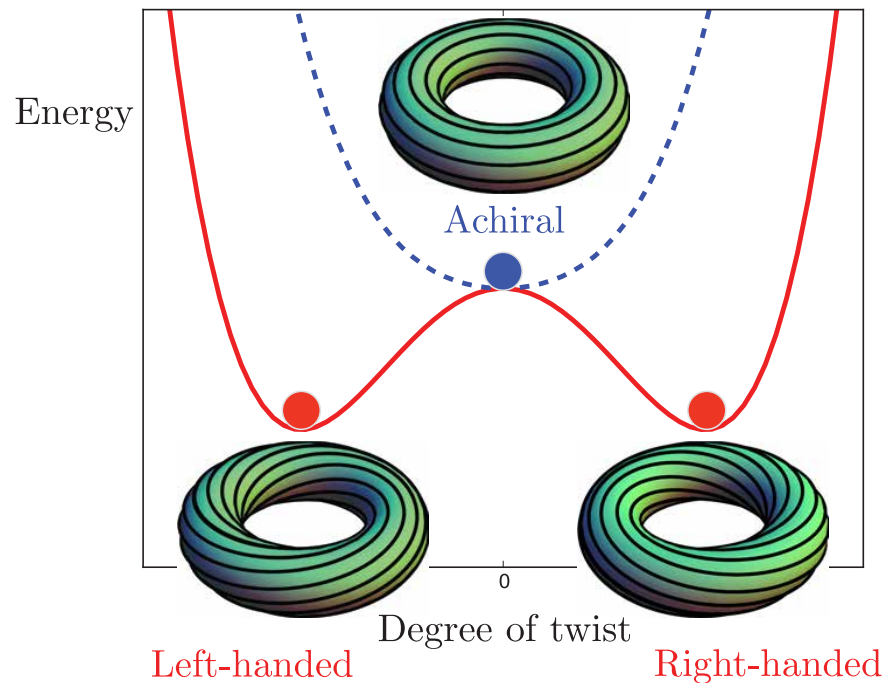
Figure 12: Energy as a function of the degree of twist has either a single achiral minimum (dashed blue) or shows spontaneous chiral symmetry breaking in toroidal nematics (red) depending on the aspect ratio and elastic constants. The chiral state is favoured for fat toroids and small values of $(K_2 - K_{24})/K_3$.

1.8.3 *Cracks in curved solids (part III)*

In chapter 5 we study cracks in curved solids rather than the crystallographic defects discussed in section 1.6.2. We consider an elastic film that is deformed into the shape of a Gaussian bump. The stresses resulting from this geometric frustration affect the onset of crack growth leading to fracture of the body. We find that the critical crack length at which growth begins depends on the location and orientation of the crack. The critical crack size can be decreased by the curvature, but also increased. In chapter 6 we calculate the path that a crack takes for several locations of the initial crack and several aspect ratios of the bump. We find that an incoming crack is deflected from the bump.

Part I

SPHERICAL NEMATICS

We present a theoretical study of the director fields and energetics of spherical nematic liquid crystal shells with degenerate planar boundary conditions. There are divalent, trivalent and tetravalent shells with two, three and four defects at the outer boundary, respectively. For ultrathin trivalent shells, we find that the defects are optimally arranged in an isosceles triangle. We calculate the energy and the stability of this trivalent ground state, and compare this with the tetravalent and divalent defect configurations. For thick divalent shells with two pairs of surface defects, we investigate the effect of thickness inhomogeneity. The pairs of defects can undergo abrupt transitions from a configuration of maximum separation to a state in which the defects are confined to the thinner hemisphere. We construct a phase diagram that maps out the stability and coexistence of these two configurations as a function of shell thickness and thickness inhomogeneity. Our results compare favourably with the experimentally observed transitions in nematic double emulsion droplets and explain their hysteretic character.

THIN SHELLS

2.1 INTRODUCTION

One of today's major drives in condensed matter physics is the assembly of mesoscale particles into complex structures [29]. By creating anisotropy in the interparticle interactions, one can increase the complexity and functionality of these structures. A proposed way to achieve anisotropic interactions is by coating a spherical particle or droplet with an orientationally ordered phase [70]. The topology of the sphere enforces defects in the coating. Since these defects are very distinct regions on the sphere, they are suitable for the attachment of linkers acting as bonds between the particles. For instance, in the case of a vector order parameter, topology requires two defects, creating a particle with two binding sites. In fact, de Vries *et al.* have already assembled such divalent nanoparticle into chains [20]. Nematic rather than vector order allows for defects of charge one-half, referring to the 180 degrees rotation experienced by the local average orientation of the nematic molecules, **n**, when encircling the defect. In fact, it is energetically favourable for defects of charge one to split into two charge one-half defects (Fig. 13a). Nematic order on the sphere has four topological defects of charge one half in its ground state, such that the sum of all charges is equal to 2, the Euler characteristic of the sphere, as demanded by the Poincare-Hopf theorem. Their mutual repulsion drives them as far away from each other as possible: at the vertices of a regular tetrahedron [57]. Thus, chemical functionalisation of the defects in the ground-state of two-dimensional nematic liquid crystal on the sphere would thus result in the diamond structure [70]. In section 3.2, however, we show the results of experimental investigations of nematic shells generated by trapping a water droplet inside a nematic droplet, revealing the existence of shells with valencies of two and three [24, 56, 41], besides the tetravalent shell. In the remainder of this chapter, we will focus on the defect separations (section 2.3), energetics (section 2.4) and fidelity of the
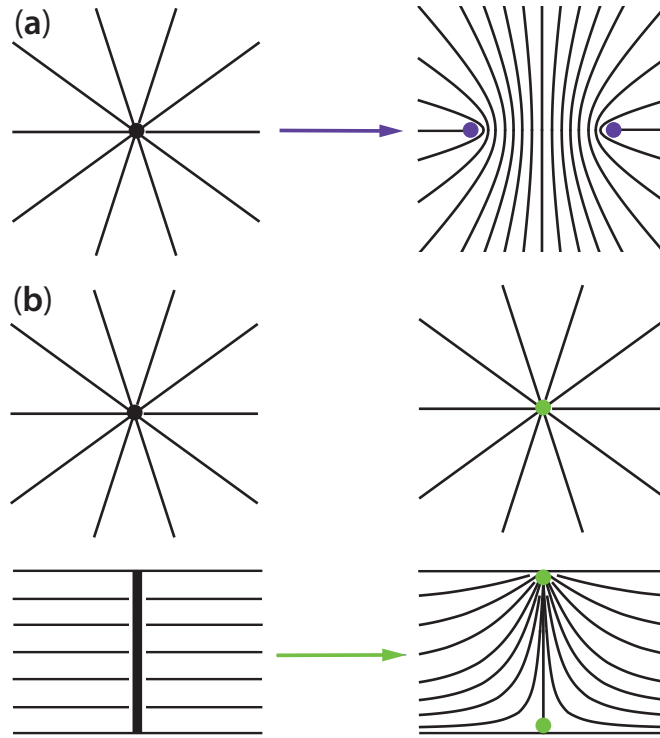
Figure 13: (a) In a two-dimensional nematic a $s = 1$ topological defect (black dot in left panel) can lower its elastic energy by splitting into two $s = 1/2$ defects (purple dots in right panel). (b) A singular line (left panel) spanning the shell with a winding number of one at the boundaries is topologically and energetically unstable. The singular core is indicated by a black dot in the top view shown in the top panel and by the vertical bold line in a cut shown in the bottom panel. One way of reducing the elastic energy escaping in the third (vertical) dimension (right panel), thereby leaving a point defect (green dot), called boojum, on each boundary.

bonds (section 2.5) in thin spherical nematic shells with three-fold valence. We will make a comparison with divalent and tetravalent shells and find the optimal valency as a function of shell thickness as well as the energy barrier between shells of different valency (section 2.4). We will conclude in section 2.6.

2.2 DIVALENT, TRIVALENT AND TETRAVALENT SHELLS

In this section we will present the experiments, performed by Teresa Lopez-Leon and Alberto Fernandez-Nieves, that corrobo-

rate our calculations in this chapter and chapter 3. To fabricate spherical nematic shells, one generates double emulsions with a microcapillary device [103]; these consist of a nematic drop that contains a smaller aqueous drop, all inside an aqueous continuous phase. Both the inner and outer water phases contain 1 wt% polyvinyl alcohol (PVA), which stabilises the emulsion against coalescence and enforces tangential anchoring of the rod-like molecules of the nematic liquid crystal, pentylcyanobiphenyl (5CB). The resulting double-emulsion drops are characterized by an outer radius, R, of around 50 μm and an inner radius, a, that are varied to produce shells of different average thicknesses, $h = R - a$, as schematically shown in Fig. 10. With this microfluidic method the thinnest shells that one can generate have $h \approx 1 \ \mu m$. However, it is possible to significantly reduce this value by increasing the volume of the inner drop once the double emulsion is formed. One achieves this by inducing a difference in osmotic pressure between the inner and outer water phases through the addition of a salt, $CaCl_2$. As pentylcyanobiphenyl has a finite permeability to water, an incoming flow of water from the outer phase can be established if the inner drop contains a higher salt concentration than the outer phase. By controlling this difference, one can control the kinetics of the process and ultimately the thickness of the shells.

Imaging the thinnest shells using optical microscopy and changing the focal plane of our microscope allows for precise determination of the position of the four defects; they are distributed throughout the shell, as shown by the images in Fig. 14a,b and by the schematic diagram in Fig. 14c. To obtain a meaningful value of the angular positions, one determines the position of all defects in a large number of shells with similar inner and outer drop sizes and plot the distribution for the central angle, θ_{ij}, which is the angle subtended by two defects (i and j) with respect to the centre of the drop, and the distribution for the surface angle, α, which is the angle subtended by two defects with respect to another defect. The resulting distributions are both Gaussian; they are centred at $\theta_{ij} = 109°$ and $\alpha = 60°$ and have a width of $\Delta\theta_{ij} = 20°$ and $\Delta\alpha = 12°$, as shown in Fig. 14d,e. The defects are thus located on the vertices of a regular tetrahedron.

There coexist divalent configurations (Fig. 15a,b) which, instead of four charge half defect lines spanning the shell, have two pairs of
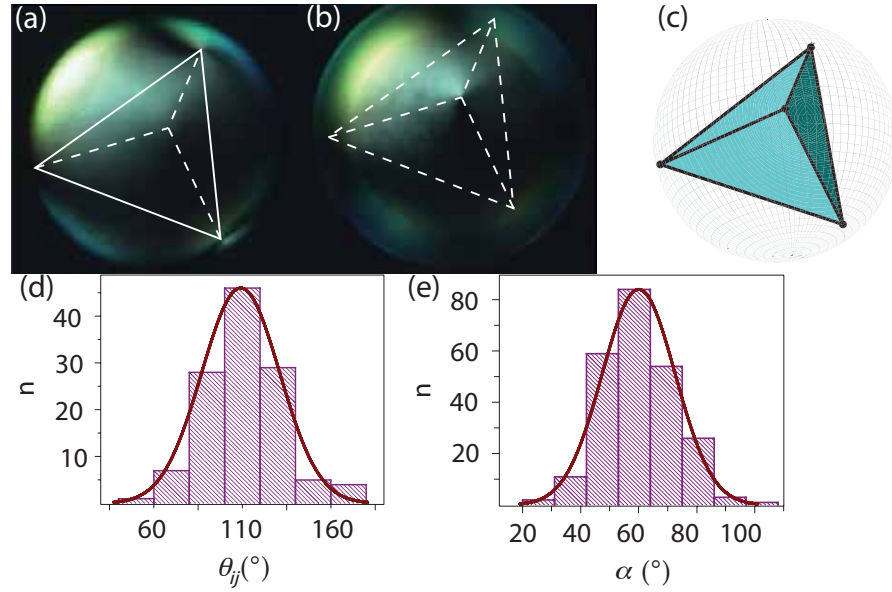
Figure 14: (a), (b) Cross-polarised images of a very thin shell with four $s = 1/2$ defects. In (a), two of the four defects are in focus, whereas in (b) we focus on the upper defect. (c) Schematic diagram of the observed arrangement of the four defects. (d), (e) Histograms for the central angle, θ_{ij}, and the surface angle, α, between defects. Ref. [56].

point defects, called boojums, residing on the boundary surfaces. They arise because the thickness of the nematic coating is nonzero: the elastic energy of a singular line with a winding number of one at the boundary is reduced by escaping in the third dimension, as is illustrated in Fig. 13b. This route thus forms an alternative to splitting into $s = 1/2$ lines spanning the shell. The defects maximise their distance and align, on average, along the diameter of the drop (Fig. 15a,b), as schematically shown in Fig. 15c, and by the central angle distribution in Fig. 15d.

Surprisingly, also structures containing both boojums as well as charge one-half disclination lines coexist (Fig. 16a-c). These defects structures have three-fold valence yet they are still consistent with Poincare-Hopf's theorem, because the total topological charge of the defects at the boundary is $1 + 1/2 + 1/2 = 2$, the Euler characteristic of the sphere. The three defects form an isosceles triangle, where the unequal angle originates from the single $s = 1$ defect, as schematically shown in Fig. 16d. The distribution for the two equal angles is centred at $\alpha_2 = 68°$ and has a width of $\Delta\alpha_2 = 15°$, as shown in Fig. 16e, whereas the distribution of the
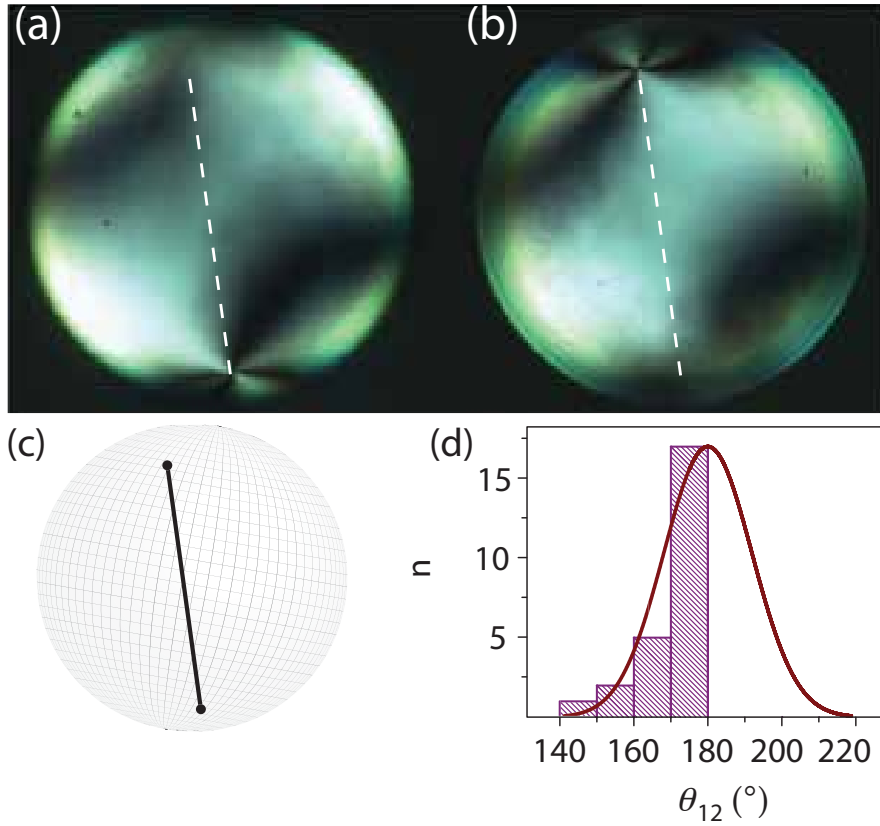
Figure 15: (a), (b) Cross-polarised images of a very thin shell with two $s = 1$ defects. (c) Schematic diagram of the observed arrangement of the two defects. (d) Histogram of the central angle, θ_{12}. Ref. [56].

unequal angle is centred at $\alpha_1 = 46°$ and has a width of $\Delta\alpha_1 = 12°$, as shown in Fig. 16f. Again, also this energetically stable defect configuration arises because of the thickness of the nematic coating is finite, and the energy barrier separating it from other defect structures will be reported in this chapter. The observed isosceles arrangement of the two $s = 1/2$ defects and the $s = 1$ defect is consistent with our calculation of the equilibrium configuration for these three defects on a spherical surface in the next section, which corresponds to $\alpha_1 = 66°$ and $\alpha_1 = 48°$.

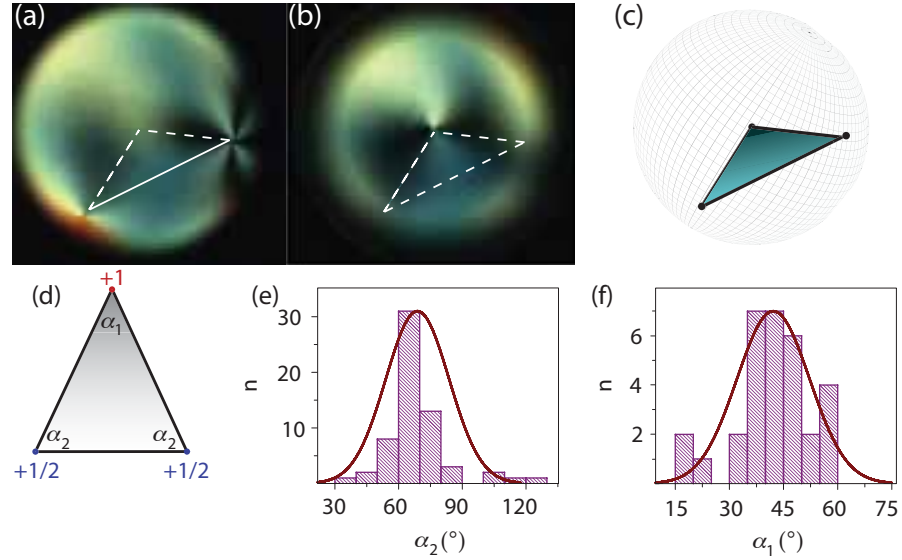Figure 16: (a), (b) Cross-polarised images of a very thin shell with three defects, two $s = 1/2$ and an $s = 1$. In (a), one of the three defects is clearly in focus, with another defect slightly below this one. In (b) the third defect is in focus. (c) Schematic diagram of the three-dimensional arrangement of the three defects. (d) Isosceles triangle formed by the three defects, with α_1 the unequal surface angle. (e),(f) Histograms of the surface angles, α_1 and α_2. Ref. [56].

2.3 TRIVALENT GROUND STATE

The free energy of a thin curved nematic film (see section 1.4) reads

$$F = \frac{1}{2} \int dA \left[k_1 \left(D_i n^i \right)^2 + k_3 \left(D_i n_j - D_j n_i \right) \left(D^i n^j - D^j n^i \right) \right],$$

(80)

where k_1 and k_3 are the two-dimensional splay and bend elastic constants and where D_i is the covariant derivative. Eq. (80) can be recast in terms of defect separation rather than the director field **n**. For a spherical nematic, the elastic energy in the one-constant approximation $k = k_1 = k_3$ reads (see eq. (78))

$$F = -\pi k \sum_{i<j}^{Z} s_i s_j \log \left(1 - \cos \theta_{ij} \right) + \sum_i^{Z} E_i \left(R \right),$$

(81)

where s_i is the topological charge of defect i, θ_{ij} is the angular distance between defects i and j, and Z is the number of defects or valence number. The self-energy $E_i(R)$ is given by

$$E_i(R) = \pi K s_i^2 \log\left(\frac{R}{a}\right) + E_c, \tag{82}$$

where R is the radius of the sphere and a is a small scale cut-off preventing a divergence of the energy. E_c represents a core energy, which depends on the details of the microscopic interactions. The self-energy is responsible for the splitting of $+1$ defect in an ideal two-dimensional nematic, because of its proportionality with s_i^2. The other term in eq. (81) describes the repulsion between like-charged defects. We wish to find the optimal location for the defects in a thin homogeneous shell given that $s_1 = 1$, $s_2 = \frac{1}{2}$ and $s_3 = \frac{1}{2}$. This requires minimising the interaction term of the free energy. We minimise the interaction energy with respect to three independent variables, namely θ_{12}, θ_{13} and the angle, C, subtended by the two curved triangular sides (circular arcs) meeting at the charge-one defect. If we apply the law of cosines on the sphere:

$$\cos\theta_{23} = \cos\theta_{12}\cos\theta_{13} + \sin\theta_{12}\sin\theta_{13}\cos C, \tag{83}$$

we can eliminate θ_{23} in favour of C in the free energy, and demand $\frac{\partial F}{\partial \theta_{12}} = \frac{\partial F}{\partial \theta_{13}} = \frac{\partial F}{\partial C} = 0$. From the latter equation, $\frac{\partial F}{\partial C} = 0$, we obtain $C = \pi$, implying that the defects lie on a great circle (see Figs. 17 and 18). There is always a circle that can be drawn through three points on a sphere; the maximal radius of this circle reflects the repulsive nature of the defects. With some straightforward algebra the other two equations, $\frac{\partial F}{\partial \theta_{12}}$ and $\frac{\partial F}{\partial \theta_{13}} = 0$, then lead to

$$\theta_{12} = \theta_{13} = \pi - \arccos\frac{2}{3} \approx 0.73\pi \approx 131.8°, \tag{84}$$

$$\theta_{23} = 2\arccos\frac{2}{3} \approx 0.54\pi \approx 96.4°. \tag{85}$$

We thus find that the defects are located at the vertices of an isosceles triangle rather than equilateral triangle, shown in Figs. 17 and 18. This less symmetric configuration arises because of the asymmetry in the magnitude of the charges of the defect: the two $+1/2$ defects repel each other less strongly than a charge one and charge one-half such that θ_{12} and θ_{13} are larger than θ_{23}. This is in marked contrast with the regular tetrahedral configuration in

Figure 17: Four views on the bend texture of the director field on the sphere containing a $+1$ defect and two $+1/2$ defects arranged in an isosceles triangle with $\theta_{12} = \theta_{13} \approx 132°$, $\theta_{23} \approx 96.4°$, $\alpha_1 \approx 48°$ and $\alpha_2 = \alpha_3 \approx 66°$.

which all the defects are equidistant, because all four charges are indistinguishable. The fact that s_2 and s_3 are of equal magnitude is still reflected in the equal length of two of the sides ($\theta_{12} = \theta_{23}$) of triangle. Perhaps surprisingly, the distance between two charge one-half defects is smaller in the trivalent state than in the more 'crowded' tetravalent state. The surface angles of the flat triangle can be found be simple trigonometry: by realising that the triangle formed by two defects and the centre of the sphere is also an
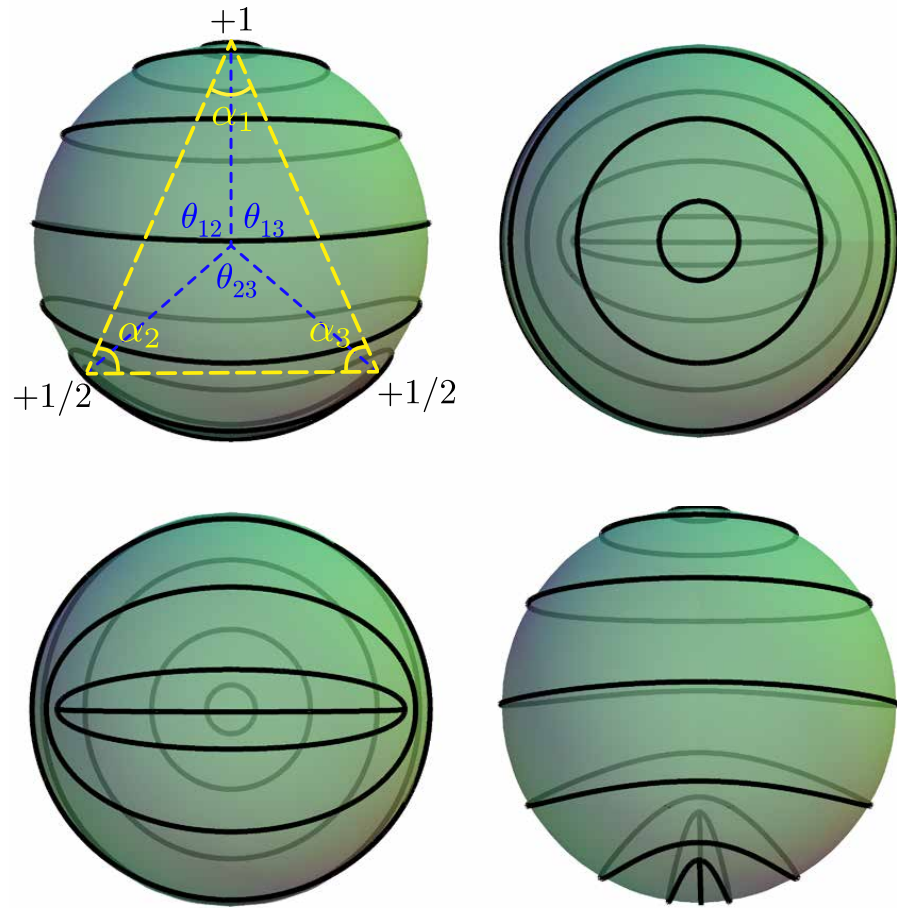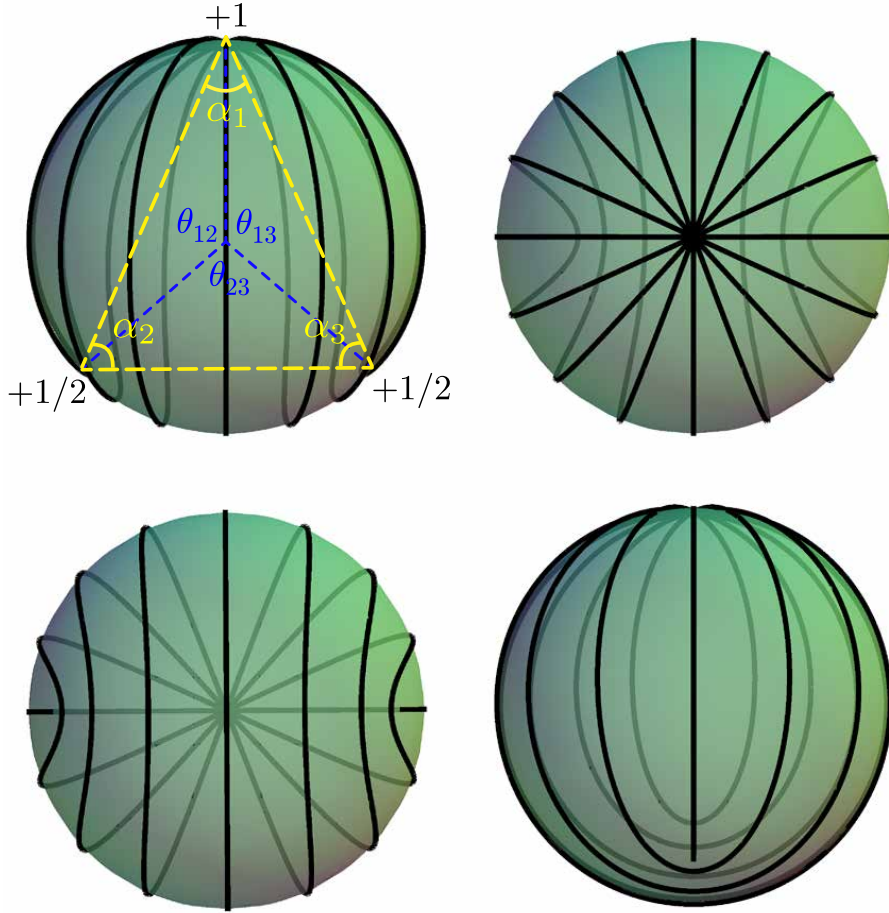
Figure 18: Four views on the splay texture of the director field on the sphere containing a $+1$ defect and two $+1/2$ defects arranged in an isosceles triangle with $\theta_{12} = \theta_{13} \approx 132°$, $\theta_{23} \approx 96.4°$, $\alpha_1 \approx 48°$ and $\alpha_2 = \alpha_3 \approx 66°$.

isosceles triangle (of which two sides have a length equal to the radius) we obtain

$$\alpha_1 = \pi - \theta_{12} = \arccos \frac{2}{3} \approx 48.2° \tag{86}$$

$$\alpha_2 = \alpha_3 = \frac{\theta_{12}}{2} = \frac{\pi}{2} - \frac{\arccos \frac{2}{3}}{2} \approx 65.9° \tag{87}$$

This is in close agreement with the experimental values reported in the previous section, which are are $\alpha_1 \approx 68°$ and $\alpha_2 \approx 46°$. Given the defect locations the energy-minimising director field can be found by means of a stereographic projection of the planar solution [57]. The bend texture is displayed in Fig. 18. Rotating this director field over an angle α yields the same free energy in the one-constant approximation. The splay texture (Fig. 17) corresponds

to $\alpha = \pi/2$. We note that the escape in the third dimension, in which singular region is distributed over a larger distance of the order of the thickness, occurs in shells of finite thickness and is somewhat different than the problem of three point defects in a two-dimensional nematic solved above. However, we expect that the defect separations will be marginally affected as long as the thickness is small compared to the radius.

2.4 VALENCE TRANSITIONS

We will now proceed with an estimate of the energy of the trivalent shell when this escape is taken into account. In doing so, we follow the arguments in ref. [105]. We first consider the energy when three singular lines are spanning the shell at angular distances reported above. We estimate this energy as the product of the two-dimensional result and the thickness, h, thus effectively taking $k = Kh$:

$$E'_{Z=3} = \pi K h \left[\left(1 + 2 \times \frac{1}{4} \right) \log \left(\frac{R}{a} \right) - 0.54 + \frac{3E_c}{\pi K h} \right]. \quad (88)$$

A heuristic yet adequate method to include the escape is to replacing the microscopic cut-off by the thickness of the shell, since the singular core is spread out over spatial dimensions of the order of h. To account for the pair of boojums an energy $4.2K\pi h$ is added [11, 105, 41]. We then obtain

$$E_{Z=3} = \pi K h \left[\log \left(\frac{R}{h} \right) + \frac{1}{2} \log \left(\frac{R}{a} \right) + 3.65 + \frac{2E_c}{\pi K h} \right]. \quad (89)$$

By comparing this to the energy of a shell with four disclination lines

$$E_{Z=4} = \pi K h \left[\log \left(\frac{R}{a} \right) - 0.43 + \frac{4E_c}{\pi K h} \right], \quad (90)$$

we can find the critical value for h above which the trivalent defect configuration is energetically preferable over the tetravalent one:

$$h^*_{34}/R = e^{4.08 - 2E_c/\pi K h} \sqrt{\frac{a}{R}} \quad (91)$$

Similarly, one can find the critical value for h below which the trivalent defect configuration is energetically preferable over the divalent one by setting $E_{Z=3}$ equal to the approximation of the

energy of a shell with two diametrically opposite pairs of surface defects, $E_{Z=2}$. Again, we will first find the energy of a shell with two singular lines

$$E'_{Z=2} = \pi K h \left[2 \log \left(\frac{R}{a} \right) - 0.69 + \frac{2E_c}{\pi K h} \right], \qquad (92)$$

after which we apply the same trick as we used to find $E_{Z=3}$ to obtain

$$E_{Z=2} = \pi K h \left[2 \log \left(\frac{R}{h} \right) + 7.69 \right]. \qquad (93)$$

We find a very similar value

$$h^*_{23}/R = e^{4.04 - 2E_c/\pi K h} \sqrt{\frac{a}{R}}. \qquad (94)$$

The energy as a function of thickness is plotted in Fig. 19 for all three different valencies. Since $h^*_{23} < h^*_{34}$ there is no h for

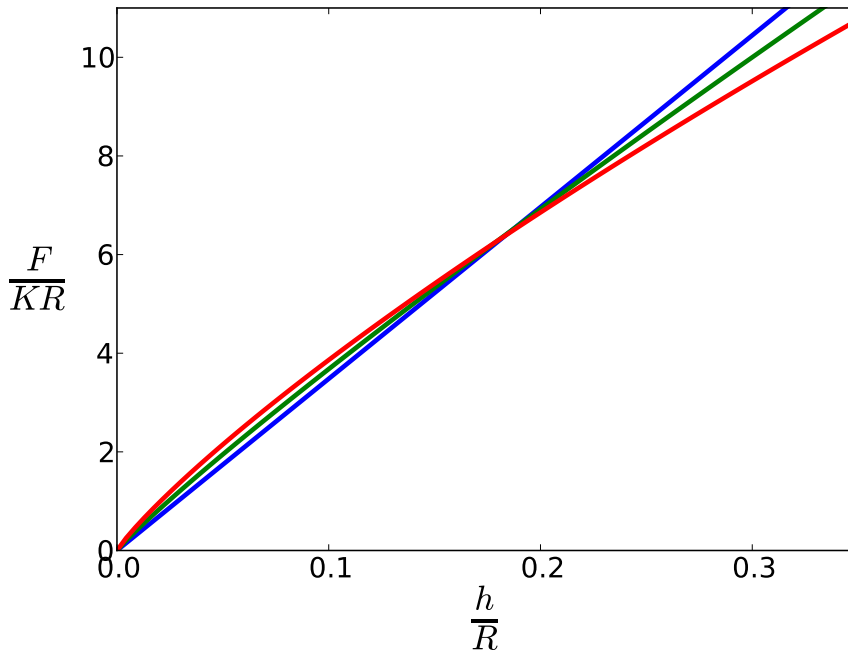Figure 19: Elastic energy as a function of shell thickness for divalent (red), trivalent (green) and tetravalent (blue) defect configuration for $R/a = 10^5$ and $E_c = 0$. Either the divalent or tetravalent configuration, but not the trivalent configuration, is lowest in energy.

which the trivalent shell has lower energy than both the divalent and tetravalent shell. The energy barriers between them however

are very large. The energy barrier for going from the trivalent to tetravalent shell lies in undoing the escape and is thus the difference between $E'_{Z=3}$ and $E_{Z=3}$:

$$\Delta E_{3\to4} = \pi K h \left(\log\left(\frac{h}{a}\right) - 4.19 + \frac{E_c}{\pi K h} \right). \tag{95}$$

The energy barrier for going from the trivalent to tetravalent shell lies in overcoming the repulsion between the two $+1/2$ defects and can thus be estimated by the difference between $E'_{Z=2}$ and $E'_{Z=3}$:

$$\Delta E_{3\to2} = \pi K h \left(\frac{1}{2}\log\left(\frac{R}{a}\right) - 0.15 - \frac{E_c}{\pi K h} \right). \tag{96}$$

Since $K \approx 10^{-11} N$, for a thin shell with $h = 1 \ \mu m$, these barriers are four orders of magnitude larger than the thermal energy scale (at room temperature), $k_B T$, where T denotes temperature and k_B is Boltzmann's constant, thus providing stability of the trivalent state. Valence transitions are unlikely to occur.

2.5   BOND FIDELITY

In this section, we will consider the fidelity of the three bonds by considering its robustness against thermal fluctuations. We will expand the energy around the equilibrium values for the zenith and azimuthal angles, $\{\theta_i^0, \phi_i^0\}$. We parametrise the departures from the equilibrium angles with a $2Z$-component vector $\mathbf{q}$, whose first three components are the deviations along the lines of longitude of the sphere and whose final three components are the deviations along the lines of latitude of the sphere. We thus have

$$q_i = \delta\theta_i, \tag{97}$$
$$q_{3+i} = \delta\phi_i \sin\theta_i. \tag{98}$$

Again we employ the law of cosine on the sphere:

$$\begin{aligned}
\cos\theta_{ij} = {} & \cos\left(\theta_i^0 + q_i\right)\cos\left(\theta_j^0 + q_j\right) \\
& + \sin\left(\theta_i^0 + q_i\right)\sin\left(\theta_j^0 + q_j\right) \\
& \times \cos\left(\phi_i^0 - \phi_j^0 + \frac{q_{3+i}}{\sin\theta_i^0} - \frac{q_{3+j}}{\sin\theta_j^0}\right),
\end{aligned} \tag{99}$$

to rewrite F in eq. (81) as an expansion to quadratic order in q:

$$F = F\left(\theta_i^0, \phi_i^0\right) + \frac{1}{2}\sum_{ij} M_{ij}q_iq_j + \mathcal{O}\left(q^4\right). \qquad (100)$$

The 6×6 matrix M can thus be found by

$$M_{ij} = \left(\frac{\partial^2 F}{\partial q_i \partial q_j}\right)_{q_i=q_j=0}. \qquad (101)$$

This calculation is performed without loss of generality upon choosing the ground state defect locations to be on the equator, *i.e.* $\theta_i^0 = \pi/2$. We diagonalise this matrix:

$$M = UDU^T. \qquad (102)$$

The matrix D has the following eigenvalues on the diagonal:

$$\{\lambda_i\} = \frac{\pi k}{20}\{0, 0, 0, 15, 17, 18\}. \qquad (103)$$

The columns of the matrix U are the corresponding orthonormal eigenvectors, $\{\mathbf{u}_i\}$, and U^T is the transpose of U. The eigenvectors belonging to the three zero eigenvalues represent rigid body rotations. The other eigenvectors are

$$\mathbf{u}_4 = \begin{pmatrix} 0 \\ 0 \\ 0 \\ 0 \\ -\frac{1}{\sqrt{2}} \\ \frac{1}{\sqrt{2}} \end{pmatrix}, \ \mathbf{u}_5 = \begin{pmatrix} \frac{4}{\sqrt{34}} \\ \frac{3}{\sqrt{34}} \\ \frac{3}{\sqrt{34}} \\ 0 \\ 0 \\ 0 \end{pmatrix}, \ \mathbf{u}_6 = \begin{pmatrix} 0 \\ 0 \\ 0 \\ \sqrt{\frac{2}{3}} \\ \frac{1}{\sqrt{6}} \\ \frac{1}{\sqrt{6}} \end{pmatrix}. \qquad (104)$$

The fourth and sixth eigenvalues also correspond to deformations that keep the defects located at a great circle. The fourth one corresponds to a displacement of the charge one-half defects such that their distance to the charge one defect grows or shrinks in equal manner and hence preserves the isosceles shape of the triangle (Fig. 20a). The sixth eigenvalue corresponds to a mode of deformation that does not posses this property, thus breaking the symmetry of reflection across the bisector of the distinct angle (Fig. 20c). The mode of deformation corresponding to the fifth eigenvalue, however, retains the isosceles shape of the triangle, but shrinks the
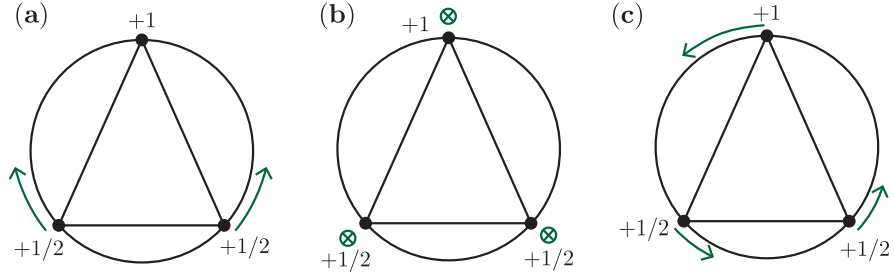
Figure 20: Schematics of the three non-trivial eigenmodes correspond-
ing to (a) $\mathbf{u}_4$, (b) $\mathbf{u}_5$ and (c) $\mathbf{u}_6$. The defects (represented by
dots) continue to lie on a great circle in (a) and (c), but not
in (b). The defects continue to form an isosceles triangle in
(a) and (b), but not in (c).

size of the triangle as the defects do not lie on a great circle any-
more (Fig. 20b). We change the basis from q_i to w_i, which is the
departure from the trivalent ground state in the i-th eigendirection:

$$q_i = U_{ij} w_j. \tag{105}$$

This basis transformation yields to quadratic order in w_i:

$$F = F\left(\theta_i^0, \phi_i^0\right) + \frac{1}{2}\lambda_4 w_4^2 + \lambda_5 w_5^2 + \lambda_6 w_6^2. \tag{106}$$

By equipartition, each term contributes $\frac{1}{2}k_B T$. The eigenvalues
corresponding to the trivalent modes of deformation are equal or
larger than the the tetravalent ones (which are $\frac{3}{8}\pi k$ and $\frac{3}{4}\pi k$ [70,
105]): the trivalent ground state is thus somewhat better protected
against thermal fluctuations.

2.6 CONCLUSION

In a spherical nematic shell of finite thickness a stable defect struc-
ture with two $s = 1/2$ lines and one pair of boojums is observed
experimentally, besides the bipolar and regular tetrahedral con-
figuration. If the shell is thin and homogeneous in thickness, the
repulsive interdefect interaction pushes the defects to lie on a great
circle. The strength of the interaction depends on the charges of
the defects. Consequently, the defects are located at the vertices of
an isosceles triangle rather than an equilateral triangle, in contrast

to the tetravalent ground state in which the defects are equidistant. In the energetically most favourable trivalent configuration, we obtain for the central angles $\theta_{12} = \theta_{13} = 0.73\pi$, $\theta_{23} = 0.54\pi$ and for the angles in the (flat) isosceles triangle $\alpha_1 = 48°$ and $\alpha_2 = \alpha_3 = 66°$. These values are in good agreement with experimental values. Estimations of the elastic energy show that there is no shell thickness for which the trivalent ground state is lower than both the tetravalent and divalent ground state. However, there are large energy barriers to provide stability for the trivalent state once it is created.

THICK SHELLS

3.1 INTRODUCTION

Many systems in condensed matter physics and elasticity can be treated as two-dimensional, though only very few, like graphene [74] and colloidal crystals at liquid-liquid interfaces [21, 4, 34], are truly *mono*layers. The theory of plates and membranes [44], superfluid [102] and liquid crystal films [6] can all be neatly described by a reduction of the number of spatial dimensions from three to two by assuming that the thickness is small compared to the other two dimensions and approximately constant. This reduction of dimensions usually simplifies the analysis significantly, because the number of variables to solve for is reduced and in addition one can employ well developed mathematical machinery such as complex analysis that is well suited to tackle two-dimensional problems. For instance, the use of conformal mappings has been applied successfully in superfluid films [102]. Another example of the use of a conformal mapping was in the study of the tetravalent defect configuration in a two-dimensional nematic on a spherical surface [57]. From the previous chapter (chapter 2) we learned that a finite shell thickness allows for shells with different valency. Experiments on nematic double emulsion droplets also show that the thickness inhomogeneity of the shell plays a crucial role [56]. Since the density difference between the inner drop and the liquid crystal, buoyancy displaces the inner drop out of the centre of the larger drop along the gravitational direction, as shown schematically in Fig. 10. This leads to a rich variety of defect structures, as shown in Fig. 21. One of the striking manifestations of the inhomogeneity are very abrupt confinement and deconfinement transitions in shells with two pairs of surface defects, called boojums[1]. When the shell is rather thick and homogeneous, the two pairs

---

1 At this point it is interesting to note that in the solid analogue of the liquid crystal shell, thickness inhomogeneity is also important. It affects the buckling and folding of these solid capsules [16].
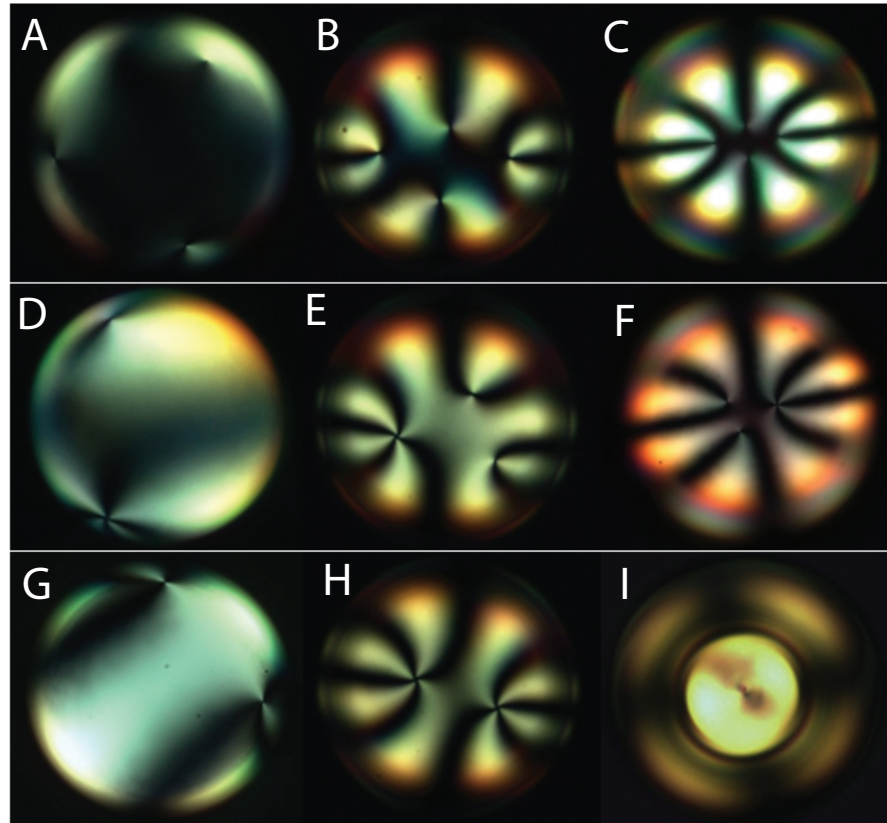
Figure 21: Defect evolution with thickness inhomogeneity. Cross-polarised images illustrating the various angular configurations of the defects in shells with four defects (A-C), shells with three defects (D-F) and shells with two defects (G-I) for different values of the shell thickness. Thickness and thickness inhomogeneity increase from left to right. Ref. [56].

are aligned diametrically (Figs. 11a and 21I). However, upon increasing the thickness inhomogeneity beyond a critical value, one pair migrates rapidly toward the other pair such that eventually all defects are confined to the thinnest section of the shell (Figs. 11b, 11c and 21G-H). This migration is in this chapter called the confinement transition and the reverse process, in which the boojum pairs maximise their angular separation, is referred to as the deconfinement transition. The investigation of these phenomena, and more generally the theoretical study of the director fields and energetics of inhomogeneous divalent nematic shells, is the main concern of this chapter. Although the thickness truly makes this a three-dimensional problem, we are able to use two-dimensional techniques such as conformal mappings to find an *Ansatz* for the

director field in spherical shells. This method is presented in detail in section 3.2. In section 3.3, we study the homogeneous shells as a function of thickness, taking into account the elastic anisotropies. In section 3.4, we construct a phase diagram for inhomogeneous shells that maps out the stability and coexistence of the confined and deconfined configurations as a function of shell thickness and thickness inhomogeneity. Our findings are shown to be in qualitative agreement with recent experimental studies. Finally, the effect of elastic anisotropy on the deconfinement transition is briefly discussed in the concluding section 3.5.

3.2 DIRECTOR FIELDS IN DIVALENT NEMATIC SHELLS

The experimental system under consideration is a nematic double emulsion droplet: a nematic liquid crystal droplet of radius R that encapsulates a smaller water droplet of radius a, as depicted in Fig. 10 and discussed in section . We defined a thickness $h \equiv R - a$ of the shell. Since in general the displacement of the inner water droplet out of the centre of the nematic droplet, Δ, is nonzero, h should be thought of as an average quantity. A surfactant or polymer is added to the inner and outer water phases for two reasons. First of all, it stabilises the double emulsion droplet, because it prevents the inner water droplet to coalesce with the continuous water phase. Secondly, it anchors the nematic molecules parallel to the interfaces. In modelling this experimental system we will employ elasticity theory for nematic liquid crystals, in which one constructs a Frank free energy functional as an expansion in spatial distortions of the local average orientation of the molecules, *i.e.* the unit director field, $\mathbf{n}\left(\mathbf{x}\right)$, that respect the symmetries of the nematic liquid crystal [18, 40]:

$$
\begin{aligned}
F[\mathbf{n}\left(\mathbf{x}\right)] = \frac{1}{2} \int dV \left(K_1 \left(\nabla \cdot \mathbf{n}\right)^2 + K_2 \left(\mathbf{n} \cdot \nabla \times \mathbf{n}\right)^2 \right. \\
\left. + K_3 \left(\mathbf{n} \times \nabla \times \mathbf{n}\right)^2 \right) - K_{24} \int \mathbf{dS} \cdot \left(\mathbf{n}\nabla \cdot \mathbf{n} + \mathbf{n} \times \nabla \times \mathbf{n}\right),
\end{aligned}
\tag{107}
$$

provided that we assume that these deformations are small on the molecular length scale. Here, K_1, K_2, K_3 and K_{24} are elastic constants measuring the amount of splay, twist, bend and saddle-splay deformations respectively. In most of the work presented, we will work in the one-constant approximation, in which the splay,

twist and bend elastic constants are taken to be equal: $K = K_1 = K_2 = K_3$. Then, eq. (141) reduces to

$$F[\mathbf{n}\,(\mathbf{x})] = \frac{1}{2}K \int dV\,(\partial_i n_j)^2$$
$$- \left(K_{24} - \frac{1}{2}K\right) \int d\mathbf{S} \cdot (\mathbf{n}\nabla \cdot \mathbf{n} + \mathbf{n} \times \nabla \times \mathbf{n})\,. \tag{108}$$

Furthermore, we discard the surface term in eq. (108), effectively taking $2K_{24} = K$. For a typical droplet size of $50\,\mu m$ the anchoring energy is much larger than the total elastic energy. Therefore, we can take the preferred tangential alignment of the nematic molecules at the interface as a constraint, thus establishing a boundary condition complementing the free energy. Our approach to minimising the free energy with respect to the director field, will be to find a realistic *Ansatz* given certain locations of the defects. By varying these locations for different shell geometries we obtain the energy landscape as a function of defect positions, thickness and thickness inhomogeneity. The technique we employ to obtain the *Ansatz* is the method of conformal mappings. With the inverse stereographic projection we can find an *Ansatz* for a director field in a homogeneous shell (section 3.2.1). Then, by using an electrostatic analogy we can expand the *Ansatz* to the inhomogeneous case (section 3.2.2). An additional numerical minimisation takes care of the escape of the disclination lines in the third dimension.

3.2.1   *The inverse stereographic projection and the Ansatz for the homogeneous shell*

The *Ansatz* for the director $\mathbf{n}$ of the homogeneous bipolar shell, with two straight disclination lines along the z-axis, simply reads

$$\mathbf{n}\,(\mathbf{x}) = \cos\alpha\,\hat{\theta} + \sin\alpha\,\hat{\phi}, \tag{109}$$

where $\hat{\theta}$ and $\hat{\phi}$ are the unit vectors corresponding to the zenith, θ, and azimuthal, ϕ, angles respectively. Note that α is the angle over which $\mathbf{n} = \hat{\theta}$ is rotated at each point on the sphere with respect to an orthonormal reference frame. Thus, the director fieldlines for $\alpha = 0$ and $\alpha = \pi/2$ correspond to the meridians and circles of latitude. To find the *Ansatz* for any other locations of the disclination lines, however, we perform an inverse stereographic projection (Fig. 22). A director field in the flat uv-plane (Fig. 23), minimising
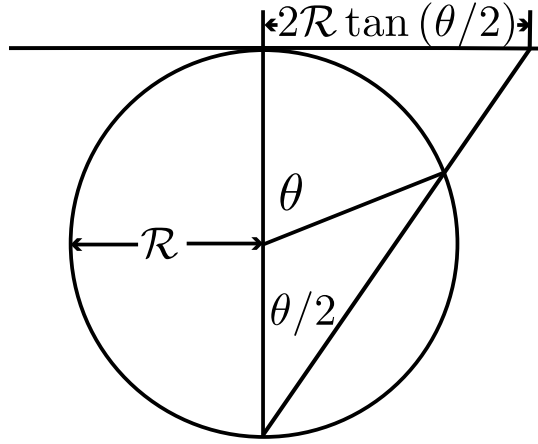
Figure 22: The inverse stereographic mapping given by eq. (248) of the the uv-plane onto the sphere with radius $\mathcal{R}$.

the free energy (see appendix A), is projected onto the concentric surfaces of spheres with radii, $\mathcal{R}$, varying between a and R, *i.e.* $a \leq \mathcal{R} \leq R$, that fill up the shell. Hereby, angles are preserved, *i.e.* this mapping is conformal. This director field contains two charge-one point defects, as we eventually wish to construct an *Ansatz* with two charge-one line defects spanning the shell. We find (see

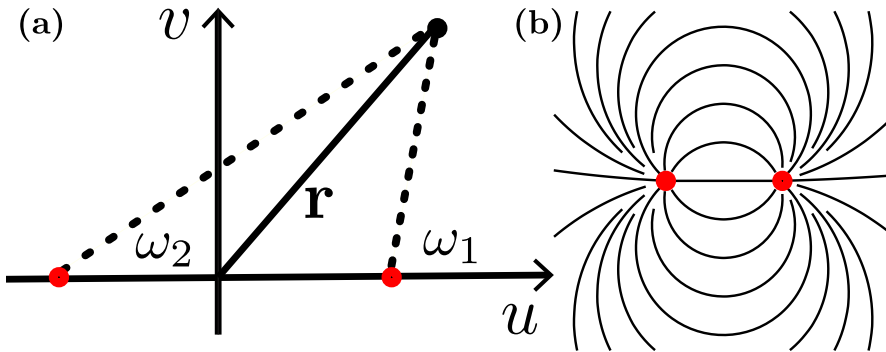Figure 23: (a) Point defects (red dots) in the uv-plane located at $(u_i, 0)$. The angular director field, $\boldsymbol{\Phi}(\mathbf{r})$ is the sum of the single defect solutions $\boldsymbol{\Phi}_i = \omega_i$. (b) Schematic of the resulting fieldlines.

appendix A)

$$\mathbf{n} = \cos\left(\Phi - \phi\right)\hat{\boldsymbol{\theta}} + \sin\left(\Phi - \phi\right)\hat{\boldsymbol{\phi}}. \tag{110}$$

with Φ given by

$$\Phi = \alpha + \sum_{i=1,2} \arctan\left(\mathcal{Y}_i, \mathcal{X}_i\right), \tag{111}$$

$$\mathcal{X}_i = \tan\left(\frac{\theta}{2}\right)\cos\phi - \mathrm{sgn}\left(u_i\right)\tan\left(\frac{\theta_i}{2}\right), \tag{112}$$

$$\mathcal{Y}_i = \tan\left(\frac{\theta}{2}\right)\sin\phi, \tag{113}$$

as the director field on the sphere, depicted in Fig. 24. In ref. [57] it was shown that this field on the sphere minimises the free energy in the one-constant approximation, provided that it possesses two charge-one defects. They are located at zenith angles

$$\theta_i = 2\arctan\left(\frac{|u_i|}{2\mathcal{R}}\right). \tag{114}$$

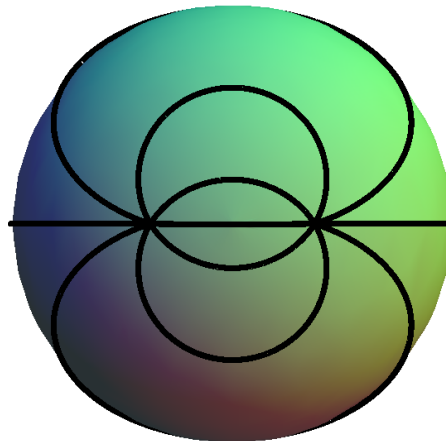At the same time this expression is an *Ansatz* for a homoge-

Figure 24: Top view of the director field on the sphere, given by eq. (110).

neous shell with two straight disclination lines spanning the shell, provided we build it out of concentric spheres of radius $\mathcal{R}$. The director lies along the spheres, including the special case that these spheres are the surfaces of the inner or outer droplets. Therefore, the tangential boundary conditions are satisfied.

3.2.2 *An electrostatic analogy and the Ansatz for the inhomogeneous shell*

The concentric spheres that fill up the homogeneous shell are displaced if the shell is inhomogeneous. Moreover, the disclination

lines are no longer straight. To construct an *Ansatz* for the director in inhomogeneous shells we need to find equations for the displaced spheres and the defect lines. For this, we exploit an electrostatic analogy, namely, calculating the equipotential (solid in Fig. 25) and electric (dashed green) field lines of an infinitely long charged line running parallel to a conducting plane (blue) at a distance d. By the method of images, solving this electrostatic
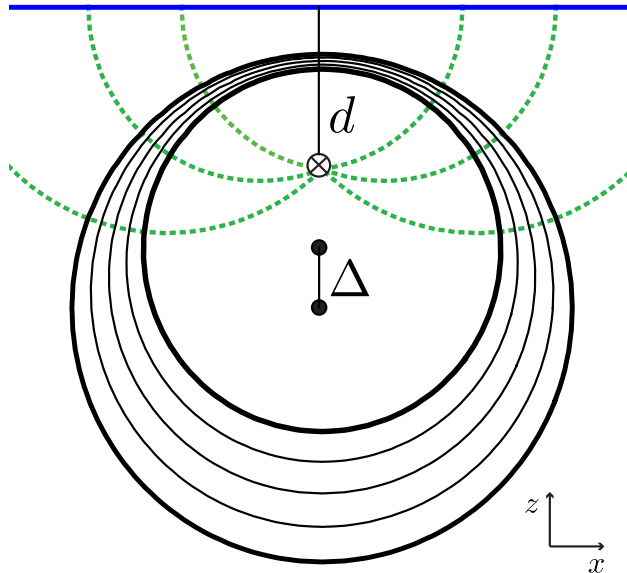

Figure 25: Equipotential (solid) and field (dashed green) lines of an infinitely long charged line, indicated with a cross, running along the y-direction, parallel to a conducting plane (blue) at a distance d. The two equipotential circles, drawn in bold, correspond to two non-concentric droplets whose centres, indicated by dots, are displaced by Δ.

problem is equivalent to solving for the equipotential and electric field lines of two oppositely charged parallel running cylinders, or, equivalently, a 2D point charge and its mirror charge. These can be extracted from the complex potential [91, 30]

$$\psi\left(w\right) = \log\left(\frac{w+id}{w-id}\right). \tag{115}$$

where $w = x + iz$ is a complex number. Note that ψ is a conformal transformation, just like the inverse stereographic projection is, mapping a region bounded by two non-concentric circles into a vertical strip (see appendix B). Thus, the level curves of the real and imaginary parts of $\psi\left(w\right)$ are the equipotential and electric field lines, respectively. These two families of orthogonal lines,

together forming what is known as an isothermic net, read mathematically

$$\Re[\psi(w)] = \log\left|\frac{w+id}{w-id}\right| = \text{constant}, \tag{116}$$

$$\Im[\psi(w)] = \arg\left(\frac{w+id}{w-id}\right) = \text{constant}. \tag{117}$$

We see that eq. (116) describes circles of Apollonius (see appendix B) with inverse points $\pm id$. We can rewrite it as

$$x^2 + (z-\eta)^2 = \mathcal{R}^2, \tag{118}$$

with radius, $\mathcal{R}$, and displacement with respect to the origin, η, which are related by

$$\mathcal{R}^2 = \eta^2 - d^2. \tag{119}$$

Rotating the circular equipotential lines around the z-axis creates the non-intersecting spheres. By choosing two of these spheres (drawn in bold in Fig. 25) as the surfaces of our inner and outer droplets in addition to a choice of d, we can fix the geometry. The relative displacement of the inner droplet with respect to its concentric position, Δ, is given by

$$\Delta = \eta_a - \eta_R, \tag{120}$$

where η_a and η_R are the vertical displacements from the origin of the inner and outer spheres, respectively. We take $\eta < 0$, such that $\Delta > 0$. This implies that the thinnest part of the shell is at the top, like in Figs. 25 and 10. The other spheres fill up the shell. Since the spheres are the surfaces of revolution of the circles around the z-axis, we obtain the equation for the spheres simply by addition of y^2 to the left hand side of eq. (118):

$$x^2 + y^2 + (z-\eta)^2 = \mathcal{R}^2. \tag{121}$$

Two independently chosen electric field lines will serve as disclination lines. These lines run perpendicular to the equipotential lines, and thus perpendicular to the surface of the inner and outer droplet, as is demanded by the tangential boundary conditions. Similar to the calculation of the equipotential lines, one can obtain the equations for the electric field lines from eq. (117) (appendix B). We find that the electric field lines are also circles:

$$(x - \epsilon)^2 + z^2 = S^2, \tag{122}$$

with radii, S, and displacements, ϵ, now in the x-direction, which are related as follows:

$$S^2 = \epsilon^2 + d^2. \tag{123}$$

Since only the circular arc that is inside the shell matters, we care about the points of intersection of the two defect lines with the spheres that fill up the shell. We would like to find the zenith angle on each sphere, β_i , that these points of intersection make. We assign a different character than θ_i, because β_i does not have a constant value as it depends on the displacement (or radius) of the sphere. Let us therefore refine our definition of θ_i as the zenith angle of the defect on the outer-most sphere. Now, the following geometrical relations hold:

$$x = \pm \mathcal{R} \sin \beta_i, \tag{124}$$

$$z = \eta + \mathcal{R} \cos \beta_i. \tag{125}$$

Then, by substituting x and z in eq. (122) and eliminating d in favour of $\mathcal{R}$ by applying eq. (119) we find an expression for ϵ_i as a function of β_i, η and $\mathcal{R}$ (assuming $\sin \beta_i \neq 0$):

$$\epsilon_i = \pm \frac{\mathcal{R} + \eta \cos \beta_i}{\sin \beta_i} = \pm \frac{\mathcal{R} + \eta_{\mathcal{R}} \cos \theta_i}{\sin \theta_i} \tag{126}$$

where the last equality follows from the constantness of ϵ_i, as we are moving along the same circle. We find the solution for β_i

$$\beta_i = 2 \arctan \left(\frac{\epsilon_i + \sqrt{\epsilon_i^2 + d^2}}{\mathcal{R} - \eta} \right). \tag{127}$$

Not surprisingly, β_i is increasing as the radius of the sphere is decreasing. If $\theta_i = 0$ or $\theta_i = \pi$, the disclination lines are straight and $\beta_i = 0$ or $\beta_i = \pi$, respectively. Next, we find η as a function of the spatial coordinates x, y and z, since it is the only variable, besides the parametric dependence on d and θ_i, on which β_i is depending. Put differently, given some point in space, on which sphere is it? To answer this question we resort to eq. (121), yielding the following result:

$$\eta(\mathbf{x}) = \frac{x^2 + y^2 + z^2 + d^2}{2z}. \tag{128}$$

We have now acquired all the necessary information to construct the *Ansatz* for the director field in an inhomogeneous shell. We

take the *Ansatz* for the director field in a homogeneous shell, eq. (110), and make the following replacements

$$\theta_i \to \beta_i, \tag{129}$$

$$z \to z - \eta. \tag{130}$$

The first substitution concerns the defect lines. The second accounts for the displacement of the spheres and implies the substitution

$$\theta \to \beta = \arccos\left(\frac{(z - \eta)}{x^2 + y^2 + (z - \eta)^2}\right), \tag{131}$$

with β being the zenith angle on the displaced sphere. Finally, together with eqs. (126)-(131) we obtain the *Ansatz* for the director in inhomogeneous shells with two charge-one disclination lines:

$$\mathbf{n} = \cos\left(\Phi - \phi\right)\hat{\boldsymbol{\beta}} + \sin\left(\Phi - \phi\right)\hat{\boldsymbol{\phi}}. \tag{132}$$

where Φ is now given by

$$\Phi = \alpha + \sum_{i=1,2} \arctan\left(\mathcal{Y}_i, \mathcal{X}_i\right), \tag{133}$$

$$\mathcal{X}_i = \tan\left(\frac{\beta}{2}\right)\cos\phi - \text{sgn}\left(u_i\right)\tan\left(\frac{\beta_i}{2}\right), \tag{134}$$

$$\mathcal{Y}_i = \tan\left(\frac{\beta}{2}\right)\sin\phi. \tag{135}$$

The disclination lines can be put anywhere except for the south pole. In the case of a bipolar defect arrangement, i.e. $\theta_i = 0$ and $\theta_i = \pi$, we draw on each sphere the director given by eq. (109), with the substitution in eq. (131) and find an *Ansatz* for the bipolar inhomogeneous shell that reads

$$\mathbf{n}\left(\mathbf{x}\right) = \hat{\boldsymbol{\beta}} = \cos\beta\cos\phi\hat{\mathbf{x}} + \cos\beta\sin\phi\hat{\mathbf{y}} - \sin\beta\hat{\mathbf{z}}. \tag{136}$$

The *Ansatz* is then subjected to a numerical minimisation, employing the finite element method [93] suitable for non-trivial geometries, to ensure the escape of the disclination lines leaving a point defect at the inner and outer surface for each line (see Figs. 26a and 26b). We refine the mesh at these defects to obtain good accuracy on the rapidly changing director (Fig. 26c).
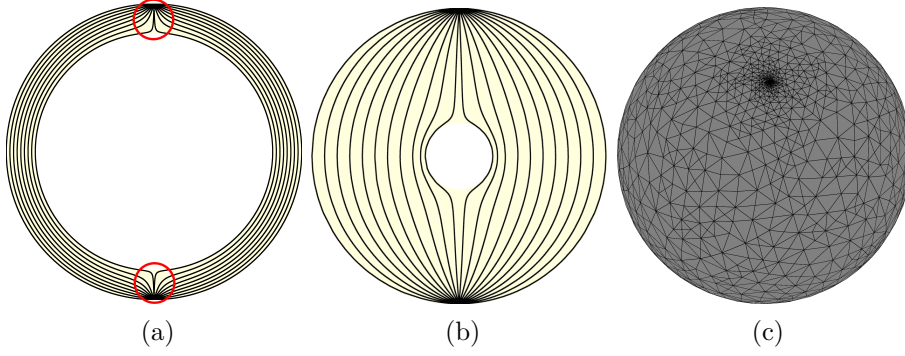
Figure 26: (a,b) Director field of the shell for (a) $\frac{h}{R} = 0.2$ and (b) $\frac{h}{R} = 0.77$. The disclination lines escape in the third dimension leaving two pairs of boojums. Each pair is encircled in red in (a). The director field in (b) resembles a slightly distorted director field of a single nematic droplet. (c) A typical mesh used in the numerical minimisation is refined around the locations of the defects.

3.3 ENERGETICS OF HOMOGENEOUS SHELLS

First, we calculate the free energy for the *Ansatz* in (109), in which the defects are located at opposite poles on the sphere, by integrating the free energy density over the spherical shell except for a cut-off region determined by $0 < \theta < \frac{b}{r}$ and $\pi - \frac{b}{r} < \theta < \pi$ with r the radial coordinate. The result reads

$$
\begin{aligned}
F =& 2\pi \left(K_1 \cos^2 \alpha + K_3 \sin^2 \alpha \right) \\
& \left(R \log \frac{2R}{b} - (R - h) \log \frac{2(R - h)}{b} - 2h \right) \\
& + 2\pi \left(K_3 - 2K_{24} \right) h \qquad\qquad (137) \\
\xrightarrow{K_i = K} & 2\pi K \left(R \log \frac{2R}{b} - (R - h) \log \frac{2(R - h)}{b} - 2h \right).
\end{aligned}
$$
$$(138)$$

Note that splay and bend deformations can be transformed into each other by tuning α, but the total energy is unchanged if $K_1 = K_3$, as is shown graphically in Fig. 27a. Furthermore, note that the saddle-splay term is proportional to the thickness, in contrast to the splay and bend energy which both contain a logarithmic divergence. We therefore expect that, as a first approach, it is not so important in determining the defect locations. Since these defects repel each other, for homogeneous shells we always find
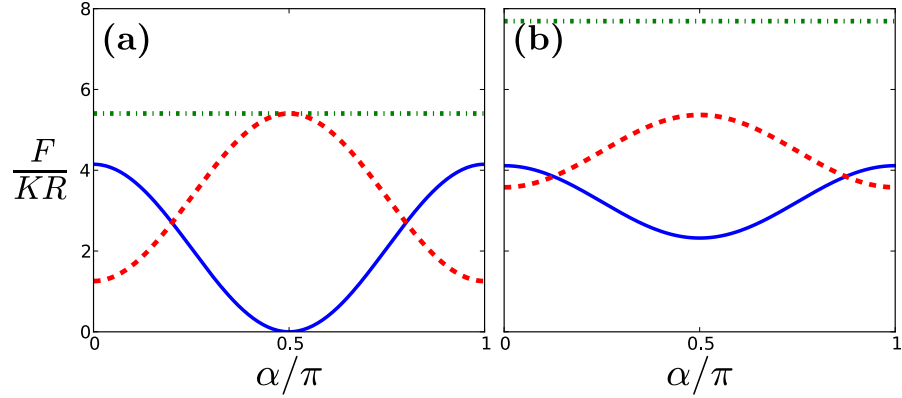
Figure 27: The splay (solid blue), bend (dashed red), and their sum (dashed-dotted green) as a function of α when (a) $\theta_{12} = \pi$ and (b) $\theta_{12} = 0.1\pi$, in both cases $\frac{b}{R} = 0.025$.

this bipolar arrangement as the free energy minimum, irrespective of thickness. Placing the defects at a different angular separation, θ_{12}, from each other, eq. (110), leads to an increase in the elastic energy, since $F \sim -\log(1 - \cos\theta_{12})$ [57, 70, 105]. Moreover, the splay and bend cannot be efficiently transferred into one another by a global rotation (changing α), e.g. splay no longer vanishes for $\alpha = \pi/2$ whereas it did for eq. (109). This is presented graphically in Fig. 27b. Note that the director field minimising the free energy for $K_1 \neq K_3$ is not equal to the *Ansatz* [3, 88, 23, 55, 49]. Besides the elastic anisotropy the escape of the defect lines in the third dimension modifies the energetics. As a result, there are two pairs of boojums residing on the interfaces. We can effectively take the escape into account in our calculations of the energy by replacing the cut-off b by the thickness h and adding $4.2\pi Kh$ for each pair of boojums[105, 11]. We obtain in the one-constant approximation

$$F = 2\pi K \left(R \log \frac{2R}{h} - (R - h) \log \frac{2(R - h)}{h} + 2.2h \right). \quad (139)$$

In Fig. 28 we compare this analytical estimate with numerical results from our procedure outlined in the previous section. We find a good agreement, in particular for small $\frac{h}{R}$, as expected. In this regime, the free energy rises as the volume of the shell increases. For large $\frac{h}{R}$, our result deviates from eq. (139). Remarkably, as the thickness is increased, the free energy decreases after some critical value, $h^*/R \approx 0.6$. The size of the inner droplet, which is $2a$, is no
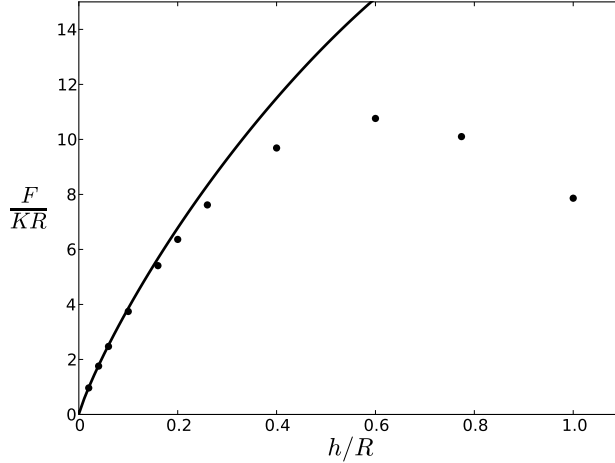
Figure 28: Free energy of the bipolar shell as a function of thickness. The line is given by the analytical estimate in eq. (139).

longer larger that the scale over which the escape happens, which is roughly h. Equating these two length scales gives a consistent back-of-the-envelope estimate $h^*/R \approx 2/3$. As a result, when h becomes comparable to R, the inner droplet no longer forms an obstruction that makes the shell locally look like a slab in which the lines can escape. Rather, the point of view that a slight director distortion is induced in a single nematic droplet (resulting in an energy cost) is more appropriate in this regime. This cross-over is illustrated in Figs. 26a and 26b.

3.4 ENERGETICS OF INHOMOGENEOUS SHELLS

3.4.1 *Buoyancy versus elastic forces*

Before we study the effect of the thickness inhomogeneity on the mechanics of the nematic liquid crystal, we first investigate its origin. In our experiments we observe that the inner water droplet is displaced along the vertical direction. This implies that gravity plays its part, but it does not necessarily mean that it is the density mismatch between the nematic and water that drives the motion of the inner droplet. Another possibility would be that the elastic forces push the droplet out of the centre, while gravity only breaks the symmetry. To identify the origin of the thickness inhomogeneity, we will compare the magnitude of the elastic forces

with Archimedes force. Therefore we map out the elastic energy as a function of the displacement $\frac{\Delta}{h}$ for several values of $\frac{h}{R}$, as shown in Fig. 29. Our first observation is that the stability of this pertur-
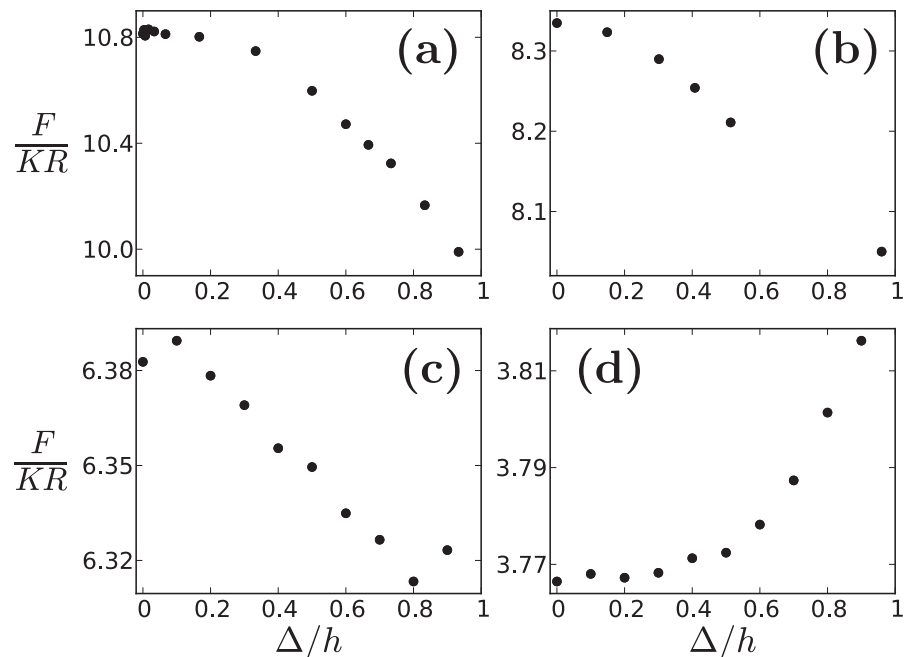

Figure 29: The elastic free energy of the liquid crystal as a function of the relative displacement of the inner droplet. In (a), (b) and (c), $\frac{h}{R} = 0.6, 0.3, 0.2$, respectively, the energy is minimised when the droplet is on the periphery of the larger droplet, resulting in an elastic force of the order of K pushing the inner droplet outwards. (d) For a thinner shell with $\frac{h}{R} = 0.1$, there is a restoring force on the inner droplet, driving it back to the centre of the outer one.

bation is a nontrivial function of the thickness. For $\frac{h}{R} = 0.2, 0.3, 0.6$ we observe that the energy decreases as a function of Δ. This is in agreement with a calculation done for $\frac{h}{R} = 0.77$ in ref. [24]. However, for a relative thin shell of $\frac{h}{R} = 0.1$ there is an elastic minimum for $\Delta = 0$. Second, the magnitude of the elastic force is less than or of the order of $f_e \sim K \approx 10^{-11} N$. This is much smaller than the net force from buoyancy and the weight of the droplet $f_b = (\rho_{nem} - \rho_w) gV$ with the volume of the water droplet $V = \frac{4}{3}\pi a^3$. For $a \approx 50 \, \mu m$ and a difference in density between 5CB and water of roughly $3 \times 10 \, kg \, m^{-3}$ at room temperature[19], we find $f_b \approx 2 \times 10^{-10} N$. Therefore, we conclude that buoyancy is

indeed responsible for displacing the inner water droplet from the centre in our experiments. If one would try to match the density of the nematic to the water density, as was done in some of the experiments in ref. [24], where the density difference was brought down to 2 $kg\ m^{-3}$, f_b and f_e will be of the same order, but only when the inner droplet is at the periphery. Also in the regime of small a these forces will become comparable.

3.4.2 *Confined and deconfined defect configurations*

In the remainder of this chapter we will compare two distinct defect configurations. In one configuration the defects are at maximum angular separation from each other at opposite sites on the sphere. We will refer to this as the deconfined state. In the other case the defects are trapped or confined to the thinnest top part of the shell. The defects are located symmetrically at an angle θ_i from the vertical axis so that their angular separation is simply $\theta_{12} = 2\theta_i$ (provided that $2\theta_i \leq \pi$). The energy can be estimated to grow with the thickness of the shell where the defects are located. This is roughly the minimal thickness at the top of the shell, for which there is a simple geometrical relation $h_{min} = h - \Delta$. From this one immediately sees that h and Δ take opposite roles. We thus expect the confined state to be energetically favourable over the deconfined state when the shell is sufficiently thin and inhomogeneous, *i.e.* low h and high Δ. This heuristic argument has led us to a systematic study of the energy landscape as a function of defect location. We classify three cases: I) the confined state is the only energy minimum, see Figs. 30a and 31a; II) both the confined and deconfined state are minima, one of them is local and the other is global, see Fig. 30b; III) the deconfined state is the only energy minimum, see Fig. 30c and 31b-c.

3.4.3 *Phase diagram*

We construct a phase diagram as a function of thickness and thickness inhomogeneity. We find that for a given thickness there is a deconfined minimum below a critical value of the relative displacement $\frac{\Delta_c}{h}$, marked green in Fig. 32, which is monotonously increasing with the thickness. The confined state is found to min-
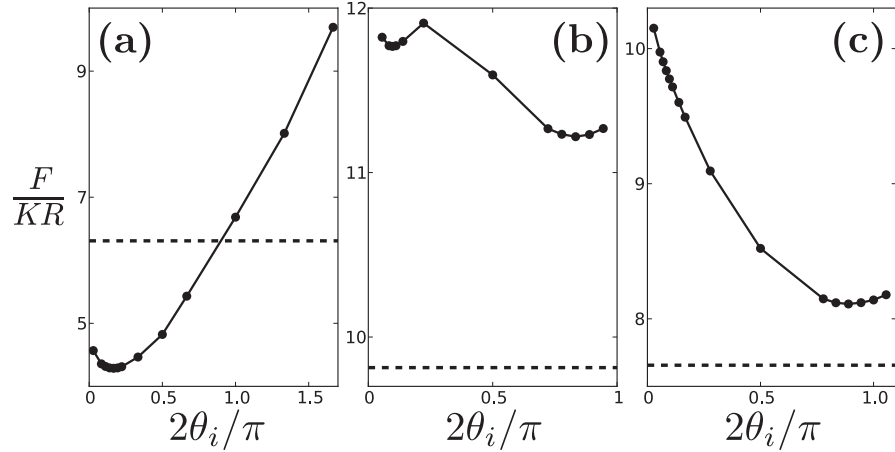
Figure 30: The free energy for a shell as a function of the central angle between two defects on the outer surface in the confined configuration, when (a) $\frac{h}{R} = 0.2$ and $\frac{\Delta}{h} = 0.831$, (b) $\frac{h}{R} = 0.7$ and $\frac{\Delta}{h} = 0.939$, (c) $\frac{h}{R} = 0.8$ and $\frac{\Delta}{h} = 0.946$. Note that for $2\theta_i = \pi$ the defects are aligned horizontally, rather than vertically as in the deconfined conformation. The dashed line indicates the energy of the deconfined configuration. These graphs suggest a confined global minimum at $\frac{\theta}{\pi} \approx 0.17$ in (a), a local confined minimum at $\frac{\theta}{\pi} \approx 0.1$ and a global deconfined minimum in (b) and a global deconfined minimum in (c).

imise the energy (at least) locally above another critical value, $\frac{\Delta_d}{h}$, marked in purple in Fig. 32, which is also larger for thicker shells. Therefore, as anticipated in the previous section, we find that the confined defect state minimises the elastic energy for thin and inhomogeneous shells, whereas the deconfined defect state minimises the energy for rather homogeneous and thick shells. Since these two critical values for $\frac{\Delta}{h}$ are different there exist two minima for $\frac{\Delta_d}{h} < \frac{\Delta}{h} < \frac{\Delta_c}{h}$. We can thus divide the phase diagram into three regions: a deconfined minimum-only, confined minimum-only and coexisting region coloured purple, green and blue in Fig. 32, respectively. These phases are separated by lines marking where, as in a first-order phase transition, a local energy minimum is lost. We remark that the energy differences between the deconfined and weakly confined states for thin and homogeneous shells become too small to conclude with certainty that $\frac{\Delta_c}{h}$ goes to a finite value and the deconfinement transition reaches $\frac{\Delta_d}{h} = 0$ at extremely low h.
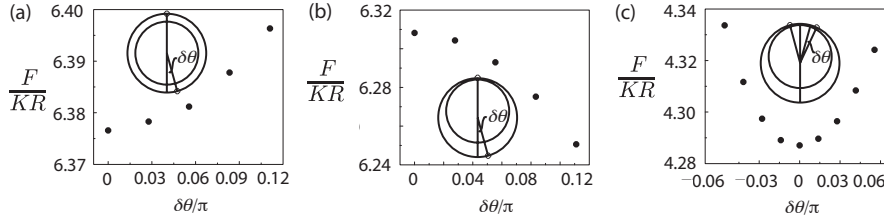
Figure 31: (a) Free energy of a shell of uniform thickness with $h/R = 0.2$, as a function of the angular perturbation of one of the two pairs of defects, $\delta\theta$. When $\Delta = 0$ the inner and outer drops are concentric and $\theta_{12} = \pi$ minimises the free energy irrespective of thickness. (b) Free energy of a shell with $\Delta/h = 0.831$, as a function of $\delta\theta$. In this case, the $\theta_{12} = \pi$ arrangement no longer minimizes the free energy. (e) Free energy as a function of the angular perturbation from the elastic-energy minimum, which is located at $30°$ for the shell in (b).

3.4.4 *Comparison with experiment*

In this section we make a comparison with the experiments on nematic double emulsion droplet performed in the lab of Alberto Fernandez-Nieves. The nematic double emulsion droplets create inhomogeneous shells, because buoyancy displaces the inner droplet upward from its concentric position along the gravitational direction. The short-range steric repulsion from the polymer polyvinyl alcohol (PVA), prevents the inner droplet from coalescing with the continuous phase [56, 41]. Therefore, we assume that the thinnest part of the shell, h_{min}, is effectively constant. By osmosis the thickness inhomogeneity can be modified. We find

$$\frac{\Delta}{h} = 1 - \frac{u_0}{u} \sqrt[3]{\frac{1 - (1 - u)^3}{1 - (1 - u_0)^3}} \tag{140}$$

where $u \equiv \frac{h}{R}$ and u_0 is the value of u when the shell becomes homogeneous, see appendix C. This path through the phase diagram is indicated in red in Fig. 32. If we traverse this path in the direction of decreasing thickness we find that the angular separation between the defects, θ_{12}, changes abruptly from π to a value much smaller than that, as does the order parameter in a first-order phase transition. In the model this occurs in both theory (red squares in Fig. 33) at $u/u_0 \approx 30$ and in the experiment
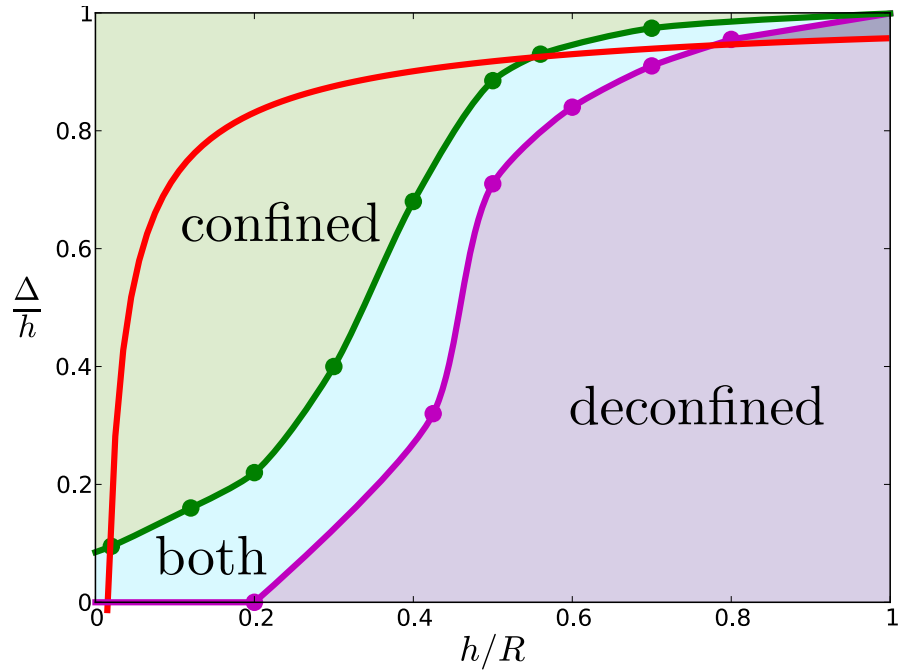
Figure 32: Phase diagram of the confined (green), deconfined (purple) and coexistence phase (blue) as a function of thickness of the shell, $\frac{h}{R}$, and thickness inhomogeneity, $\frac{\Delta}{h}$. The confinement (green), $\frac{\Delta_c}{h}$, and deconfinement (purple), $\frac{\Delta_d}{h}$, transition lines separate these phases. The red line represents the assumed experimental trajectory of constant h_{min}.

(black circles in Fig. 33) at $u/u_0 \approx 20$. The abruptness of the confinement transition is marked by the the short timescale of only tens of seconds, compared to the hours over which the osmosis occurs, in which the pair of defects located at the thicker hemisphere moves toward the top of the shell (see Fig. 34). Upon decreasing the thickness and consequently the thickness inhomogeneity even further the defects spread and the angular separation increases again. When the shell is approximately homogeneous (Fig. 35a), the effect of confinement has weakened so much that the defects are aligned antipodally. The axis joining them can now point in any direction though, as shown by the two shells in Figs. 35b and 35c. In this case, the energy of the thin shell does not depend on the orientation of this axis, in contrast to what happens for thicker shells, whose boojums axis are aligned along the gravitational direction. This also confirms that the defect deconfinement transition in the phase diagram goes to $\Delta = 0$ for low h. Upon
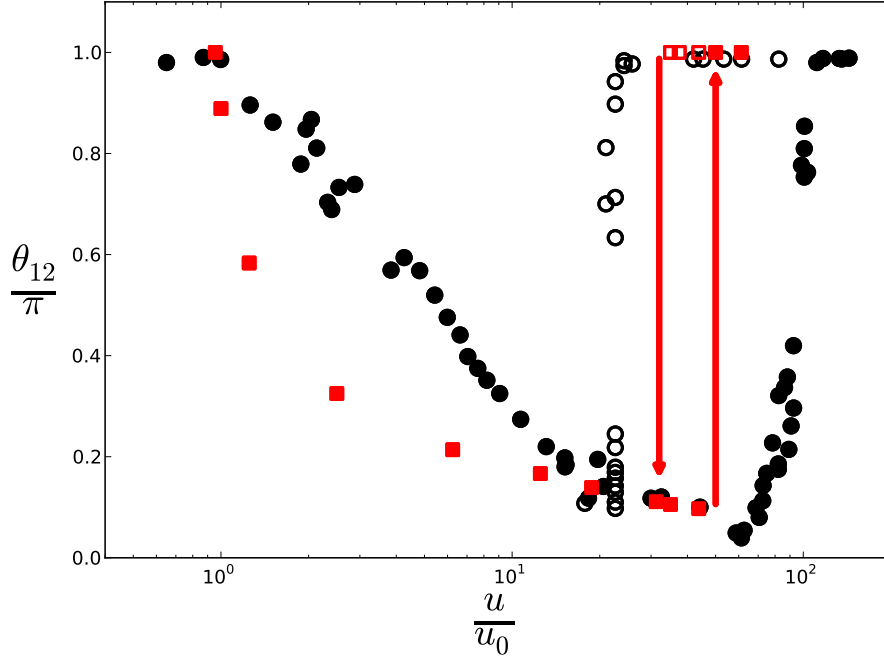
Figure 33: Angular separation between the defects as a function of normalised shell thickness, u/u_0, in the experiment (black circles) [41] and in theory (red squares). An increase (decrease) of u/u_0 is established by shrinking (expanding) the inner water droplet. The open symbols depict the hysteresis.

reversing the path through the phase diagram, *i.e.* traverse the red path in Fig. 32 in the direction of increasing thickness, we first find that the defects move toward each other gradually. Upon increasing the thickness even further we find that θ_{12} increases rapidly to its maximum possible value at $\frac{u}{u_0} \approx 50$ and $\frac{u}{u_0} \approx 80$ in the model and experiment, respectively, as the mutual repulsion between the pairs of defects becomes too large. It is thus favourable to have one pair of boojums at the thickest part of the shell. Note that the thickness at which this deconfinement transition occurs is thus larger than the thickness at which the confinement transition occurs. This hysteresis between the confinement and deconfinement transitions is due to phase coexistence. The green and purple curves in Fig. 32 (corresponding to the confinement and deconfinement transition) intersect the red curve (assumed experimental path) at different points in the phase diagram. Finally, we remark that we have not observed any splitting of the defects into
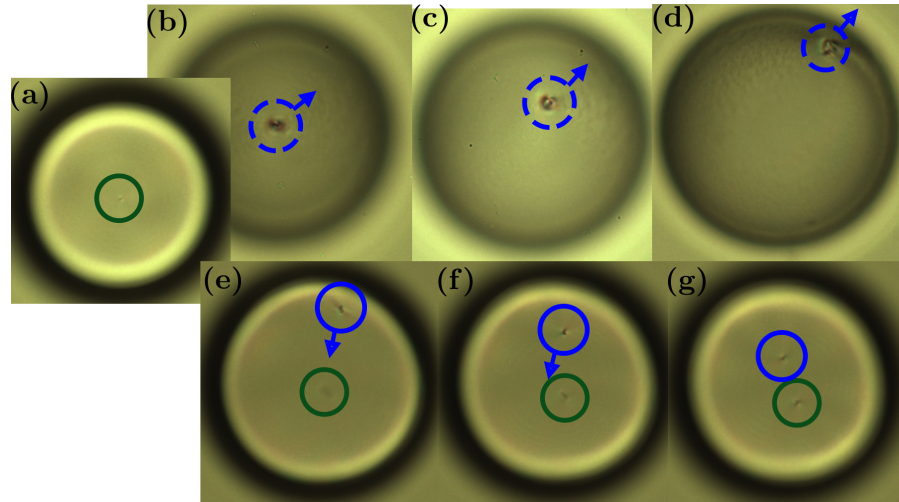
Figure 34: Bright field images of a shell (top view) undergoing the con-
finement transition. (a) One defect pair, encircled in green,
is at the top of the shell before the transition. The other pair
of boojums, encircled in blue, moves from the lower hemi-
sphere in (b)-(d) to the upper hemisphere in (e)-(g).The ar-
row indicates the direction of motion. The circle is dashed if
the defect pair is located in the lower hemisphere. The time
span is tens of seconds. $2R = 133~\mu m$ and $2a = 125~\mu m$.
Ref. [41].

disclination lines of charge one-half during this process of shell
thinning and thickening.

3.5 CONCLUSION

In this study, we have crossed from a two-dimensional description
of a spherical nematic liquid crystal to a spherical divalent shell
with a finite thickness and possible inhomogeneity. Irrespective of
thickness, we always find an antipodal arrangement as the free
energy minimum in homogeneous shells of nematic liquid crystals.
However, this scenario changes when the shell thickness is suffi-
ciently inhomogeneous. The repulsion between the pairs of boo-
jums competes with the minimisation of the distance between the
defects within a pair. As a result, the defects undergo a confine-
ment transition to the thinnest part of the shell. Conversely, the
defects confined in the thinner hemisphere make a deconfinement
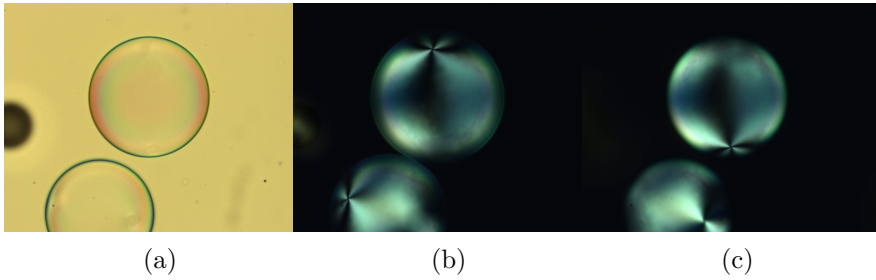transition that maximises their separation. The critical displace-

(a)   (b)   (c)

Figure 35: (a) Bright field image of two thin shells obtained after osmot-
ically shrinking the corresponding thicker shells. The loca-
tion of the defects are easily seen in cross-polarisation by (b)
focusing the shells at the top, to see the upper pair of boo-
jums, and (c) at the bottom, to see the lower pair of boojums.
The defects are a diameter away, with $\theta_{12} = \pi$. Interestingly,
for these thin shells, the direction of the axis joining the two
pairs of boojums is not correlated with the gravitational z-
axis. The dimensions of the upper shell are $2R = 138.8\ \mu m$
and $2a = 137.5\ \mu m$, corresponding to $u/u_0 = 1.05$. Ref.
[41].

ment of the inner droplet for which these transitions occur are
in general not equal, i.e. there is hysteresis present. These tran-
sitions are also present in our experiment, where a water droplet
encapsulates a nematic liquid crystal droplet to make a spherical
nematic shell. We have showed that these shells are inhomoge-
neous due to the buoyancy that displaces the inner droplet along
the gravitational direction. Additional to the confinement and de-
confinement transitions, a continuous evolution is observed, when
thin shells become less inhomogeneous. Though we found an excel-
lent qualitative agreement between theory and experiment for all
these phenomena, an exact quantitative agreement is still lacking,
possibly due to a lack of validity of the one-constant approxima-
tion. It would be interesting to extend this study by investigating
the role of elastic anisotropy on the defect transitions in nematic
shells. Since it is more difficult to exchange splay and bend when
the defects are confined, there will be more distortions of the type
weighted with the largest Frank constant in this state and we ex-
pect that the region in the phase diagram occupied by the confined
state will be smaller if elastic anisotropy is included. This would
imply that the confinement and deconfinement transitions occur

at smaller thickness if $K_1 \neq K_3$. It should be noted though that the *Ansatz* will no longer be accurate if the elastic anisotropy is large. Finally, it would be worthwhile to pursue a study on chirality in nematic shells, because chirality can emerge spontaneously in geometrically confined liquid crystals (see chapter 4).

Part II

TOROIDAL NEMATICS

In this part, we present a theoretical study of director fields in toroidal (rather than spherical) geometries with degenerate planar boundary conditions. In contrast to spherical nematics in Part I, the topology does not induce defects in nematic toroids. However, we do find spontaneous chirality: despite the achiral nature of nematics the director configuration shows a handedness if the toroid is thick enough. In the chiral state the director field displays a double twist, whereas in the achiral state there is only bend deformation. The critical thickness increases as the difference between the twist and saddle-splay moduli grows. A positive saddle-splay modulus prefers alignment along the meridians of the bounding torus, and hence promotes a chiral configuration. The chiral-achiral transition mimics the order-disorder transition of the mean-field Ising model. The role of the magnetisation in the Ising model is played by the degree of twist. The role of the temperature is played by the aspect ratio of the torus. Remarkably, an external field does not break the chiral symmetry explicitly, but shifts the transition. In the case of toroidal cholesterics, we do find a preference for one chirality over the other – the molecular chirality acts as a field in the Ising analogy. Remarkably, an external field does not break the chiral symmetry explicitly, but shifts the transition. Finally, we compare theoretical findings with experimental observations of chirality in toroidal nematic droplets.

CHIRAL SYMMETRY BREAKING

4.1 INTRODUCTION

The liquid crystal in a common display is twisted due to the orientation of the molecules at the confining glass plates. By manipulating this twist using electric fields, an image can be generated. More exotic structures can emerge when the liquid crystal is confined by curved rather than flat surfaces. The topology and geometry of the bounding surface can drive the system into structures that would not be achieved without the presence of external fields. In this sense, the shape of the surface plays a role akin to that of an external field. Thus, under confinement by curved surfaces, the molecules can self-assemble into complex hierarchical structures with emergent macroscopic properties not observed for flat liquid crystal cells. However, the design principles and properties of structures generated by this geometric route are still largely unknown. As discussed in Part I, spherical nematics have been widely studied from experimental, theoretical, and simulation points of view and their intriguing technological potential for divalent nanoparticle assembly has been already demonstrated [20]. In contrast, there are virtually no controlled experiments with ordered media in confined volumes with handles, even though there has been much interest in the interplay between order and toroidal geometries [94, 7, 43, 28, 27, 6, 114, 84, 10]. Alberto Fernanez-Nieves and co-workers experimentally generate stable toroidal droplets of a nematic liquid crystal, using a continuous host with a yield stress. This approach allows them to perform unique experiments that probe nematic materials confined within droplets that are topologically different from the sphere. We observe that the toroidal nematic droplets formed are defect-free. However, polarised microscopy reveals a twisted nematic orientation in droplets with planar degenerate (tangential) boundary conditions, despite the achiral nature of nematics. This phenomenon, which we will iden-

tify as spontaneous chiral symmetry breaking[1], is subject of theoretical study in this chapter. The chirality of nematic toroids is displayed by the the local average orientation of the nematic molecules, called the director field and indicated by the unit vector $\mathbf{n}$. Motivated by experiment, we will assume this director field to be aligned in the tangent plane of the bounding torus. Fig. 36a shows an achiral nematic toroid which has its fieldlines aligned along the azimuthal direction, $\hat{\phi}$. In contrast, the chiral nematic toroids in Figs. 36b and 36c show a right and left handedness, respectively, when following the fieldlines anticlockwise (in the azimuthal direction). The origin of the chirality lies in two elastic ef-
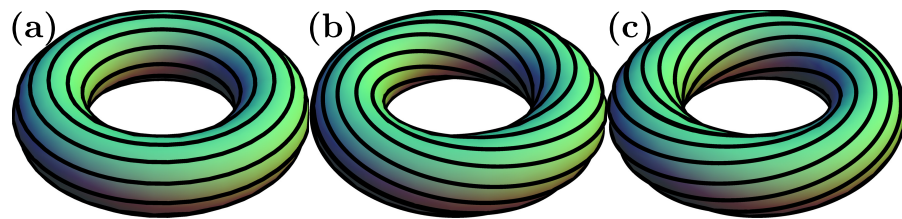

Figure 36: Schematic of (a) achiral, (b) righthanded and (c) lefthanded toroidal nematic liquid crystals. The black lines are director field lines on the bounding torus.

fects of geometric confinement. Firstly, there is a trade-off between bend and twist deformations. Secondly, another type of director distortion called saddle-splay couples the director to the curvature of the boundary, and can consequently favour the chiral state.

These nematic toroids share similarites with polymer bundles [5, 43, 61, 48, 60, 87, 31]. In fact, twisted DNA toroids have been analysed with liquid crystal theory [43, 99, 87]. Under the appropriate solvent conditions DNA condenses into toroids [53, 5]. These efficient packings of genetic material are interesting as vehicles in therapeutic gene delivery; it has been argued [43] that a twist in DNA toroids, for which there are indications both in simulations [96, 98] and experiments [14], would unfold more slowly and could therefore be beneficial for this delivery process. Thus, besides a way to engineer complex structures, the theory of geometrically confined liquid crystals may also provide understanding of biological systems.

---

1 Technically, it is spontaneous *achiral* symmetry breaking since the symmetry is the *lack* of chirality. However, we will conform to the standard convention.

The organisation of this chapter is as follows. In section 4.2 we will discuss our calculational method which involves a single variational *Ansatz* only for the director fields of both chiral and achiral toroidal nematics. In section 4.3 we will consider its energetics in relation to the slenderness, elastic anisotropies, cholesteric pitch and external fields, and discuss the achiral-chiral transition in the light of the mean field treatment of the Ising model. In section 4.4 we compare these theoretical results with experimental measurements of the twist in toroidal nematic droplets. Finally, we conclude in section 4.5.

4.2 TOROIDAL DIRECTOR FIELDS

4.2.1 *Free energy of a nematic toroid*

We will study the general case in which the director lies in the tangent plane of the boundary assuming that the anchoring is strong so that the only energy arises from elastic deformations captured by the Frank free energy functional [18, 40]:

$$
\begin{aligned}
F[\mathbf{n}\left(\mathbf{x}\right)] = \frac{1}{2} \int \mathrm{d}V \Big(&K_1 \left(\nabla \cdot \mathbf{n}\right)^2 \\
&+ K_2 \left(\mathbf{n} \cdot \nabla \times \mathbf{n}\right)^2 + K_3 \left(\mathbf{n} \times \nabla \times \mathbf{n}\right)^2\Big) \\
&- K_{24} \int \mathrm{d}\mathbf{S} \cdot \left(\mathbf{n}\nabla \cdot \mathbf{n} + \mathbf{n} \times \nabla \times \mathbf{n}\right),
\end{aligned}
\tag{141}
$$

where $\mathrm{d}\mathbf{S} = \boldsymbol{\nu}\, \mathrm{d}S$ is the area element, with $\boldsymbol{\nu}$ the unit normal vector (outward pointing) and where $\mathrm{d}V$ is the volume element. Due to the anisotropic nature of the nematic liquid crystal, this expression contains three bulk elastic moduli, K_1, K_2, K_3, rather than a single one for fully rotationally symmetric systems. In addition, there is a surface elastic constant K_{24}. K_1, K_2, K_3 and K_{24} measure the magnitude of splay, twist, bend and saddle-splay distortions, respectively. We now provide a geometrical interpretation of the saddle-splay distortions. Firstly, observe that under perfect planar anchoring conditions $\mathbf{n} \cdot \boldsymbol{\nu} = 0$ and so the first term in the saddle-splay energy does not contribute:

$$
F_{24} = -K_{24} \int \mathrm{d}S\, \boldsymbol{\nu} \cdot \left(\mathbf{n} \times \nabla \times \mathbf{n}\right).
\tag{142}
$$

This remaining term in the saddle-splay energy is often rewritten as

$$F_{24} = K_{24} \int \mathrm{d}S \, \boldsymbol{\nu} \cdot (\mathbf{n} \cdot \nabla) \, \mathbf{n}. \tag{143}$$

because

$$
\begin{aligned}
(\mathbf{n} \times \nabla \times \mathbf{n})_a &= \epsilon_{abc} n_b \epsilon_{cpq} \partial_p n_q \\
&= (\delta_{ap}\delta_{bq} - \delta_{aq}\delta_{bp}) \, n_b \partial_p n_q \\
&= -n_b \partial_b n_a,
\end{aligned}
\tag{144}
$$

where in the last line one uses that $0 = \partial_a (1) = \partial_a (n_b n_b) = 2 n_b \partial_a n_b$. In other words, the bend is precisely the curvature of the integral curves of $\mathbf{n}$. Employing the product rule of differention $0 = \partial_a (\nu_b n_b) = \nu_b \partial_a n_b + n_b \partial_a \nu_b$ yields

$$F_{24} = -K_{24} \int \mathrm{d}S \, \mathbf{n} \cdot (\mathbf{n} \cdot \nabla) \, \boldsymbol{\nu}. \tag{145}$$

Upon writing $\mathbf{n} = n_1 \boldsymbol{e}_1 + n_2 \boldsymbol{e}_2$, with $\boldsymbol{e}_1$ and $\boldsymbol{e}_1$ two orthonormal basis vectors in the plane of the surface, one obtains

$$F_{24} = K_{24} \int \mathrm{d}S \, n_i L_{ij} n_j, \tag{146}$$

where we note that $i, j = 1, 2$ (rather than running till 3). Thus the nematic director couples to the extrinsic curvature tensor [37], defined as

$$L_{ij} = -\boldsymbol{e}_i \cdot (\boldsymbol{e}_j \cdot \nabla) \, \boldsymbol{\nu}. \tag{147}$$

If $\boldsymbol{e}_1$ and $\boldsymbol{e}_2$ are in the directions of principal curvatures, κ_1 and κ_2, respectively, one finds

$$F_{24} = K_{24} \int dS \left(\kappa_1 n_1^2 + \kappa_2 n_2^2 \right). \tag{148}$$

We conclude that the saddle-splay term favours alignment of the director along the direction with the smallest principal curvature if $K_{24} > 0$. The controversial surface energy density $K_{13}\mathbf{n}\nabla \cdot \mathbf{n}$ is sometimes incorporated in eq. (141), but is in our case irrelevant, because the normal vector is perpendicular to $\mathbf{n}$, and so $\mathbf{n} \cdot \boldsymbol{\nu} = 0$.

We will consider a nematic liquid crystal confined in a handle body bounded by a torus given by the following implicit equation for the cartesian coordinates x, y, and z:

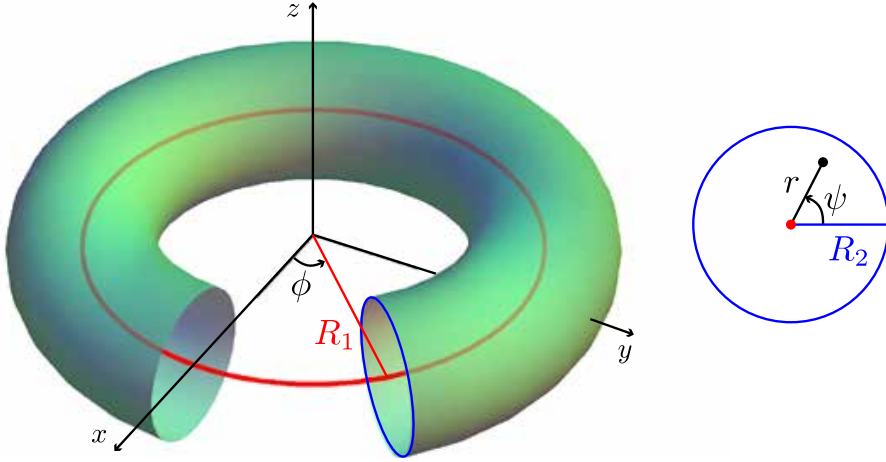$$\left(R_1 - \sqrt{x^2 + y^2} \right)^2 + z^2 \leq R_2^2. \tag{149}$$

Figure 37: *Left panel*: Schematic of the boundary of the geometry spec-
ified eq. (149) including graphical definitions of ϕ and R_1.
The torus characterised by a large (red) and a small (blue)
circle. The large circle, or centerline, has radius R_1. *Right
panel*: Schematic of a cut including graphical definitions of
r, ψ and R_2.

Here, R_1 and R_2 are the large and small radii, respectively, of
the circles that characterise the outer surface: a torus obtained
by revolving a circle of radius R_2 around the z-axis (Fig. 37). We
can conveniently parametrise this solid torus by the coordinates
$r \in [0, R_2]$, $\phi \in [0, 2\pi)$ and $\psi \in [0, 2\pi)$ (illustrated in Fig. 37):

$$x = (R_1 + r \cos \psi) \cos \phi, \tag{150}$$

$$y = (R_1 + r \cos \psi) \sin \phi, \tag{151}$$

$$z = r \sin \psi. \tag{152}$$

The metric reads:

$$g_{\mu\nu} = \begin{pmatrix} 1 & 0 & 0 \\ 0 & (R_1 + r \cos \psi)^2 & 0 \\ 0 & 0 & r^2 \end{pmatrix}, \tag{153}$$

with $\mu, \nu \in \{r, \phi, \psi\}$. It follows that $\mathbf{dS} = \boldsymbol{\nu} \sqrt{g}\, d\psi\, d\phi$ and $dV = \sqrt{g}\, dr\, d\psi\, d\phi$, where $g = \det g_{\mu\nu}$.

For a torus the ϕ and ψ directions are the principal directions.
The curvature along the ψ direction is everywhere negative (mea-
sured with respect to the outward pointing normal) and the small-
est of the two, so when $K_{24} > 0$, the director tends to wind along
the small circle with radius R_2 (*i.e.* meridian).

4.2.2   *Double twist*

To minimise the Frank energy we formulate a variational *Ansatz* built on several simplifying assumptions [43]. We consider a director field which has no radial component (*i.e.* $n_r = 0$), is tangential to the centerline ($r = 0$), and is independent of ϕ. Furthermore, since we expect the splay (K_1) distortions to be unimportant, we first take the field to be divergence free (*i.e.* $\nabla \cdot \mathbf{n} = 0$). Recalling that in curvilinear coordinates the divergence is $\nabla \cdot \mathbf{n} = \frac{1}{\sqrt{g}} \partial_\mu \left(\sqrt{g} n^\mu \right)$, we write :

$$n_\psi = \frac{f\left(r\right) R_1}{\sqrt{g_{\phi\phi}}}, \tag{154}$$

where the other terms in $\sqrt{g}$ play no role as they are independent of ψ. The ϕ-component of the director follows from the normalisation condition. For the radial dependence of $f\left(r\right)$ we make the simplest choice:

$$f\left(r\right) = \frac{\omega r}{R_2}, \tag{155}$$

and obtain

$$n_\psi = \omega \frac{\xi r / R_2}{\xi + \frac{r}{R_2} \cos \psi}, \tag{156}$$

where we have introduced $\xi \equiv R_1 / R_2$, the slenderness or aspect ratio of the torus. The variational parameter ω governs the chirality of the toroidal director field. If $\omega = 0$ the director field corresponds to the axial configuration (Fig 36a). The sign of ω determines the chirality: right handed when $\omega > 0$ (Fig. 36c) and left handed when $\omega < 0$ (Fig. 36b). The magnitude of ω determines the degree of twist. Note that the direction of twist is in the radial direction, as illustrated in Fig. 38. Therefore the toroidal nematic is doubly twisted, resembling the cylindrical building blocks of the blue phases [18, 40]. It may be useful to relate ω with a quantity at the surface, say the angle, α, that the director makes with $\hat{\phi}$. For the *Ansatz*, this angle will be different depending on whether one measures at the inner or outer part of the torus, but for large ξ we find

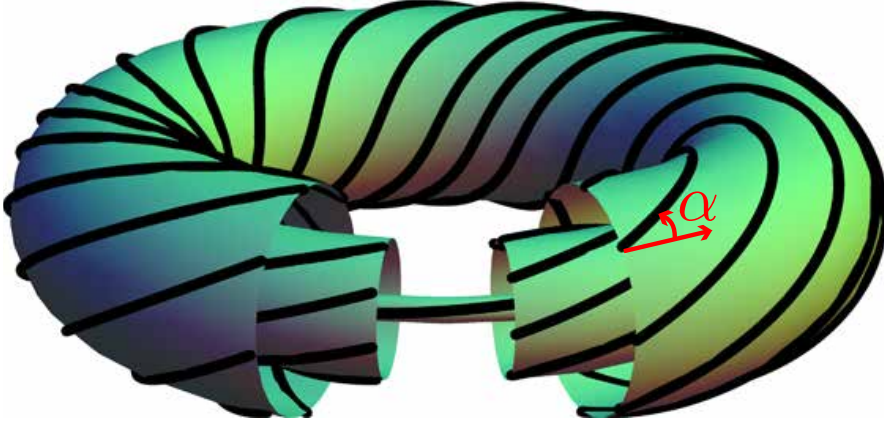$$\omega \approx n_\psi \left(r = R_2\right) = \sin \alpha. \tag{157}$$

Figure 38: Schematic of the *Ansatz* for the director fieldlines ($\omega = 0.6$ and $\xi = 3$), displaying a twist when going radially outward, including a graphical definition of α.

4.3 CHIRAL SYMMETRY BREAKING

4.3.1 *Results for divergence-free field*

Since ω only determines the chirality of the double-twisted configuration but not the amount of twist, the free energy is invariant under reversal of the sign of ω, *i.e.* $F(-\omega) = F(\omega)$. This mirror symmetry allows us to write down a Landau-like expansion in which F only contains even powers of ω,

$$F = a_0\left(\{K_i\}, \xi\right) + a_2\left(\{K_i\}, \xi\right)\omega^2 + a_4\left(\{K_i\}, \xi\right)\omega^4$$
$$+ \mathcal{O}\left(\omega^6\right) \tag{158}$$

where $\{K_i\} = \{K_1, K_2, K_3, K_{24}\}$, the set of elastic constants. If the coefficient $a_2 > 0$, the achiral nematic toroid ($\omega_{eq} = 0$) corresponds to the minimum of F provided that $a_4 > 0$. In contrast, the mirror symmetry is broken spontaneously whenever $a_2 < 0$ (and $a_4 > 0$). The achiral-chiral critical transition at $a_2 = 0$ belongs to the universality class of the mean-field Ising model. Therefore, we can immediately infer that the value of the critical exponent β in $\omega_{eq} \sim (-a_2)^{\beta}$ is $\frac{1}{2}$. To obtain the dependence of the coefficients a_i

on the elastic constants and ξ, we need to evaluate the integral in eq. (141). We find for the bend, twist and saddle-splay energies:

$$\frac{F_3}{K_3 R_1} = 2\pi^2 \left(\xi - \sqrt{\xi^2 - 1} \right) / \xi$$
$$+ \pi^2 \frac{\xi \left(1 - 9\xi^2 + 6\xi^4 + 6\xi\sqrt{\xi^2 - 1} - 6\xi^3\sqrt{\xi^2 - 1} \right)}{(\xi^2 - 1)^{\frac{3}{2}}} \omega^2$$
$$+ \mathcal{O}\left(\omega^4 \right), \tag{159}$$

$$\frac{F_2}{K_2 R_1} = 4\pi^2 \frac{\xi^3}{(\xi^2 - 1)^{\frac{3}{2}}} \omega^2 + \mathcal{O}\left(\omega^6 \right), \tag{160}$$

$$\frac{F_{24}}{K_{24} R_1} = -4\pi^2 \frac{\xi^3}{(\xi^2 - 1)^{\frac{3}{2}}} \omega^2. \tag{161}$$

Though the bend and twist energies are Taylor expansions in ω, the saddle-splay energy is exact. The large ξ asymptotic behavior of the elastic energy reads[2]:

$$\frac{F}{K_3 R_1} \approx \frac{\pi^2}{\xi^2} + 4\pi^2 \left(k - \frac{5}{16\xi^2} \right) \omega^2 + \frac{\pi^2}{2} \omega^4 + \mathcal{O}\left(\omega^6 \right), \tag{162}$$

where $k \equiv \frac{K_2 - K_{24}}{K_3}$ is the elastic anisotropy in twist and saddle-splay. The achiral configuration contains only bend energy. For sufficiently thick toroids, bend distortions are exchanged with twist and the mirror symmetry is indeed broken spontaneously (Fig. 39). Interestingly, if $K_{24} > 0$ the saddle-splay deformations screen the cost of twist. If $K_{24} < 0$ on the other hand, there is an extra penalty for twisting. Setting the coefficient of the ω^2 term equal to zero yields the phase boundary:

$$k_c = \frac{-1 + 9\xi_c^2 - 6\xi_c^4 - 6\xi_c\sqrt{\xi_c^2 - 1} + 6\xi_c^3\sqrt{\xi_c^2 - 1}}{4\xi_c^2}$$
$$\approx \frac{5}{16\xi_c^2} \qquad \text{if } \xi \gg 1. \tag{163}$$

Fig. 40 shows the phase diagram as a function of ξ and k. It is interesting to look at the critical behavior. The degree of twist close to the transition is

$$\alpha_{eq} \approx \omega_{eq} \approx 2 \left(\frac{5}{16\xi^2} - k \right)^{1/2}, \tag{164}$$

---

2 The fourth order term in the bend energy for general ξ, that reduces to $\frac{\pi^2}{2} K_3 R_2 \xi \omega^4$ in eq. (162), is not given in eq. (159), because it is too lengthy.
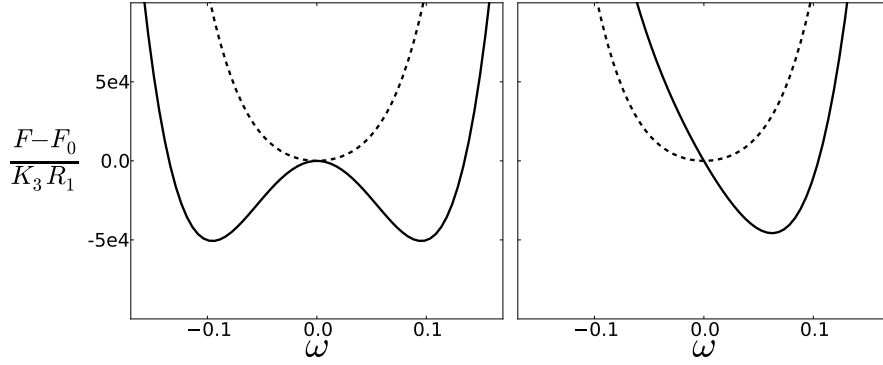
Figure 39: *Left panel:* The free energy as a function of ω for $\xi = 6$ (dashed) and $\xi = 5$ (solid), when $(K_2 - K_{24})/K_3 = 10^{-2}$. For $\xi = 5$ the chiral symmetry is broken spontaneously: the minimum values of the energy occurs for a nonzero ω. *Right panel:* The free energy as a function of ω for $q = 0$ (dashed) and $qR_2 = 10^{-3}$ (solid), when $\xi = 6$, $(K_2 - K_{24})/K_3 = 10^{-2}$ and $K_2/K_3 = 0.3$. For $qR_2 = 10^{-3}$ the chiral symmetry is broken explicitly: the minimum value of the energy occurs for a nonzero ω, because F contains a term linear in ω.

where we have used that $\sin \alpha_{eq} \approx \alpha_{eq}$ for small α_{eq}. Upon expanding $\xi = \xi_c + \delta\xi$ (with $\delta\xi < 0$) and $k = k_c + \delta k$ (with $\delta k < 0$) around their critical values ξ_c and k_c, respectively, we obtain the following scaling relations:

$$\alpha_{eq} \approx \frac{\sqrt{5}}{2} \left(-\frac{\delta\xi}{\xi_c^3} \right)^{1/2} \tag{165}$$

$$\alpha_{eq} \approx 2 \left(-\delta k \right)^{1/2} \tag{166}$$

while keeping k and ξ fixed, respectively. Eqs. (165) and (166) are analogues to $m_{eq} \sim (-t)^{1/2}$, relating the equilibrium magnetisation, m_{eq} (in the ferromagnetic phase of the Ising model in Landau theory), to the reduced temperature, t.

4.3.2 *Effects of external fields and cholesteric pitch*

Due to the inversion symmetry of nematics, $F[\mathbf{n}] = F[-\mathbf{n}]$, an external magnetic field, $\mathbf{H}$, couples quadratically to the compo-
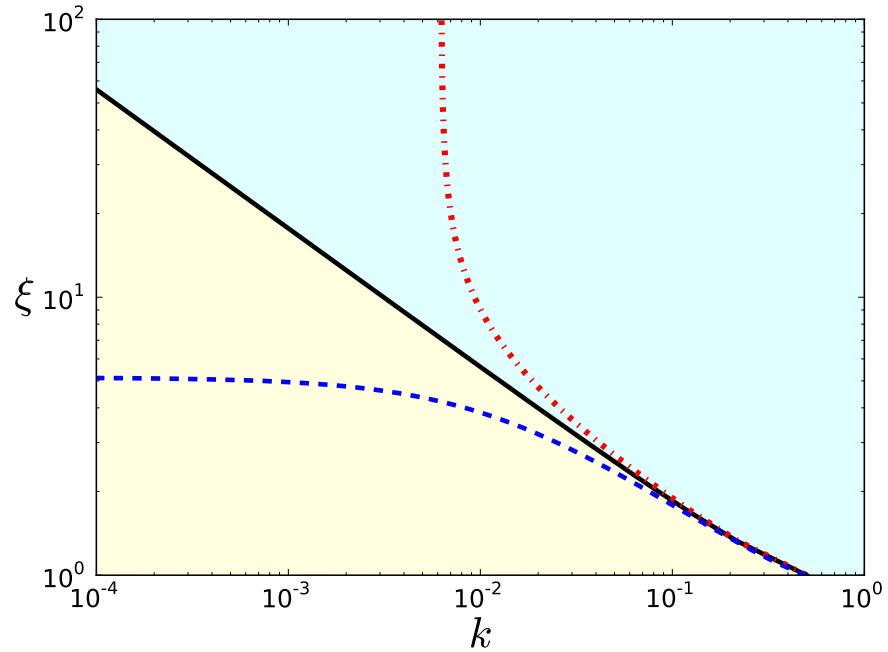
Figure 40: Phase diagram as a function of the toroidal slenderness and the elastic anisotropy in twist and saddle-splay constant, $k \equiv (K_2 - K_{24})/K_3$. The twisted (yellow region) and axial (cyan region) configuration are separated by a boundary line in the absence of an external field (solid black), when $\mathbf{H} = \sqrt{0.1 K_3}/\left(\sqrt{\chi_a} R_2\right) \hat{\boldsymbol{\phi}}$ (dashed blue) and when $\mathbf{H} = \sqrt{0.1 K_3}/\left(\sqrt{\chi_a} R_2\right) \hat{\mathbf{z}}$ (dash-dotted red).

nents of $\mathbf{n}$ rather than linearly as in spin systems. The magnetic free energy contribution reads:

$$F_m = -\frac{\chi_a}{2} \int \mathrm{d}V \left(\mathbf{n} \cdot \mathbf{H}\right)^2, \tag{167}$$

where $\chi_a = \chi_\parallel - \chi_\perp$, the difference between the magnetic susceptibilities parallel and perpendicular to $\mathbf{n}$. Consequently, there is no explicit chiral symmetry breaking due to $\mathbf{H}$ as is the case in the Ising model. Rather, $\mathbf{H}$ shifts the location of the critical transition in the phase diagram. For concreteness, we will consider two different applied fields, namely a uniaxial field $\mathbf{H} = H_z \hat{\mathbf{z}} = H_z \sin(\psi) \hat{\mathbf{r}} + H_z \cos(\psi) \hat{\boldsymbol{\psi}}$ and an azimuthal field $\mathbf{H} = H_\phi \hat{\boldsymbol{\phi}}$, as

if produced by a conducting wire going through the hole of the toroid. For $\mathbf{H} = H_z\hat{\mathbf{z}}$ we find

$$F_m = -\pi^2 \chi_a H_z^2 R_1 R_2^2 \xi^2 \left(2\xi \left(\xi - \sqrt{\xi^2 - 1} \right) - 1 \right) \omega^2$$

$$\approx -\frac{\pi^2}{4} \chi_a H_z^2 R_1 R_2^2 \omega^2 \qquad \text{if } \xi \gg 1. \tag{168}$$

For a positive χ_a this energy contribution is negative, implying that a larger area in the phase diagram is occupied by the twisted configuration. The new phase boundary (Fig. 40), which is now a surface in the volume spanned by ξ, k and H_z instead of a line, reads:

$$k_c = \left[-1 + 9\xi_c^2 - 6\xi_c^4 - 6\xi_c\sqrt{\xi_c^2 - 1} + 6\xi_c^3\sqrt{\xi_c^2 - 1} \right.$$

$$- \frac{\chi_a (H_z)_c^2 R_2^2}{K_3} \left(\xi_c^2 - 1 \right) \xi_c$$

$$\left. \times \left(-2\xi_c + 2\xi_c^3 + \sqrt{\xi_c^2 - 1} - 2\xi_c^2\sqrt{\xi_c^2 - 1} \right) \right] / \left(4\xi_c^2 \right)$$

$$\approx \frac{5}{16\xi_c^2} + \frac{\chi_a (H_z)_c^2 R_2^2}{16 K_3} \quad \text{if } \xi \gg 1. \tag{169}$$

In contrast, an azimuthal field favours the axial configuration, contributing a postive ω^2-term to the energy when $\chi_a > 0$:

$$F_m = -\pi^2 \chi_a H_\phi^2 R_1 R_2^2$$

$$+ \frac{2\pi^2}{3} \chi_a H_\phi^2 R_1 R_2^2 \xi \left(2\xi^2 \left(\xi - \sqrt{\xi^2 - 1} \right) - \sqrt{\xi^2 - 1} \right) \omega^2$$

$$\approx -\pi^2 \chi_a H_\phi^2 R_1 R_2^2 + \frac{\pi^2}{2} \chi_a H_\phi^2 R_1 R_2^2 \omega^2 \quad \text{if } \xi \gg 1. \tag{170}$$

Consequently, this yields a shifted phase boundary (Fig. 40):

$$k_c = \left[-1 + 9\xi_c^2 - 6\xi_c^4 - 6\xi_c\sqrt{\xi_c^2 - 1} + 6\xi_c^3\sqrt{\xi_c^2 - 1} \right.$$

$$- \frac{2\chi_a (H_\phi)_c^2 R_2^2}{3K_3} \left(\xi_c^2 - 1 \right)$$

$$\left. \times \left(1 + \xi_c^2 - 2\xi_c^4 + 2\xi_c^3\sqrt{\xi_c^2 - 1} \right) \right] / \left(4\xi_c^2 \right)$$

$$\approx \frac{5}{16\xi_c^2} - \frac{\chi_a (H_\phi)_c^2 R_2^2}{8 K_3} \qquad \text{if } \xi \gg 1. \tag{171}$$

Similar results (eqs. (168)-(171)) hold for an applied electric field $\mathbf{E}$ instead of a magnetic field; the analog of χ_a is the dielectric anisotropy. There could however be another physical mechanism at

play in a nematic insulator, namely the flexoelectric effect [64, 18]. Splay and bend deformations induce a polarisation

$$\mathbf{P} = e_1 \mathbf{n} \nabla \cdot \mathbf{n} + e_3 \mathbf{n} \times \nabla \times \mathbf{n}, \tag{172}$$

where e_1 and e_3 are called the flexoelectric coefficients. Note that the first term in eq. (172) is irrelevant for the divergence-free *Ansatz*. A coupling of $\mathbf{P}$ with $\mathbf{E}$

$$F_P = - \int dV \mathbf{P} \cdot \mathbf{E} \tag{173}$$

could potentially lead to a shift of the transition. In the particuar case when $\mathbf{E} = E_z \hat{\mathbf{z}} = E_z \sin(\psi)\hat{\mathbf{r}} + E_z \cos(\psi)\hat{\boldsymbol{\psi}}$, however, the ω^2 contribution from eq. (173) vanishes, thus not yielding such a shift.

If we now consider toroidal cholesterics rather than nematics, the chiral symmetry is broken explicitly (Fig. 39). A cholesteric pitch of $2\pi/q$ gives a contribution to the free energy of:

$$F_{cn} = K_2 \, q \int dV \mathbf{n} \cdot \nabla \times \mathbf{n}. \tag{174}$$

Substituting eq. (156) yields

$$
\begin{aligned}
F_{cn} &= -8\pi^2 K_2 \, q \, R_1 R_2 \, \xi \left(\xi - \sqrt{\xi^2 - 1} \right) \omega + \mathcal{O}\left(\omega^3\right) \\
&\approx -4\pi^2 K_2 \, q \, R_1 R_2 \, \omega + \mathcal{O}\left(\omega^3\right) \qquad \text{if } \xi \gg 1.
\end{aligned}
\tag{175}
$$

Therefore, at the critical line in the phase diagram spanned by k and ξ, the degree of twist or surface angle scales (for large ξ) with the helicity of the cholesteric as

$$\alpha_{eq} \approx \left(2K_2 R_2 \, q / K_3\right)^{1/3} \sim q^{1/3}. \tag{176}$$

This is the analog scaling relation of $m_{eq} \sim H^{1/3}$ in the mean-field Ising model.

4.3.3 *Results for the two-parameter Ansatz*

Motivated by experiments (see section 4.4), we can introduce an extra variational paramer γ to allow for splay deformations, in addition to ω:

$$n_\psi = \omega \frac{\xi r / R_2}{\xi + \gamma \frac{r}{R_2} \cos \psi}. \tag{177}$$

(Note that eq. (156) is recovered by setting $\gamma = 1$ in eq. (177).) In subsection 4.3.1 analytical results for $\gamma = 1$ were presented. In this subsection we will slightly improve these results by finding the optimal value of γ numerically. First, we discretise the azimuthally symmetric director field in the r and ψ direction. Next, we compute the Frank free energy density (eq. (141)) by taking finite differences [25] of the discretised nematic field. After summation over the volume elements the Frank free energy will become a function of ω and γ for a given set of elastic constants and a given aspect ratio. Because of the normalisation condition on $\mathbf{n}$, the allowed values for ω and γ are constrained to the open diamond-like interval for which $-\xi < \gamma < \xi$ and $\frac{|\gamma| - \xi}{\xi} < \omega < \frac{\xi - |\gamma|}{\xi}$ holds.
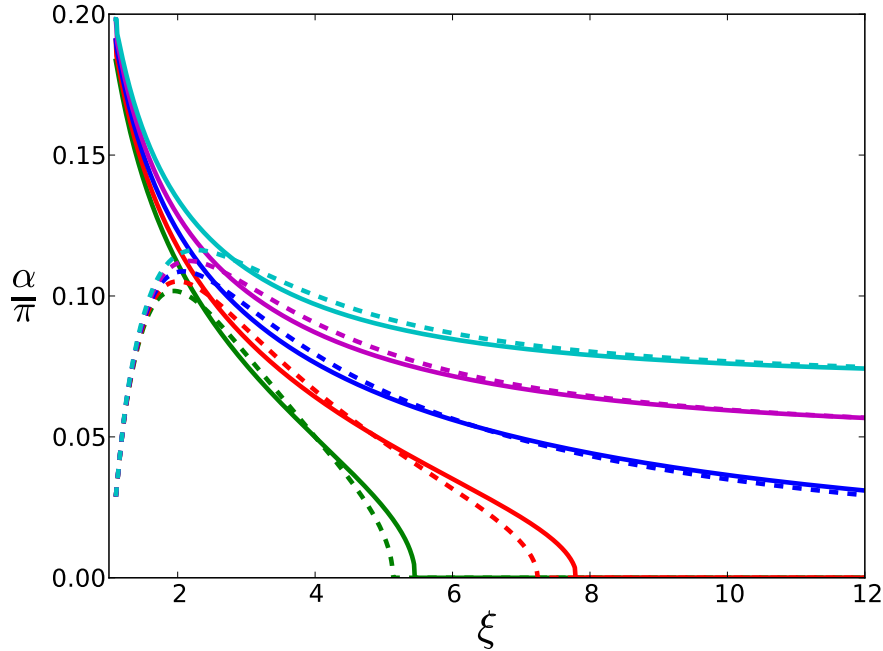

Figure 41: Twist angle α (in units of π) at $\psi = \pi/2$ versus the slenderness ξ for $k = 0.012$ (green), $k = 0.006$ (red), $k = 0$ (blue), $k = -0.006$ (magenta) and $k = -0.012$ (cyan). The dashed lines represent α for $\gamma = 1$, the solid lines represent α found for the optimal γ.

The minima of the energy surface can be found by employing the conjugate gradient method. We have looked at the difference between the $\gamma = 1$ case and the case where the value of γ is chosen to minimise the energy. This was done for various choices of k. We have chosen the material properties of 5CB, i.e. $K_1 = 0.64 K_3$ and $K_2 = 0.3 K_3$ [40]. The value for of K_{24} has not been so accurately
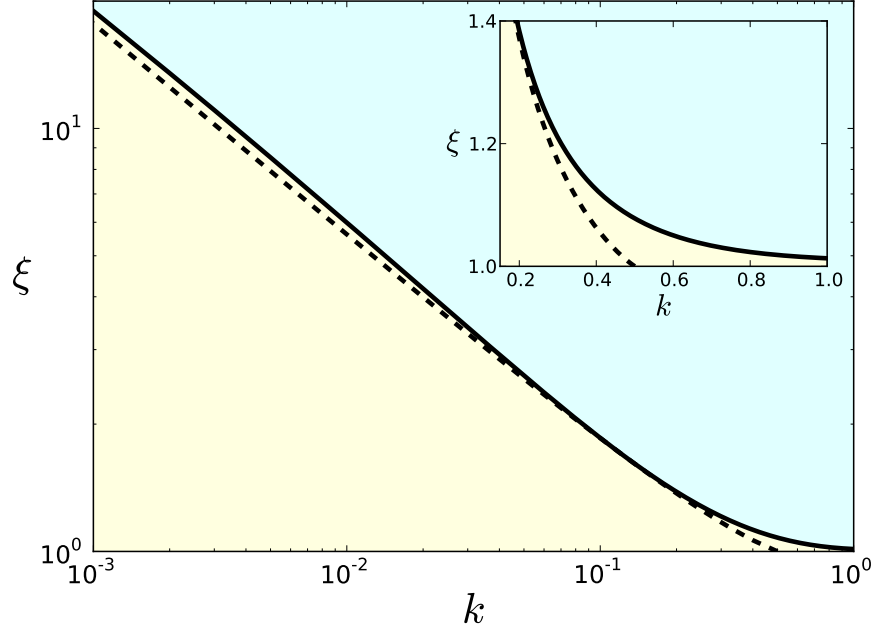
Figure 42: The phase boundary as a function of the toroidal slenderness ξ and elastic anisotropy k for γ as a variational parameter(solid) and for $\gamma = 1$ (dashed). The inset zooms in on the phase boundary for small ξ.

determined, but previous measurements [2, 45, 79, 92, 46, 77] seem to suggest that $K_{24} \approx K_2$, corresponding to $k \approx 0$.

We are interested in how the phase boundary changes by introducing the variational parameter γ. Therefore, the twist angle α, evaluated at the surface of the torus at $\psi = \frac{\pi}{2}$, versus the slenderness ξ is shown in Fig. 41. For the particular choices of k there are two noticeable differences between the single-parameter *Ansatz* and the two-parameter *Ansatz*. Firstly, for small values of ξ, α is changed significantly. Secondly, for larger values of ξ we see that if there is a chiral-achiral phase transition, ξ_c is shifted by a small amount. In Fig. 42 we further investigate how introducing γ influences the phase boundary, by plotting the phase boundary as a function of the toroidal slenderness ξ and elastic anisotropy k for both γ as a variational parameter (solid) and for $\gamma = 1$ (dashed). Observe that, for both the small ξ and small k regime, the difference is significant.

4.4 COMPARISON WITH EXPERIMENT

To make nematic toroidal droplets, Alberto Fernandez-Nieves and co-workers inject a nematic liquid crystal, namely 4-n-pentyl-4'-cyanobiphenyl (5CB), through a needle into a rotating bath containing a yield-stress material consisting of (i) 1.5 wt% polyacrylamide microgels (carbopol ETD 2020), (ii) 3 wt% glycerin, (iii) 30 wt% ethanol, (iv) 1 wt% polyvinyl alcohol (PVA), and (v) 64.5 wt% ultrapure water [77]. The presence of PVA guarantees degenerate tangential (or planar) anchoring for the liquid crystal at the surface of the droplets; they confirmed this by making spherical droplets and checking their bipolar character. We also note that the continuous phase is neutralized to pH 7, where the sample transmission is more than 90% [13]. However, the most relevant property of this phase is its yield stress, σ_y. During formation of the torus, the stresses involved are larger than σ_y and hence the continuous phase essentially behaves as if it were a liquid. The combination of the viscous drag exerted by the outer phase over the extruded liquid crystal and its rotational motion causes the liquid crystal to form a curved jet, as shown in Fig. 43a, which eventually closes onto itself, resulting in a toroidal nematic droplet, such as that shown in Fig. 43b in bright field and in Fig. 43c between cross-polarizers. Once the torus has been formed, the elasticity of the continuous phase provides the required force to overcome the surface tension force that would naturally tend to transform the toroidal droplet into a spherical droplet [76]. Remarkably, when these droplets are observed along their side view under cross-polarizers, their central region remains bright irrespective of the orientation of the droplet with respect to the incident polarization direction, as shown in Fig. 43d-f; the corresponding bright-field images are shown in Fig. 43g-i. Note that for an axial torus with its director field along the tube, the cross-polarized image should appear black for an orientation of 0° and 90° with respect to the incident polarization direction. Hence our result is suggestive of a twisted structure. In fact, twisted bipolar droplets also have a central bright region, when viewed between cross-polarizers, irrespective of their orientation [109, 47, 22, 112].

We then quantify our results by measuring the twist angle in our toroidal droplets along the z direction, from $(r = R_2, \psi = 90°)$ to
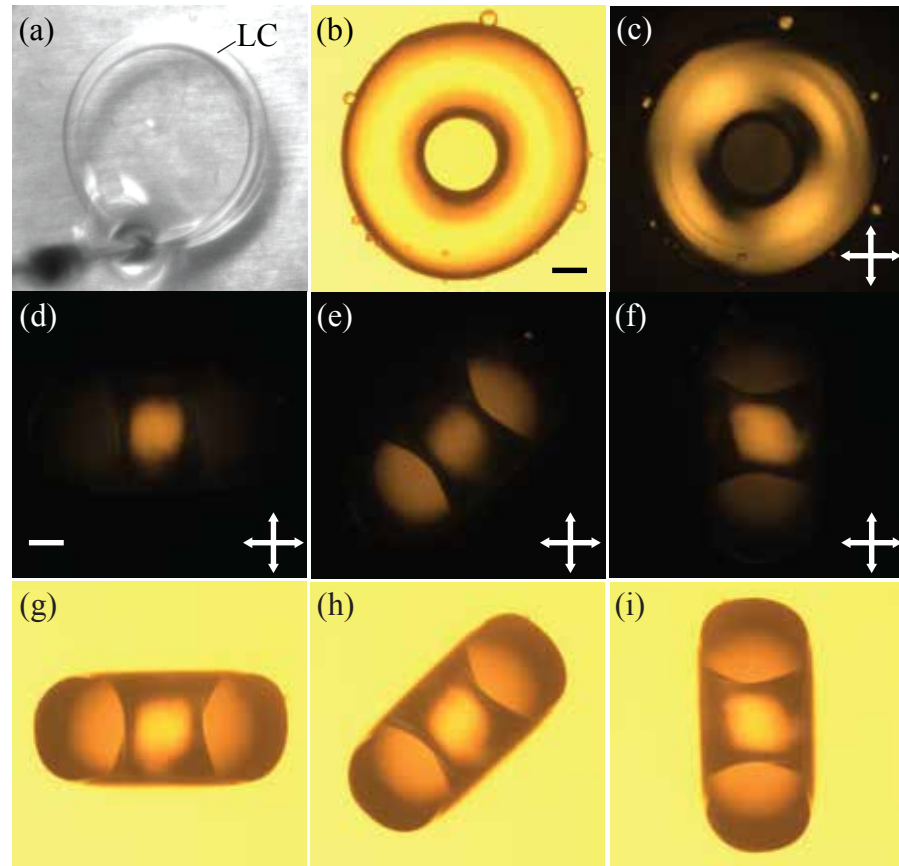
Figure 43: Toroidal droplets. (a) Formation of a toroidal liquid crystal droplet inside a material with yield stress. (b and c) The top view of a typical stable toroidal droplet of nematic liquid crystal is shown in (b) when viewed in bright field and in (c) when viewed under cross-polarizers. (d-f) Side view of a typical toroidal droplet with $\xi = 1.8$ when viewed under cross-polarizers for orientations of 0°, 45°, and 90° with respect to the incident polarization direction. Note that the center part of the toroid remains bright irrespective of its orientation. (g-i) Corresponding bright-field images. The dark regions of the toroid in these images are due to light refraction. (Scale bar: $100\mu m$.) Ref. [77].

$(r = R_2, \psi = 270°)$ (see Fig. 37). The method relies on the fact that linearly polarized light follows the twist of a nematic liquid crystal if the polarization direction is either parallel or perpendicular to the nematic director at the entrance of the sample, provided the Mauguin limit is fulfilled [115]; the corresponding mode of propagation is referred to as extraordinary or ordinary waveguiding, respectively. We then image the torus from above (Fig. 44A), rotate the polarizer to ensure that the incident polarization direction is parallel or perpendicular to the nematic director at $(r = R_2, \psi = 90°)$, and then rotate the analyzer an angle ϕ_{exit} with respect to the polarizer while monitoring the transmitted intensity, T. The minimum in T, shown in Fig. 44B, reflects the lack of light propagation through the analyzer, indicating that the incident polarization direction has rotated an amount τ such that it is perpendicular to the analyzer after exiting the torus at $(r = R_2, \psi = 270°)$. The image of the torus in this situation exhibits four black regions where extinction occurs, as shown in Fig. 44C; these correspond to waveguiding of ordinary and extraordinary waves. It is along these regions that we measure T. The counterclockwise rotation of the incident polarization direction by an angle of $-56°$ exactly corresponds to the twist angle of the nematic along the z direction through the center of the circular cross section. However, to increase the precision of our estimate, we fit the T vs. ϕ_{exit} results to the theoretically expected transmission [115], leaving τ as a free parameter. We find $\tau = (52.9 \pm 0.4)°$ for $\xi = 3.5$. Moreover, within the experimentally accessed ξ-range, we find that the twist is nonzero and that it monotonously decreases with increasing aspect ratio, as shown in Fig. 44D. Remarkably, these features are captured by our theoretical calculations for large ξ, as shown by the dashed line in Fig. 44D. We note that the deviations of the experiment and the theory for small ξ result from the inadequacy of the *Ansatz* in describing the highly twisted structures observed experimentally at these low values of ξ. This can be partially resolved by lifting the constraint that $\gamma = 1$. This introduces a second variational parameter in the *Ansatz*, which allows the nematic field to splay. The result qualitatively captures the experimental trend for all aspect ratios, as shown by the solid line in Fig. 44D. By further comparing the experiment to the theory in the high ξ-region, we obtain a value for the saddle-splay elastic
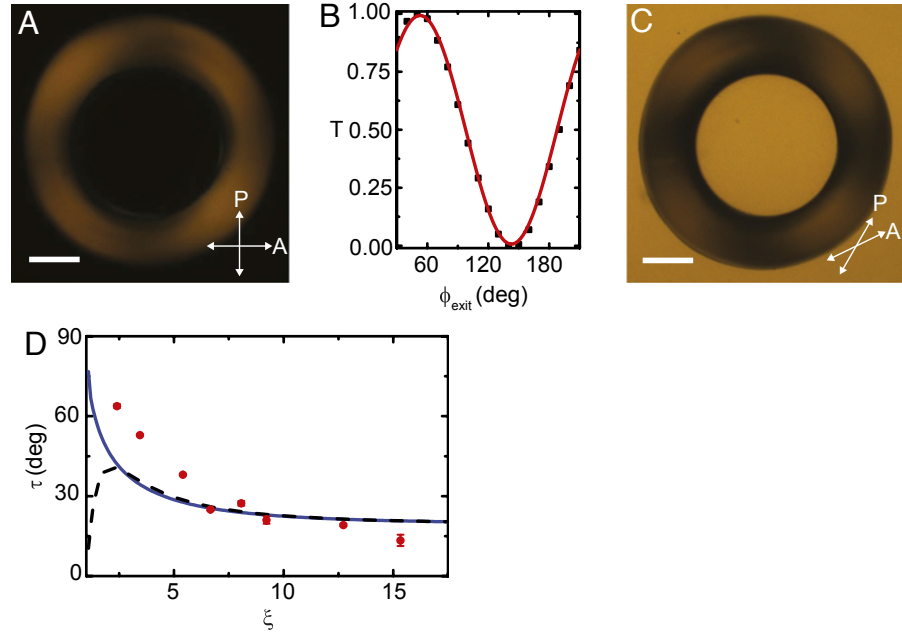
Figure 44: Determination of the twist angle and its dependence with slenderness. (A) A torus with $\xi = 3.5$ when viewed from the top and between crosspolarizers. (B) Transmission, T, as a function of the angle between the incident polarization direction and the analyzer, ϕ_{exit}. The line is a fit to the theoretical expectation in the Mauguin limit [115] with the twist angle, τ, as the only free parameter. We obtain $\tau = (52.9 \pm 0.4)°$. (C) Top view of the same torus at the minimum of the transmission curve. We measure T along the four black regions that are observed, which are darkest for the indicated direction of the polarizer and analyzer. The sense of rotation of the analyzer indicates the nematic arrangement is right-handed; this likely results from the way the torus is generated, as all tori generated in the same way have the same handedness. (D) Twist angle as a function of ξ. The dashed line represents the theoretical prediction based on eq. (156), for $K_{24} = 1.02K_2$. The solid line represents the theoretical prediction based on the improved *Ansatz* including the second variational parameter γ for the same value of K_{24}, where we have used that $K_1 = 0.64K_3$ for 5CB [40]. (Scale bar: $200\mu m$.) Ref. [77].

constant of $K_{24} = 1.02K_2$, which is slightly larger than the twist elastic constant, supporting our interpretation on the relevance of saddle-splay distortions. However, our analysis cannot exclude the possibility of a slightly smaller value of K_{24} and hence of a twisted-to-axial transition for extremely large ξ.

4.5 CONCLUSIONS

We have investigated spontaneous chiral symmetry breaking in toroidal nematic liquid crystals. As in the case of nematic tactoids [80, 101], the two ingredients for this macroscopic chirality are orientational order of achiral microscopic constituents and a curved confining boundary. This phenomenon occurs when both the aspect ratio of the toroid and $\frac{K_2 - K_{24}}{K_3}$ are small. The critical behavior of this structural transition belongs to the same universality class as the ferromagnet-paramagnet phase transition in the Ising model in dimensions above the upper critical dimension. The analogues of the magnetisation, reduced temperature and external field are the degree of twist (or surface angle), slenderness or $\frac{K_2 - K_{24}}{K_3}$, and (cholesteric) helicity in liquid crystal toroids, respectively. Critical exponents are collected in Table 1.

Liquid crystal toroid	Mean-field Ising model	Exponent
$\alpha_{eq} \sim (-\delta\xi)^\beta$	$m_{eq} \sim (-t)^\beta$	$\beta = 1/2$
$\alpha_{eq} \sim (-\delta k)^\beta$		
$\alpha_{eq} \sim q^{1/\delta}$	$m_{eq} \sim H^{1/\delta}$	$\delta = 3$

Table 1: Dictionary of the critical behavior of the structural transition in liquid crystal toroids and the thermal phase transition in the mean-field Ising model.

Thus, the helicity rather than an external field breaks the chiral symmetry explicitly. Remarkably, since an external field couples quadratically to the director field, it induces a shift of the phase boundary. An azimuthally aligned field favours the mirror symmetric director configuration, whereas a homogeneous field in the z-direction favours the doubly twisted configuration.

A minimization of the elastic energy analogous to the one presented in this article for toroidal droplets, has also been carried out for spherical droplets [112]. The analytical results reproduce qualitatively the twisted textures observed experimentally in spherical bipolar droplets [109]. In this case, detailed measurements of the dependence of the twist angle on the elastic moduli were carried out by changing temperature which in turn affects the elastic moduli. The measured exponent β was 0.75 ± 0.1 for $8\,\mathrm{CB}$ and 0.76 ± 0.1 for $8\,\mathrm{OCB}$ [47], rather than the $\frac{1}{2}$ exponent we calculated in our mean field energy minimizations that entirely neglect thermal fluctuations.

Part III

FRACTURE OF CURVED SOLIDS

In this final part we turn our attention from confined liquid crystals to geometrically frustrated solids. The curvature of two-dimensional solids which are forced to adopt a certain shape, is a source of stress. We study the effects of the stress on the fracture mechanics of such solids. We find that the curvature can both decrease or increase the critical length at which the crack starts growing depending on the location and orientation of the crack, thus both stimulating and inhibiting the onset of crack growth. Finally, the non-uniform stress generates curved crack trajectories.

5

ONSET OF CRACK GROWTH

5.1 LINEAR ELASTIC FRACTURE MECHANICS

The first and foremost one should realise when studying how things break is that fracture occurs through the propagation of one or more cracks [59]. It is exceptionally rare that materials break because a series of bonds extending from one end of the sample to the other end all break simultaneously. A real solid is not so perfect and contains flaws at which the stresses are focussed: near the tip of a crack the stresses and strains become very large. As a consequence, the material around the tip will fail and the crack will propagate. If the material behaves linear elastically, the stress tensor σ_{ij} at a distance r from the crack tip which is assumed to be small compared to the crack length a reads [8, 83, 116]

$$\sigma_{ij} = \frac{K_I}{\sqrt{2\pi r}} f_{ij}^I(\theta) + \frac{K_{II}}{\sqrt{2\pi r}} f_{ij}^{II}(\theta), \tag{178}$$

Close to the crack tip the stress is not infinite as is suggested by the inverse square root of r in eq. (178), but finite. The small region in which plastic deformations occur is called the process zone. If the radius of this zone, r_p, is small compared to the crack length – called an assumption of small scale yielding – eq. (178) describes the stresses in the annulus $r_p \ll r \ll a$ well. The sub- and super-scripts I and II in eq. (178) refer to the modes of fracture, which are displayed in Fig. 45. In two dimensions, there are two symmetry modes of fracture, namely an opening mode (traditionally labelled as mode I) and a sliding or shearing mode (traditionally labelled as mode II). For a horizontally aligned crack (*i.e.* in the x direction), in mode I vertical displacements are anti-symmetric in reflection about the x-axis ($u_y(x, -y) = -u_y(x, y)$) and horizontal displacements are symmetric ($u_x(x, -y) = u_x(x, y)$). In mode II it is the other way around: vertical displacements are symmetric ($u_y(x, -y) = u_y(x, y)$) and horizontal displacements are anti-symmetric ($u_x(x, -y) = -u_x(x, y)$). Under general loading conditions, the problem can be decomposed into these two modes.
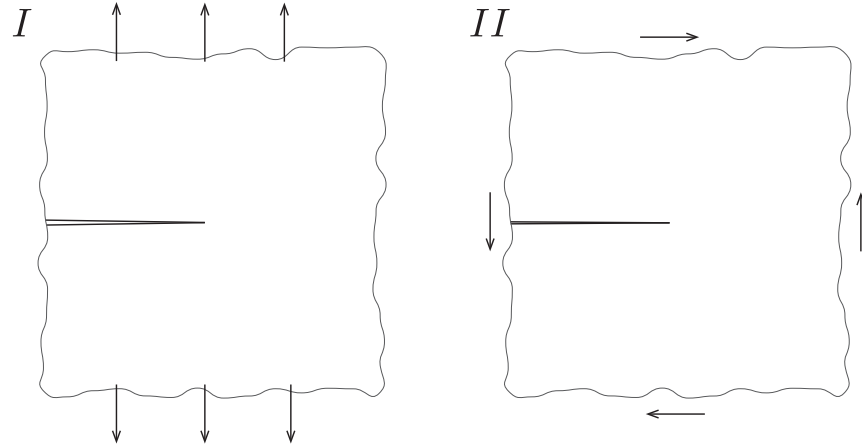
Figure 45: *Left panel:* Schematic of mode I fracture. *Right panel:* Schematic of mode II fracture.

The functions functions f_{ij}^I and f_{ij}^{II} are universal, meaning that they neither depend on loading conditions nor geometry. Thus, f_{ij}^I and f_{ij}^{II} are the same for cracks in the bulk and at the edge, for disk-shaped samples, strips, and infinite domains. They only depend on the polar angle θ (where the location of the tip is taken as the origin, see Fig. 46) and read:

$$f_{rr}^I = -\frac{1}{4}\cos\left(\frac{\theta}{2}\right) + \frac{5}{4}\cos\left(\frac{3\theta}{2}\right), \tag{179}$$

$$f_{\theta\theta}^I = \frac{3}{4}\cos\left(\frac{\theta}{2}\right) + \frac{1}{4}\cos\left(\frac{3\theta}{2}\right), \tag{180}$$

$$f_{r\theta}^I = \frac{1}{4}\sin\left(\frac{\theta}{2}\right) + \frac{1}{4}\sin\left(\frac{3\theta}{2}\right), \tag{181}$$

and

$$f_{rr}^{II} = -\frac{5}{4}\sin\left(\frac{\theta}{2}\right) + \frac{3}{4}\sin\left(\frac{3\theta}{2}\right), \tag{182}$$

$$f_{\theta\theta}^{II} = -\frac{3}{4}\sin\left(\frac{\theta}{2}\right) - \frac{3}{4}\sin\left(\frac{3\theta}{2}\right), \tag{183}$$

$$f_{r\theta}^{II} = \cos\left(\frac{\theta}{2}\right) + 3\cos\left(\frac{3\theta}{2}\right). \tag{184}$$

Eqs. (178)-(184)) follow from Williams' asymptotic analysis [110]: solving the equilibrium equations in the vicinity of the crack tip with the crack modelled as a slit with two edges that are closed in the reference state but which could open up once loading is applied. The only variables in eq. (178) which are not universal,
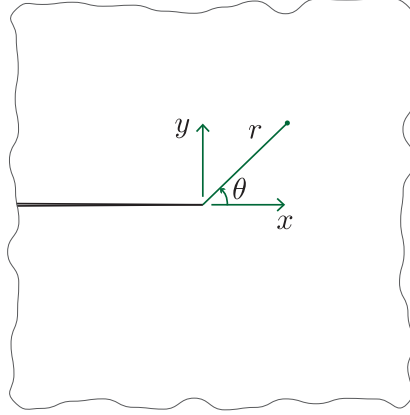
Figure 46: Schematic of the crack tip coordinates for a crack aligned in the x-direction.

are the prefactors K_I and K_{II}. These prefactors are called the stress intensity factors (of mode I and mode II, respectively), because they characterise the strength of the stress singularity. All information about loading, crack length and the shape of the sample reduce to this one quantity, thus making it one of the most important concepts in linear elastic fracture mechanics. Indeed, it is believed to determine the onset and direction of crack growth. For instance, a mode I crack will start to propagate if K_I exceeds a critical value, K_c. The critical vale for the stress intensity factor, K_c, which determines the onset of crack growth, is often referred to as the fracture toughness and it is a material property. If the crack growth is quasistatic, the growth also comes to a halt if the stress intensity factor drops below the critical value again. We call this stable crack growth. The growth is unstable if the crack continues propagating till the material fails. Several theories for mixed-mode fracture exist, of which one of them is the criterion of maximum circumferential, or hoop, stress [116]. This postulates that the pre-existing crack will grow in the direction θ_c in which $\sigma_{\theta\theta}(\theta)$ is the largest, thus satisfying

$$\frac{\partial \sigma_{\theta\theta}}{\partial \theta}|_{\theta=\theta_c} = 0, \quad \frac{\partial^2 \sigma_{\theta\theta}}{\partial \theta^2}|_{\theta=\theta_c} < 0 \tag{185}$$

Applying this criterion to eqs. (178)-(184) yields the kink angle

$$\theta_c = 2\arctan\left(\frac{-2\eta}{1 + \sqrt{1 + 8\eta^2}}\right), \tag{186}$$

where $\eta \equiv K_{II}/K_I$. A propagating crack will eventually turn its orientation such as to be in mode I and experience a maximum tensile stress. The condition for the onset of crack growth in this theory of mixed-mode fracture is that the intensity factor in the direction of maximum circumferential stress exceeds a critical value, which is assumed to be the same as for pure mode I loading:

$$\sigma_{\theta\theta}\left(\theta_c\right)\sqrt{2\pi r} > K_c. \tag{187}$$

Finally, besides crack growth criteria, the stress intensity factors also yield the shape of the crack tip opening. The displacement fields in the vicinity of the crack tip are obtained from the stress fields given by eqs. (178)-(184):

$$u_r^I = K_I \frac{1+\nu}{Y}\sqrt{\frac{r}{2\pi}}\left[\left(\frac{5}{2}-4\frac{\nu}{1+\nu}\right)\cos\left(\frac{\theta}{2}\right)-\frac{1}{2}\cos\left(\frac{3\theta}{2}\right)\right], \tag{188}$$

$$u_\theta^I = K_I \frac{1+\nu}{Y}\sqrt{\frac{r}{2\pi}}\left[-\left(\frac{7}{2}-4\frac{\nu}{1+\nu}\right)\sin\left(\frac{\theta}{2}\right)+\frac{1}{2}\sin\left(\frac{3\theta}{2}\right)\right], \tag{189}$$

and

$$u_r^{II} = K_I \frac{1+\nu}{Y}\sqrt{\frac{r}{2\pi}}\left[\left(-\frac{5}{2}-4\frac{\nu}{1+\nu}\right)\sin\left(\frac{\theta}{2}\right)+\frac{3}{2}\sin\left(\frac{3\theta}{2}\right)\right], \tag{190}$$

$$u_\theta^{II} = K_I \frac{1+\nu}{Y}\sqrt{\frac{r}{2\pi}}\left[-\left(\frac{7}{2}-4\frac{\nu}{1+\nu}\right)\cos\left(\frac{\theta}{2}\right)+\frac{3}{2}\cos\left(\frac{3\theta}{2}\right)\right], \tag{191}$$

where Y is Young's modulus and ν is Poisson's ratio. For a pure mode I crack, the vertical displacement at the crack edges (*i.e.* $\theta = \pm\pi$) reads

$$u_y\left(r,\pm\pi\right) = -u_\theta\left(r,\pm\pi\right) = \pm\frac{4K_I}{Y}\sqrt{\frac{r}{2\pi}}. \tag{192}$$

Hence, the shape of the crack tip is parabolic.

5.2 CRACKS IN A GAUSSIAN BUMP

5.2.1 *Problem formulation*

In this chapter we will study cracks in two-dimensional curved solids. Examples of two-dimensional curved solids are colloidal particles at a fluid-fluid interface, viral shells or plates, *e.g.* in aircraft

structures, where out-of plane deflection may be large compared to the plate thickness [108, 33, 117]. Besides the in-plane fracture modes introduced in the previous section, there are bending modes that we will discard in our analysis [111, 89, 33, 117]. We will focus on the effects of the in-plane stresses generated by the curvature. As pointed out by Hui et al., in curved plates the near tip stress fields will display the same singular behaviour as in eq. (178) [33, 117]. However, the values of the stress intensity factors are affected by the curvature. In turn, this influences the onset and direction of growth of pre-existing cracks.

5.2.2 *The Gaussian bump*

The surface that we will choose to study the effects of the geometric frustration on cracks is the gaussian bump (Fig. 47), whose height profile reads

$$h\left(\mathbf{x}\right) = \alpha x_0 \exp\left(-\rho^2/2\right), \tag{193}$$

where x_0 is a measure of the width of bump, $\rho = \left|\mathbf{x}\right|/x_0$ is the normalised radial coordinate, and $\alpha = h\left(0\right)/x_0$ is the aspect ratio of the bump. This surface has several convenient and interesting
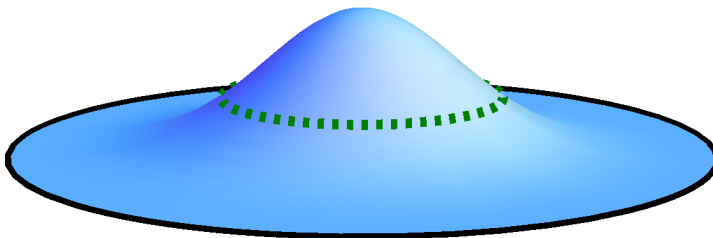

Figure 47: Schematic of a Gaussian bump. The circle $\rho = 1$, indicating the width of the bump, is drawn in dashed green. The circle $\rho = R/x_0$, which is the edge of the disk, is drawn in black.

features. First, it has a flat counterpart (unlike *e.g.* a sphere), such that one can tune α continuously from zero to a finite value. Second, it has a varying Gaussian curvature with regions of positive

and negative curvature. The curvature is positive for $\rho < 1$ and negative for $\rho > 1$. Indeed, from eq. (75) we find [107]

$$G\left(\rho\right) = \frac{\alpha^2}{x_0^2} \exp\left(-\rho^2\right) \frac{1 - \rho^2}{\left(1 + \alpha^2 \rho^2 \exp\left(-\rho^2\right)\right)^2} \tag{194}$$

$$\approx \frac{\alpha^2}{x_0^2} \exp\left(-\rho^2\right)\left(1 - \rho^2\right). \tag{195}$$

The latter approximation is valid, because we are working in the regime of small α^2. Finally, we consider the origin of the Gaussian bump to be located at the centre of the disk of radius R. If one considers samples much smaller than the width of the bump $R \ll x_0$, then $G \to \alpha^2/x_0^2$ and so the Gaussian bump reduces to a spherical cap with radius of curvature of x_0/α.

5.2.3 *Decomposing the problem*

We need to solve for the equilibrium equations of linear elasticity with an infinitely narrow cut (representing the crack) in a Gaussian bump, possibly under external loading. This external loading is usually applied at the boundary of the sample, though in principle could also be applied at the crack edges. We will decompose the problem of a crack with stress-free edges in a Gaussian bump loaded at the boundary into two other problems, called A and B. The first of these two problems is finding the stress field, $\sigma_{ij}^G\left(\mathbf{x}\right)$, prior to the introduction of the crack, due to curvature and external loading only. Next, in problem B, we solve for the stress field, $\sigma_{ij}^0\left(\mathbf{x}\right)$, for a crack whose edges are loaded, but in which there is neither curvature nor loading at the boundary of the sample. The traction, $\mathbf{p}$, applied at the crack edges is such that it cancels the tractions in the first problem, *i.e.* the traction on the top crack edge is

$$p_i = -\sigma_{ij}^G \nu_j, \tag{196}$$

with $\boldsymbol{\nu}$ the normal vector of the top crack edge, and the traction loading on the bottom crack edge is equal but opposite. Thus, the stresses generated by the curvature serve as traction on the crack edges. Superposing the stress fields in problem A with the stress fields in problem B, $\sigma_{ij}\left(\mathbf{x}\right) = \sigma_{ij}^G\left(\mathbf{x}\right) + \sigma_{ij}^0\left(\mathbf{x}\right)$, solves the initial problem (see Fig. 48). It satisfies the equilibrium equations (eq.
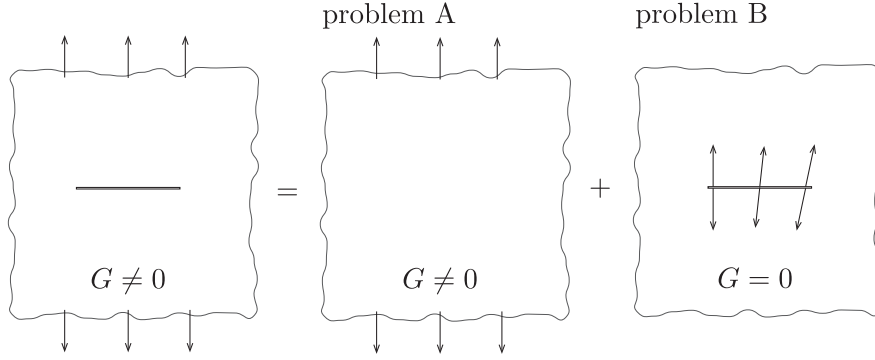
Figure 48: The solution of the problem on the left hand side of this schematic equation is obtained by superposing the stress fields in A and B. In A there is geometric frustration due to the nonzero curvature, but no crack. In B there is no curvature, but there is a crack whose edges are loaded such as to cancel the stresses generated in A at the crack location. In B, the arrows representing the forces at the crack edge are drawn non-vertical intentionally, because generally $\sigma_{xy}^G \neq 0$ and hence there could be a shear force.

(39)),

$$\partial_i \sigma_{ij} = \partial_i \sigma_{ij}^G + \partial_i \sigma_{ij}^0 = 0, \tag{197}$$

as well as the equation for the Airy stress function (eq. 75)

$$\frac{1}{Y}\partial^4 \chi = \frac{1}{Y}\partial^4 \chi^G + \frac{1}{Y}\partial^4 \chi^0 = -G. \tag{198}$$

Moreover, conditions at both the boundary of the sample and at the crack edge are correct. In the absence of any curvature, this decomposition reduces to the usual equivalence of crack face loading and far field loading. Since σ^G does not contain any singularity, the stress intensity factors of σ^0 are equal to the stress intensity factors of the full solution σ.

5.2.4 *Stress fields in the absence of cracks*

The first problem involves solving for the stresses as a result of Gaussian curvature only, prior to the introduction of the crack. Firstly, we will take the circular boundary of the disk traction-

free. For the stress components $\sigma_{\rho\rho}^G (\rho)$ and $\sigma_{\rho\phi}^G (\rho)$ evaluated at the boundary we thus have

$$p_\rho = \sigma_{\rho\rho}^G (R/x_0) = 0, \tag{199}$$

$$p_\phi = \sigma_{\rho\phi}^G (R/x_0) = 0. \tag{200}$$

Due to rotational symmetry $\sigma_{\rho\phi}^G = 0$ [107]. The trace of the stress tensor, however, reads [107]

$$\sigma_{\rho\rho}^G + \sigma_{\phi\phi}^G = \frac{\alpha^2}{4} Y \left(\frac{x_0^2}{R^2} \exp \left(-\frac{R^2}{x_0^2} \right) - \frac{x_0^2}{R^2} + \exp \left(-\rho^2 \right) \right). \tag{201}$$

From this starting point we obtain $\sigma_{\rho\rho}^G$ and $\sigma_{\phi\phi}^G$. Again, employing rotational symmetry the force-balance in the ρ direction reads

$$\rho \frac{\partial \sigma_{\rho\rho}^G}{\partial \rho} + \sigma_{\rho\rho}^G - \sigma_{\phi\phi}^G = 0. \tag{202}$$

Substituting eq. (201) to eliminate $\sigma_{\phi\phi}^G$ yields a differential equation for $\sigma_{\rho\rho}^G$ whose solution is

$$\sigma_{\rho\rho}^G = \frac{C}{\rho^2} - \frac{\alpha^2 Y}{8\rho^2} \exp \left(-\rho^2 \right) + \frac{\alpha^2 Y}{8} \frac{x_0^2}{R^2} \left[\exp \left(-\frac{R^2}{x_0^2} \right) - 1 \right]. \tag{203}$$

Demanding that the stress is finite at the origin sets the integration constant $C = Y\alpha^2/8$. We thus find

$$\sigma_{\rho\rho}^G = \frac{\alpha^2}{8} Y \left(\rho^{-2} \left[1 - \exp \left(-\rho^2 \right) \right] + \frac{x_0^2}{R^2} \left[\exp \left(-\frac{R^2}{x_0^2} \right) - 1 \right] \right), \tag{204}$$

for the radial stress component. Substituting $\sigma_{\rho\rho}^G$ back into eq. (201) yields for the azimuthal component

$$\sigma_{\phi\phi}^G = \frac{\alpha^2}{8} Y \left(\rho^{-2} \left[\exp \left(-\rho^2 \right) - 1 \right] + 2 \exp \left(-\rho^2 \right) \right.$$
$$\left. + \frac{x_0^2}{R^2} \left[\exp \left(-\frac{R^2}{x_0^2} \right) - 1 \right] \right). \tag{205}$$

These stress components are plotted as a function of ρ in Fig. 49a. If instead of traction-free boundary conditions (eqs. (199)-(200)), we apply a radial force of magnitude P,
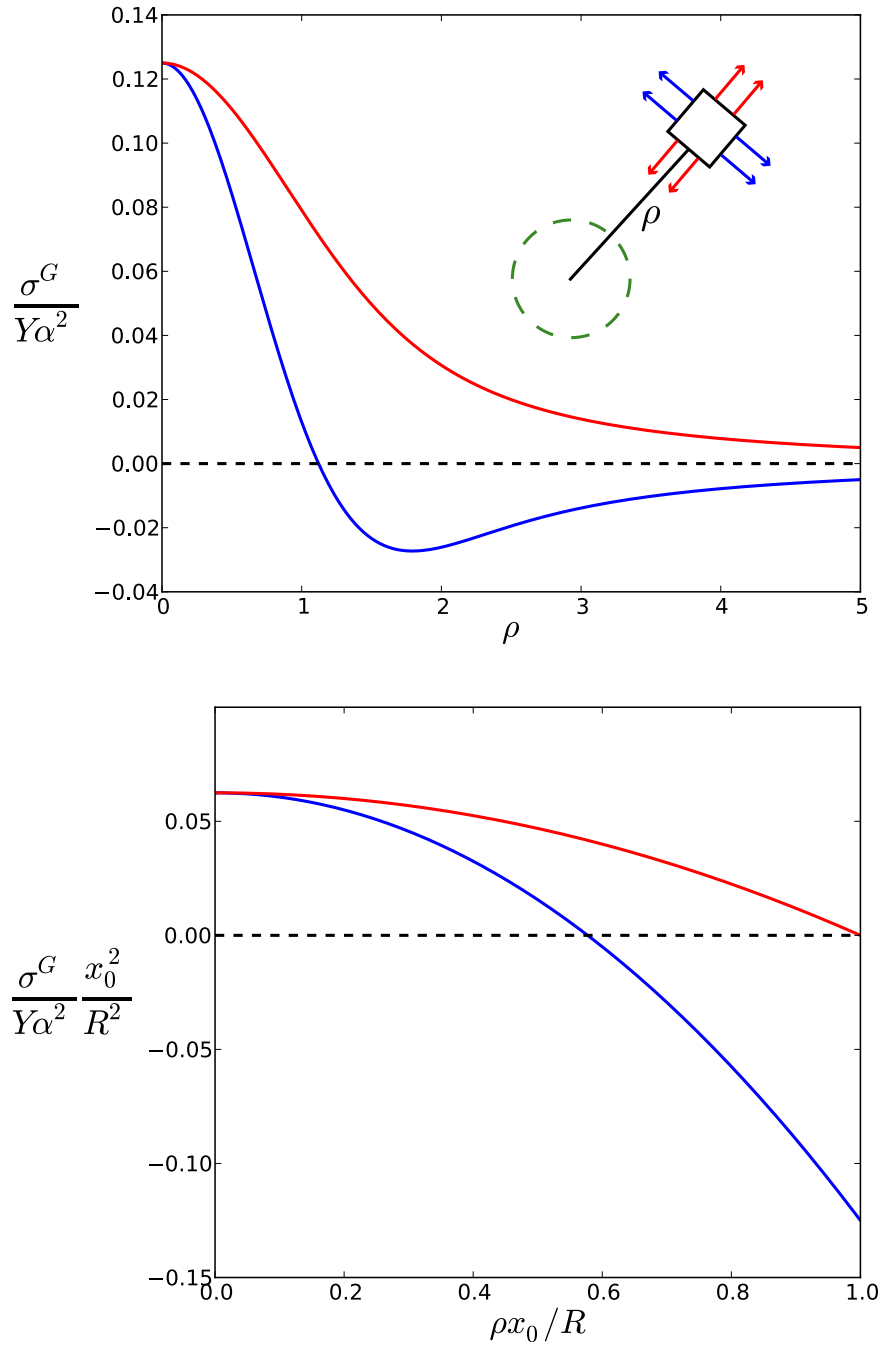
$$p_\rho = P, \tag{206}$$

$$p_\phi = 0, \tag{207}$$

Figure 49: Stress components $\sigma_{\rho\rho}^G$ (red) and $\sigma_{\phi\phi}^G$ (blue) for $P = 0$ and $R/x_0 \to \infty$ (*top panel*), $R/x_0 = 0.01$ (*bottom panel*) as a function of the rescaled radius. *Inset:* Schematic of $\sigma_{\rho\rho}^G$ and $\sigma_{\phi\phi}^G$ indicated by red and blue arrows, respectively. The bump is indicated by the green dashed circle $\rho = 1$.

we can simply superpose a uniform stress field $\sigma_{\rho\rho} = P$ and $\sigma_{\phi\phi} = P$ to the obtained expression for σ_{ij}:

$$\sigma_{\rho\rho}^G = \frac{\alpha^2}{8} Y \left(\rho^{-2} \left[1 - \exp\left(-\rho^2\right) \right] \right.$$
$$\left. + \frac{x_0^2}{R^2} \left[\exp\left(-\frac{R^2}{x_0^2}\right) - 1 \right] \right) + P, \tag{208}$$

$$\sigma_{\phi\phi}^G = \frac{\alpha^2}{8} Y \left(\rho^{-2} \left[\exp\left(-\rho^2\right) - 1 \right] + 2\exp\left(-\rho^2\right) \right.$$
$$\left. + \frac{x_0^2}{R^2} \left[\exp\left(-\frac{R^2}{x_0^2}\right) - 1 \right] \right) + P. \tag{209}$$

In an infinite medium $(R \to \infty)$, the non-vanishing stress components reduce to

$$\sigma_{rr}^G = \frac{\alpha^2}{8} Y \rho^{-2} \left(1 - \exp\left(-\rho^2\right) \right) + P, \tag{210}$$

$$\sigma_{\phi\phi}^G = \frac{\alpha^2}{8} Y \left(\rho^{-2} \left[\exp\left(-\rho^2\right) - 1 \right] + 2\exp\left(-\rho^2\right) \right) + P. \tag{211}$$

Finally, in the spherical cap regime $(R \ll x_0)$ we find (Fig. 49b)

$$\sigma_{\rho\rho}^G \approx \frac{\alpha^2}{16} Y \left(R^2/x_0^2 - \rho^2 \right) + P, \tag{212}$$

$$\sigma_{\phi\phi}^G \approx \frac{\alpha^2}{16} Y \left(R^2/x_0^2 - 3\rho^2 \right) + P. \tag{213}$$

The azimuthal stress is compressive for $|\mathbf{x}| > R/\sqrt{3} \approx 0.58R$ for $P = 0$.

5.2.5 Results for small center cracks

Now that we have solved for the stresses prior to the introduction of the crack, we can calculate the stress intensity factors by means of weight function. The stress intensity factor is an integral over the length of the crack, which we define as $2a$ for a crack in the bulk. The product of the applied traction at the crack edge with the weight function, $m(x, a)$, comprises the integrand:

$$K_I = \int_{-a}^{a} m(\xi, a) \, p_y(\xi) \, d\xi, \tag{214}$$

$$K_{II} = \int_{-a}^{a} m(\xi, a) \, p_x(\xi) \, d\xi. \tag{215}$$

The weight function can be viewed as the stress intensity factor for a force dipole at x, *i.e.* $p_y(\xi) = \delta(\xi - x)$ for mode I or $p_x(\xi) = \delta(\xi - x)$ for mode II. The weight function depends on the length of the crack, but also on the location of the applied traction and diverges at the tip. For instance, the weight function for the tip at $x = a$ of a crack in an infinite plane is

$$m(x, a) = \frac{1}{\sqrt{\pi a}} \sqrt{\frac{a + \xi}{a - \xi}}. \tag{216}$$

The stress intensity factors for such a centre crack in a Gaussian bump are thus

$$K_I = \frac{1}{\sqrt{\pi a}} \int_{-a}^{a} d\xi \sqrt{\frac{a + \xi}{a - \xi}} \, \tilde{\sigma}_{yy}^{G}(\xi, 0), \tag{217}$$

$$K_{II} = \frac{1}{\sqrt{\pi a}} \int_{-a}^{a} d\xi \sqrt{\frac{a + \xi}{a - \xi}} \, \tilde{\sigma}_{xy}^{G}(\xi, 0), \tag{218}$$

where $\tilde{\sigma}_{ij}^{G}(x, y)$ is the stress due to geometric frustration only. The origin of the xy coordinate system is at the middle of the crack.[1] If the crack size is small enough compared to the length scale over which the stresses vary, *i.e.*

$$a \left| \partial_x \tilde{\sigma}_{iy}^{G} \right| \ll \tilde{\sigma}_{iy}^{G}, \tag{219}$$

it is legitimate to take σ_{iy}^{G} out of the integrand and we obtain the following result

$$K_I = \frac{\tilde{\sigma}_{yy}^{G}(0, 0)}{\sqrt{\pi a}} \int_{-a}^{a} d\xi \, \frac{a + \xi}{\sqrt{a^2 - \xi^2}} = \sqrt{\pi a} \tilde{\sigma}_{yy}^{G}(0, 0), \tag{220}$$

$$K_{II} = \frac{\tilde{\sigma}_{xy}^{G}(0, 0)}{\sqrt{\pi a}} \int_{-a}^{a} d\xi \, \frac{a + \xi}{\sqrt{a^2 - \xi^2}} = \sqrt{\pi a} \tilde{\sigma}_{xy}^{G}(0, 0). \tag{221}$$

This result holds irrespective of the details of the shape of the surface. For a Gaussian bump with a crack that is aligned radially, eqs. (220) and (221) reduce to

$$K_I = \sqrt{\pi a} \, \sigma_{\phi\phi}^{G}(\rho^*), \tag{222}$$

$$K_{II} = 0, \tag{223}$$

---

1 The tilde is there to distinguish it from σ_{ij}^{G} which generally is a function of ρ, and thus, although it describes the same physical quantity, is a different function of its arguments.

where ρ^* is the distance to the crack from the centre of the bump. Since K_{II} the crack will grow radially if $K_I > K_c$. For the bump this implies that the critical length, a_c, at which radial cracks will grow is

$$a_c = \frac{K_c^2}{\pi \left(\sigma_{\phi\phi}^G \left(\rho^* \right) \right)^2}. \tag{224}$$

We plot this quantity in Fig. 50 for several aspect ratios of the bump in an infinite plane (*i.e.* $R \to \infty$)) and $P = 0.01Y$. We
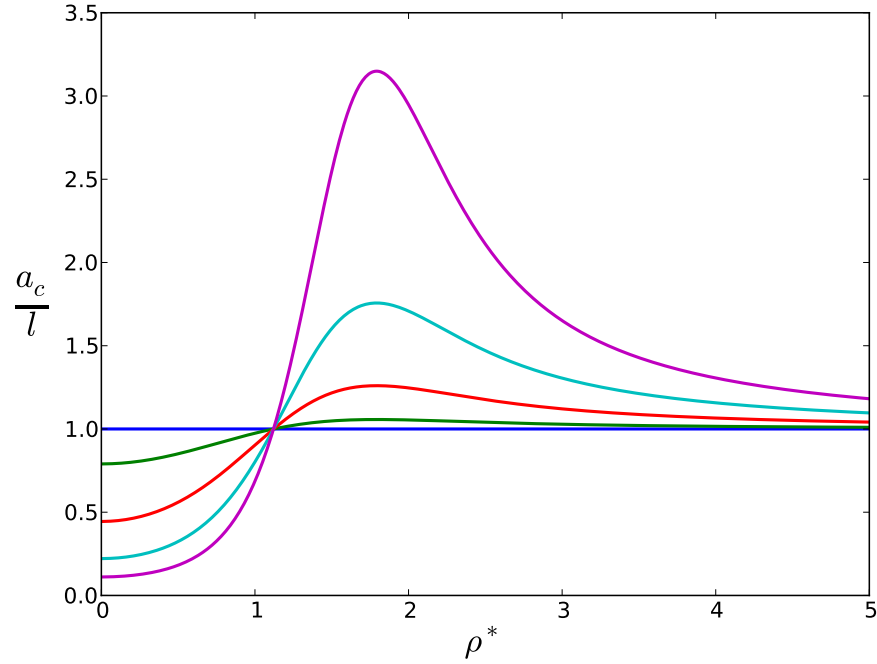

Figure 50: Normalised critical length of the small straight crack in the radial direction versus normalised radial distance of the location of the crack for $P = 0.01Y$ and aspect ratios $\alpha = 0$ (blue), $\alpha = 0.1$ (green), $\alpha = 0.2$ (red), $\alpha = 0.3$ (cyan) and $\alpha = 0.4$ (magenta).

have normalised a_c by the length, l, at which a crack under 1% strain (*i.e.* $P = 0.01Y$) would grow in the flat case (*i.e.* $\alpha = 0$). The critical size is smallest if the crack is located at the top of the bump ($\rho^* = 0$), where $\sigma_{\phi\phi}^G$ has its maximum. The critical crack length is largest at $\rho^* \approx 1.8$, where $\sigma_{\phi\phi}^G$ has its minimum. Since $\sigma_{\phi\phi}^G$ flips sign at $\rho^* \approx 1.1$, the normalised critical crack length a_c/l crosses unity for $\rho^* \approx 1.1$. For cracks located at radial distances smaller than this value, $a_c/l < 1$ and the curvature thus stimulates crack growth. On the other hand, if the crack is located sufficiently

far from the bump, $a_c/l > 1$ and the crack growth is suppressed. It should be noted that for cracks located such that we find $K_1 < 0$ (signalled by a divergence of a_c), the stress field is not given by eqs. (178)-(184)), because the crack edges would have to interpenetrate. As can be seen from eq. (192), $K_1 < 0$ would give $u_y(r, \pi) < 0$ on the top edge and $u_y(r, \pi) > 0$ on the bottom edge. In practice, crack closure or bulging occurs [8]. If α increases (or P decreases) further there will be an annular region for which this occurs.

For a small crack in the azimuthal direction rather than radial direction, we find

$$K_I = \sqrt{\pi a}\, \sigma_{\rho\rho}^G(\rho^*), \tag{225}$$
$$K_{II} = 0. \tag{226}$$

and the critical crack length is given by

$$a_c = \frac{K_c^2}{\pi \left(\sigma_{\rho\rho}^G(\rho^*)\right)^2}. \tag{227}$$

For small azimuthal cracks, the curvature suppresses the crack growth independently of the value of ρ^*, as is shown in Fig. 51, because $\sigma_{\rho\rho}^G > 0$. The critical crack length is smaller in the presence of curvature than in the absence of curvature, no matter where the azimuthal crack is located.

Next we will consider the general case in which the orientation of the crack makes an angle β with the radial direction. The traction at the crack edge reads

$$p_y \approx \tilde{\sigma}_{yy}^G(0,0) = \sigma_{\rho\rho}^G(\rho^*)\sin^2\beta + \sigma_{\phi\phi}^G(\rho^*)\cos^2\beta, \tag{228}$$
$$p_x \approx \tilde{\sigma}_{xy}^G(0,0) = \left(\sigma_{\phi\phi}^G(\rho^*) - \sigma_{\rho\rho}^G(\rho^*)\right)\sin\beta\cos\beta. \tag{229}$$

The stress intensity factors are therefore

$$K_I = \sqrt{\pi a}\left(\sigma_{\rho\rho}^G(\rho^*)\sin^2\beta + \sigma_{\phi\phi}^G(\rho^*)\cos^2\beta\right), \tag{230}$$
$$K_{II} = \sqrt{\pi a}\left(\sigma_{\phi\phi}^G(\rho^*) - \sigma_{\rho\rho}^G(\rho^*)\right)\sin\beta\cos\beta. \tag{231}$$

For the radial and azimuthal crack ($\beta = 0$ and $\beta = \pi/2$, respectively) we recover $K_{II} = 0$, and there will thus not be a kink. However, for intermediate values of α, *i.e.* $\beta \pmod{\pi/2} \neq 0$, the mode II stress intensity factor does not vanish. Therefore, if the crack does grow, it will grow in a different direction than the direction of the pre-existing crack. This kink angle can be calculated
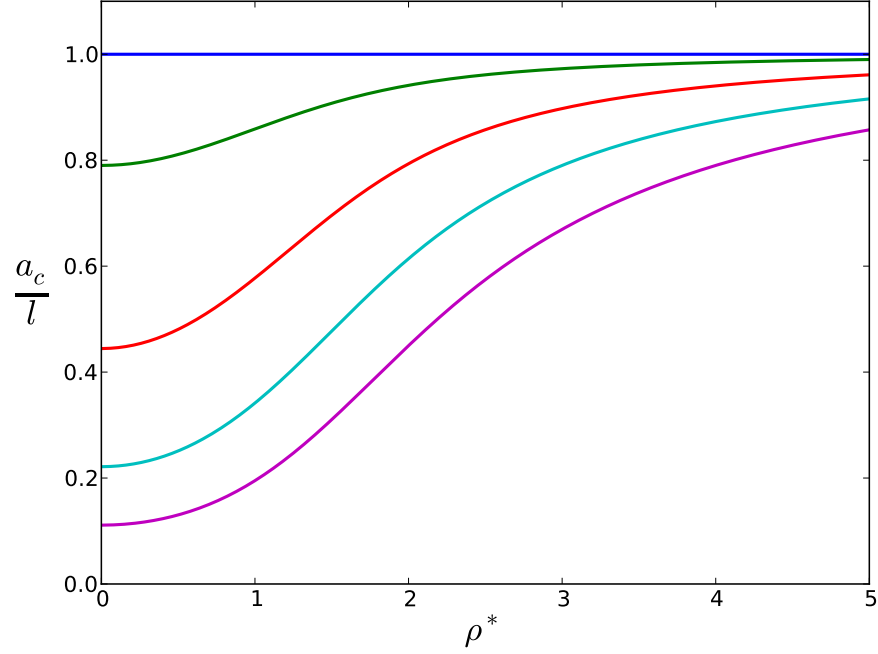
Figure 51: Normalised critical length of the small straight crack in the
azimuthal direction versus normalised radial distance of the
location of the crack for $P = 0.01Y$ and aspect ratios $\alpha = 0$
(blue), $\alpha = 0.1$ (green), $\alpha = 0.2$ (red), $\alpha = 0.3$ (cyan) and
$\alpha = 0.4$ (magenta).

with the maximum hoop stress criterium (eq. (186)) and is plot-
ted for $\beta = \pi/4$ in the top panel of Fig. 52 as a function of ρ for
several values of α. The sign of the kink angle is determined by
the sign of K_{II}. If K_{II} is positive (negative), that is, η is positive
(negative), assuming P is large enough to prevent a nonphysical
negative K_I, then θ_c is negative (positive). The sign of θ_c is inde-
pendent of the crack location, because $\sigma^G_{\rho\rho} \geq \sigma^G_{\phi\phi}$ for all ρ^*, but is
depending on the value for β, as is illustrated in the top panels of
Fig. 53 and Fig. 54 for $\rho^* = 2$ and $\rho^* = 0.5$. We find $K_{II} < 0$
(or $K_{II} > 0$) for $0 < \beta \pmod{\pi} < \frac{\pi}{2}$ (or $\frac{\pi}{2} < \beta \pmod{\pi} < \pi$)
and so $\theta_c > 0$ (or $\theta_c < 0$). For all values of β this implies that the
crack direction will be corrected toward the azimuthal direction.
The top panel of Fig. 53 also shows that the value for which the
kink angle is the largest (which is where the ratio of the mode
II and mode I stress intensity factors is the largest) occurs at a
value for β which is typically somewhat smaller than $\pi/4$. Since
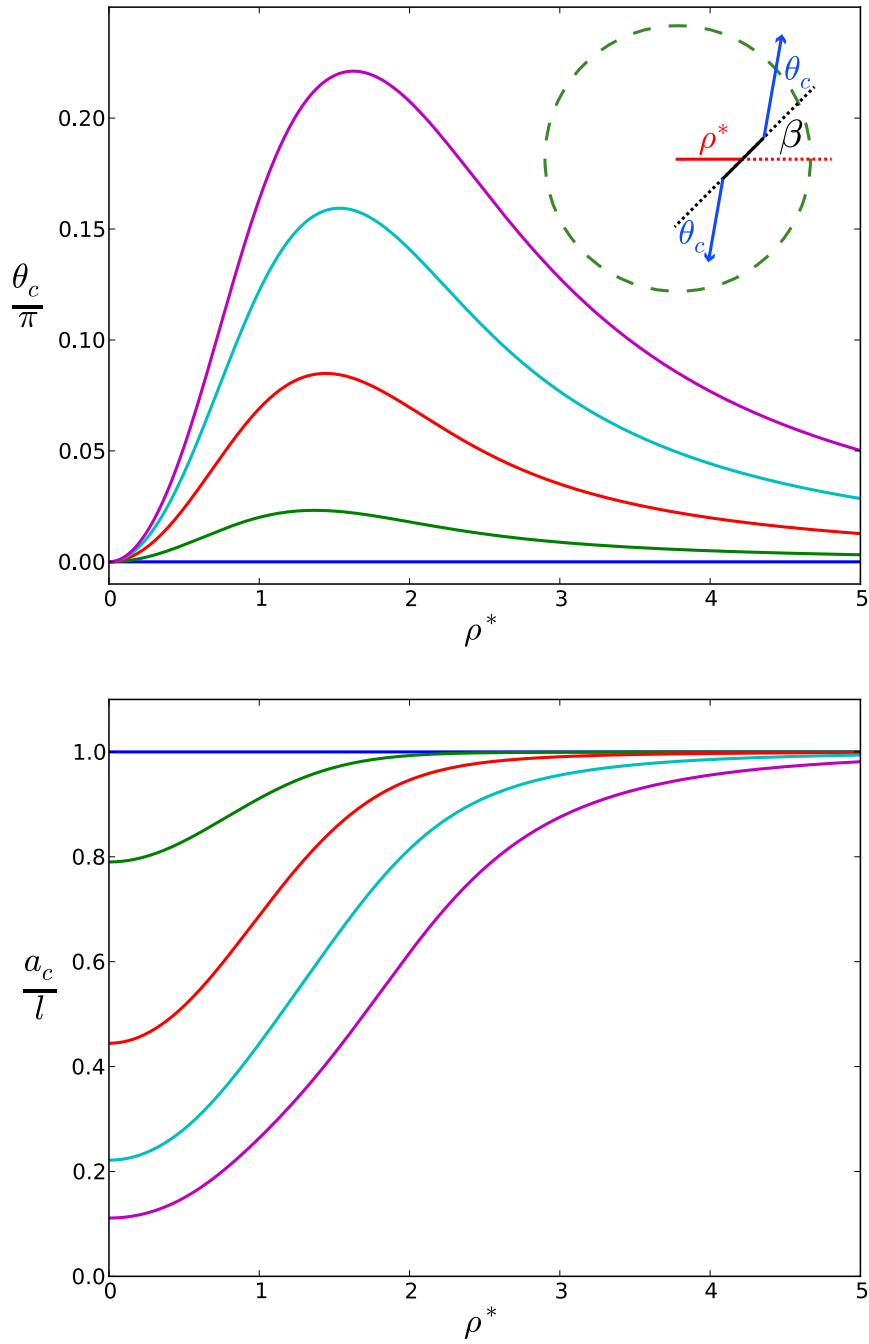the loading is mixed mode, the stress that enters in the formula

Figure 52: Kink angle (*top panel*) and normalised critical length of the small straight crack (*bottom panel*) versus normalised radial distance of the location of the crack for $\beta = \pi/4$ and $P = 0.01Y$ and aspect ratios $\alpha = 0$ (blue), $\alpha = 0.1$ (green), $\alpha = 0.2$ (red), $\alpha = 0.3$ (cyan) and $\alpha = 0.4$ (magenta). *Inset*: Schematic with graphical definitions of ρ^*, β and θ_c.
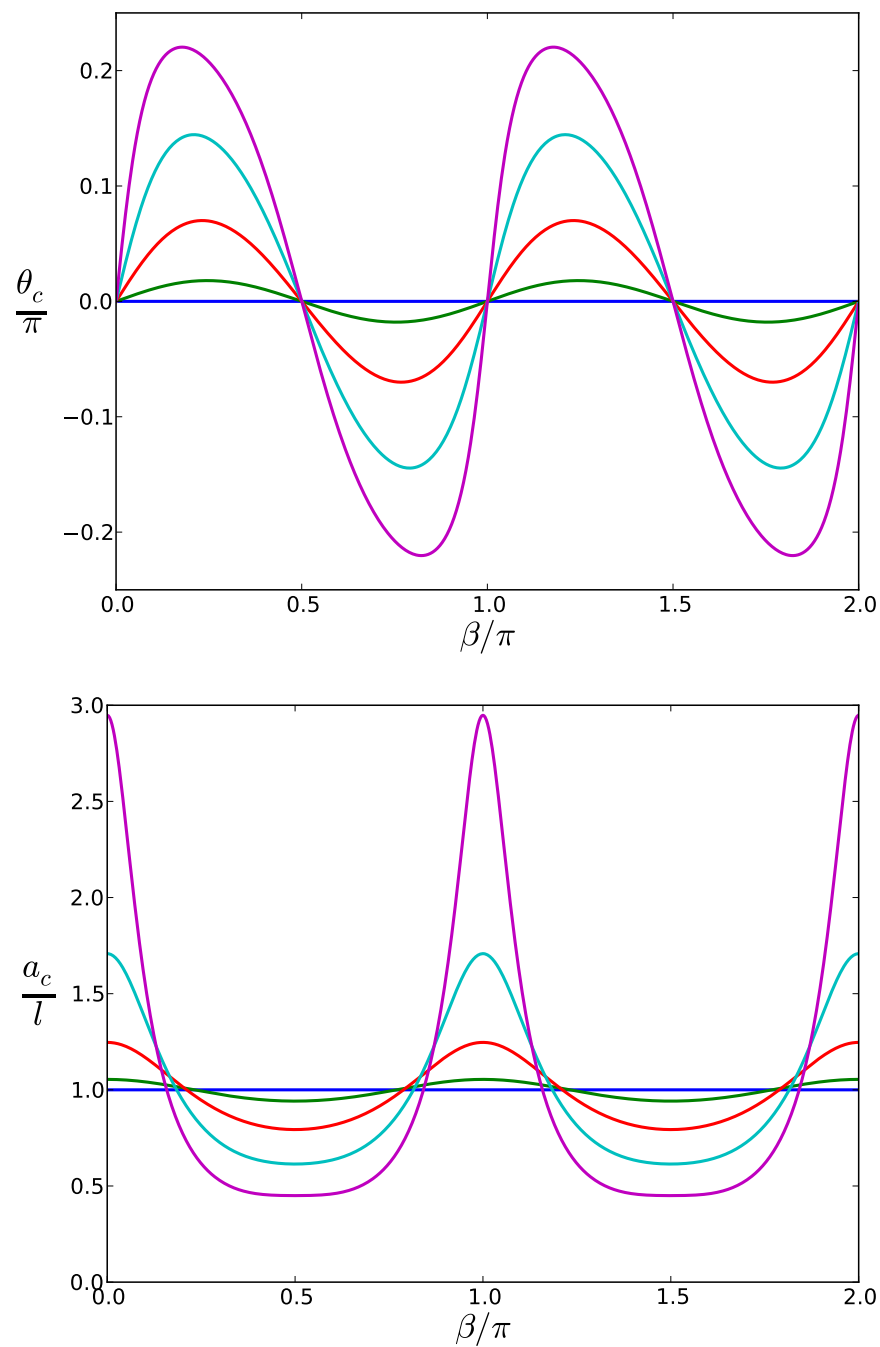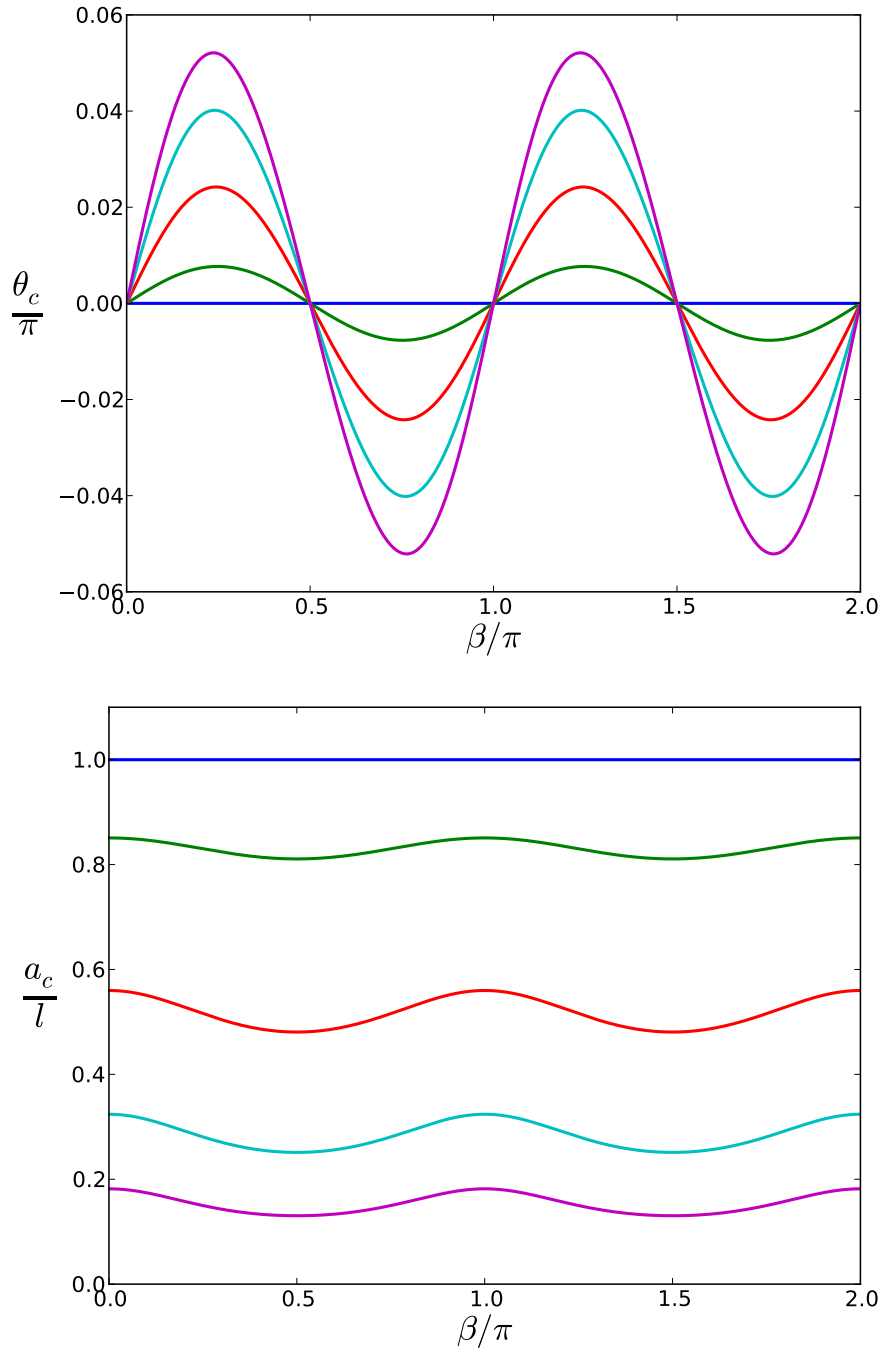
Figure 53: Kink angle (*top panel*) and normalised critical length of the small straight crack (*bottom panel*) versus the orientation of the crack for $\rho^* = 2$ and $P = 0.01Y$ and aspect ratios $\alpha = 0$ (blue), $\alpha = 0.1$ (green), $\alpha = 0.2$ (red), $\alpha = 0.3$ (cyan) and $\alpha = 0.4$ (magenta).

Figure 54: Kink angle (*top panel*) and normalised critical length of the small straight crack (*bottom panel*) versus the orientation of the crack for $\rho^* = 0.5$ and $P = 0.01Y$ and aspect ratios $\alpha = 0$ (blue), $\alpha = 0.1$ (green), $\alpha = 0.2$ (red), $\alpha = 0.3$ (cyan) and $\alpha = 0.4$ (magenta).

for the critical crack length is the circumferential stress (evaluated for $\theta = \theta_c$ in eq. (178)), and eq. (187) gives

$$a_c = \frac{K_c^2}{\pi \left(\sigma_{yy}^G \left(\rho^* \right) f_{\theta\theta}^I \left(\theta_c \right) + \sigma_{xy}^G \left(\rho^* \right) f_{\theta\theta}^{II} \left(\theta_c \right) \right)^2}. \qquad (232)$$

We again plot the critical size as a function of crack location in the bottom panel of Fig. 52, now for $\beta = \pi/4$, and as a function of β in the bottom panel of Fig. 53 for $\rho^* = 2$. The latter shows that the curvature suppresses crack growth the most when the crack is oriented radially (*i.e.* $\beta = 0,\ \pi$), and stimulates crack growth the most when the crack is aligned azimuthally (*i.e.* $\beta = \pi/2,\ 3\pi/2$). For $\rho^* \lesssim 1.1$, the curvature stimulates the crack growth irrespective of the orientation of the crack, as is shown in the bottom panel of Fig. 54 for $\rho^* = 0.5$.

5.3   CONCLUSIONS

The critical length of the crack can both be enhanced or diminished by geometry-induced stress, in contrast to uniformly applied outward force at the boundary of the disk, which always stimulates crack growth. For a radial crack in a Gaussian bump, the critcal length decreases for cracks located at distances to the top smaller than $\rho^* \approx 1.1$. For radial cracks located at $\rho^* \gtrsim 1.1$ the critical length is increased by the curvature. This effect is strongest when $\rho^* \approx 1.8$. The critical size of an azimuthally oriented crack is decreased by the curvature irrespective of position. In addition to the critical size, also the kink angle depends on the location and orientation of the crack. The pre-existing crack will start to grow in a direction with a larger azimuthal component.

CURVED CRACK PATHS

6.1 COTTERELL AND RICE THEORY

In the previous chapter, stress intensity factors and kink angles of straight cracks were obtained. To predict the trajectory of a crack, we need to calculate the the stress intensity factors and crack growth direction for curved or kinked cracks. For this we employ the perturbation theory for slightly curved cracks developed by Cotterell and Rice [15]. This theory assumes a small deviation $\lambda\left(x\right)$ of a straight crack, as is illustrated in Fig 55. Let $p_n\left(x\right)$ and
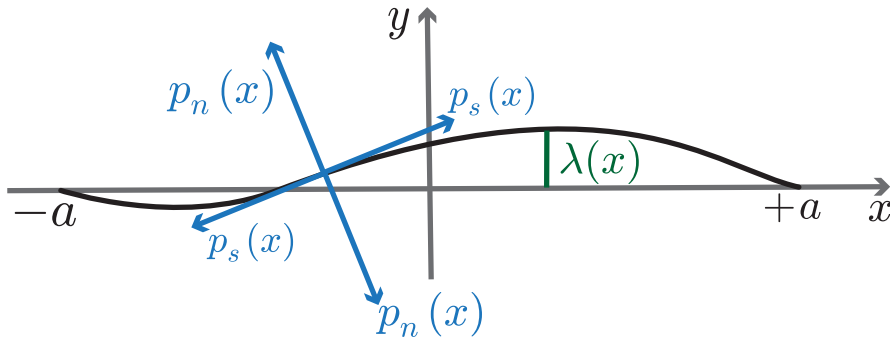
Figure 55: Schematic of a slightly curved crack with crack tips at $x = -a$ and $x = a$, including graphical definitions of $p_n\left(x\right)$, $p_s\left(x\right)$ and $\lambda\left(x\right)$.

$p_s\left(x\right)$ denote the normal and shear tractions and primes denote derivatives. The stress intensity factors at the tip at $x = a$ are approximated by [15]

$$K_I = \frac{1}{\sqrt{\pi a}} \int_{-a}^{a} \sqrt{\frac{a+\xi}{a-\xi}} \left(p_n - \frac{3}{2}\omega p_s + \lambda p'_s + 2\lambda' p_s \right) d\xi,$$

(233)

$$K_{II} = \frac{1}{\sqrt{\pi a}} \int_{-a}^{a} \sqrt{\frac{a+\xi}{a-\xi}} \left(p_s + \lambda p'_n + \frac{1}{2}\omega p_n \right) d\xi,$$

(234)

where $\omega = \lambda'\left(a\right)$ is the slope at the tip, which is (to leading order) the angle of the crack tip orientation with the x-direction. If $\lambda = 0$ these expressions reduce to eqs. (214)-(216) for straight

center cracks. For a semi-infinite crack whose (right) tip is located at $x = d$ eqs. (233) and (233) reduce to

$$K_I = \sqrt{\frac{2}{\pi}} \int_{-\infty}^{d} \sqrt{\frac{1}{d - \xi}} \left(p_n - \frac{3}{2} \omega p_s + \lambda p_s' + 2\lambda' p_s \right) d\xi,$$

(235)

$$K_{II} = \sqrt{\frac{2}{\pi}} \int_{-\infty}^{d} \sqrt{\frac{1}{d - \xi}} \left(p_s + \lambda p_n' + \frac{1}{2} \omega p_n \right) d\xi.$$

(236)

6.2 CRACK PATHS ON A GAUSSIAN BUMP

Based on the stress intensity factors in eqs. (233) and (234), we calculate the kink angle with eq. (186). Next, we grow the crack in the direction specified by the kink angle by a small increment. This process is iterated such that a series of connected line segments forms a crack path. This path approximates a smooth curved crack trajectory provided the length of the increment, Δx, is small enough. We will take $\Delta x = 0.05 x_0$ and show in Appendix D that this choice is sufficient. The only point at which the crack path is not smooth but makes a kink, is at the onset of growth of the pre-existing crack.

We will start with a straight semi-infinite crack in an elastic sheet confined to a Gaussian bump. This pre-existing crack is aligned in the x-direction and its tip is located at $d = -8 x_0$. We will vary the initial offset in the y direction, y_{off}. A uniform loading of the entire semi-infinite crack leads to an ill-posed problem, as the stress intensity factors diverge. Instead, we consider a force dipole at $x = x_p$ of magnitude $T \equiv \gamma Y x_0$ (with γ thus a dimensionless number indicating the magnitude):

$$p_n = T \delta \left(x - x_p \right),$$

(237)

$$p_s = 0.$$

(238)

We will choose $x_p = -10 x_0$, thus far away from the bump. Substituting these expressions into eqs. (235) and (236) gives a contribution to the stress intensity factors of:

$$K_I = \frac{\sqrt{2} T}{\sqrt{\pi \left(d - x_p \right)}},$$

(239)

$$K_{II} = \frac{\omega T}{\sqrt{2\pi \left(d - x_p \right)}}.$$

(240)

If the slope is positive (negative), *i.e.* the slope $\omega > 0$ ($\omega < 0$), then $K_{II} > 0$ ($K_{II} < 0$) and hence $\theta_k < 0$ ($\theta_k > 0$). Thus the external loading tries to restore the crack to a straight horizontal orientation, with $\omega = 0$.

The curvature has a distinct effect on the crack path. Numerically calculated crack paths for several values of y_{off}, $\gamma = 1$ and $\alpha = 0.5$ are presented in Fig. 56. A zoom of the crack paths around
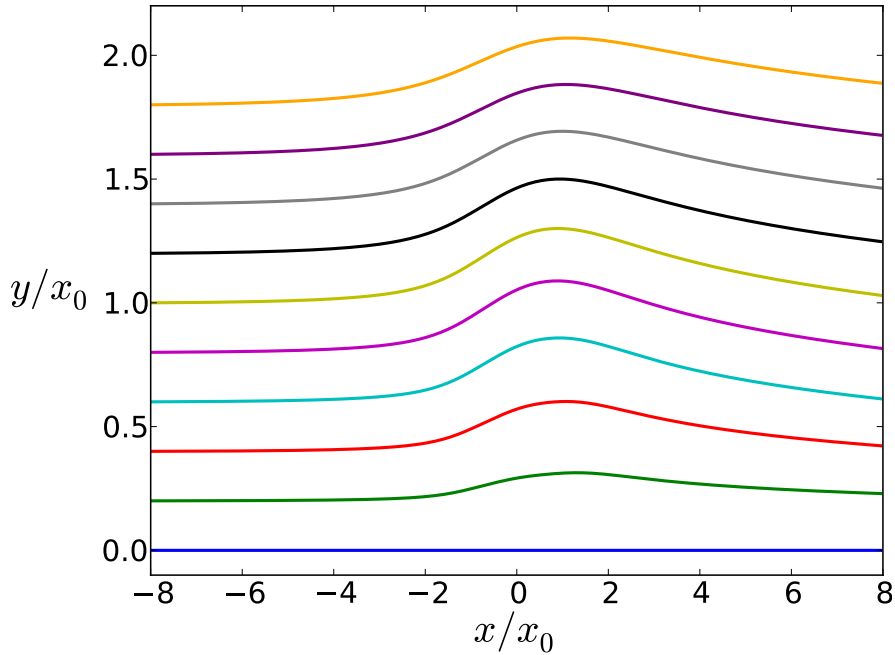

Figure 56: Crack paths for $\alpha = 0.5$ (yellow), $\gamma = 1$, and $y_{\text{off}} = 0$ (blue), $y_{\text{off}} = 0.2x_0$ (green), $y_{\text{off}} = 0.4x_0$ (red), $y_{\text{off}} = 0.6x_0$ (cyan), $y_{\text{off}} = 0.8x_0$ (magenta), $y_{\text{off}} = x_0$ (yellow), $y_{\text{off}} = 1.2x_0$ (black), $y_{\text{off}} = 1.4x_0$ (grey), $y_{\text{off}} = 1.6x_0$ (purple) and $y_{\text{off}} = 1.8x_0$ (orange).

the bump with the x and y on the same scale is shown in Fig. 57. We observe that there is a deflection as the crack approaches the bump. This is can also be inferred from the positive values of ω for negative x (Fig. 58). ω reaches its maximum at $x \approx -0.3x_0$. This corresponds to an inflection point of the crack path. Then ω crosses zero in between $x \approx x_0$ and $x \approx 1.5x_0$ depending on the value of y_{off}, the vertical deflection is maximal and the crack turns. Next is another inflection point beyond $x = 2x_0$, after which the crack eventually attains a horizontal orientation. Interestingly, the deflection is largest when y_{off} is of the order of the width of the
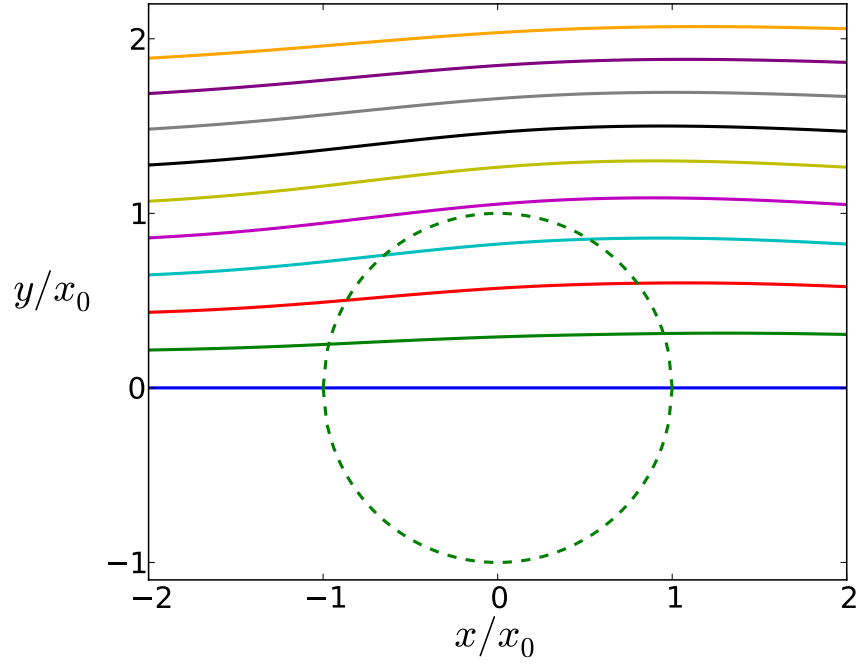
Figure 57: Crack paths for $\alpha = 0.5$ (yellow), $\gamma = 1$, and $y_{\text{off}} = 0$ (blue), $y_{\text{off}} = 0.2x_0$ (green), $y_{\text{off}} = 0.4x_0$ (red), $y_{\text{off}} = 0.6x_0$ (cyan), $y_{\text{off}} = 0.8x_0$ (magenta), $y_{\text{off}} = x_0$ (yellow), $y_{\text{off}} = 1.2x_0$ (black), $y_{\text{off}} = 1.4x_0$ (grey), $y_{\text{off}} = 1.6x_0$ (purple) and $y_{\text{off}} = 1.8x_0$ (orange). Circle $\rho = 1$ in dashed green.

bump. This can be seen from Fig. 59, where we plot the maximal y-deflection Δ as a function of y_{off}.

We can also vary the aspect ratio instead of the initial offset. The crack paths for several values of α are displayed in Fig. 60, $y_{\text{off}} = x_0$ and $\gamma = 1$. The observe that the deflection increases upon increasing the aspect ratio.

6.3 CONCLUSIONS

In conclusion, we have numerically calculated crack paths with Cotterell-Rice perturbation theory. We considered an external normal loading that tends to grow the pre-existing semi-infinite crack horizontally. The curvature-induced stresses are competing with this normal loading. The curvature is responsible for deflecting the crack path, after which it 'goes around' the bump. The magnitude of deflection increases with aspect ratio and is largest when the initial offset is around the width of the bump. Finally, when
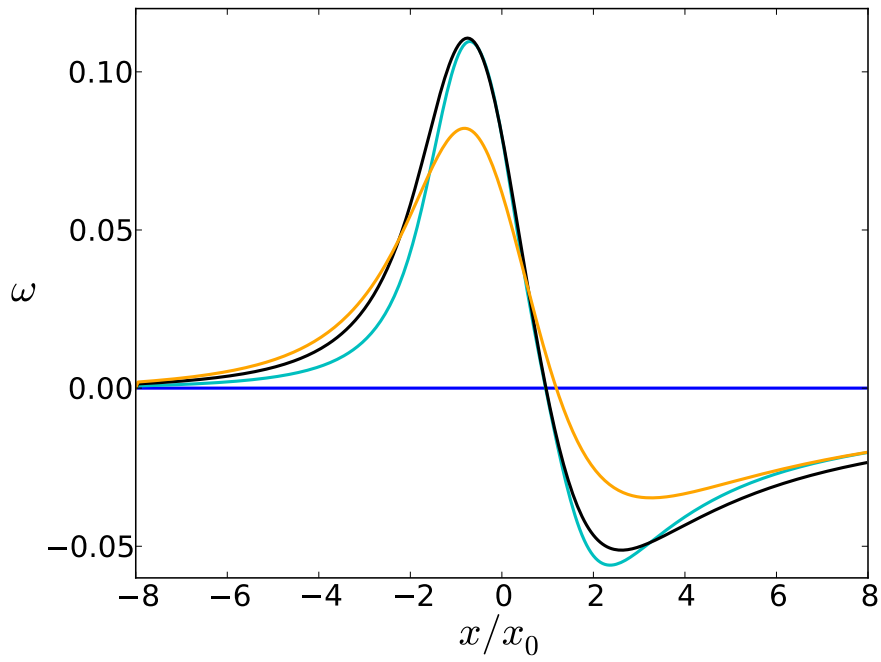
Figure 58: Crack tip angle ω for $\alpha = 0.5$ (yellow), $\gamma = 1$, and $y_{\text{off}} = 0$ (blue), $y_{\text{off}} = 0.6x_0$ (cyan), $y_{\text{off}} = 1.2x_0$ (black) and $y_{\text{off}} = 1.8x_0$ (orange).

the crack tip has past the bump, the crack turns to a horizontal orientation.
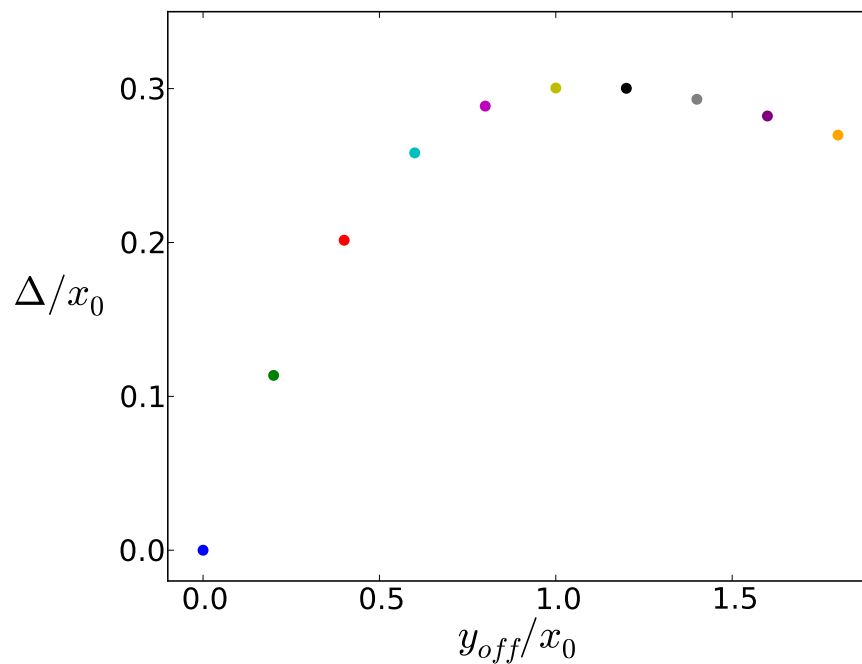
Figure 59: The maximal vertical deflection of the crack path as a function of the initial offset.
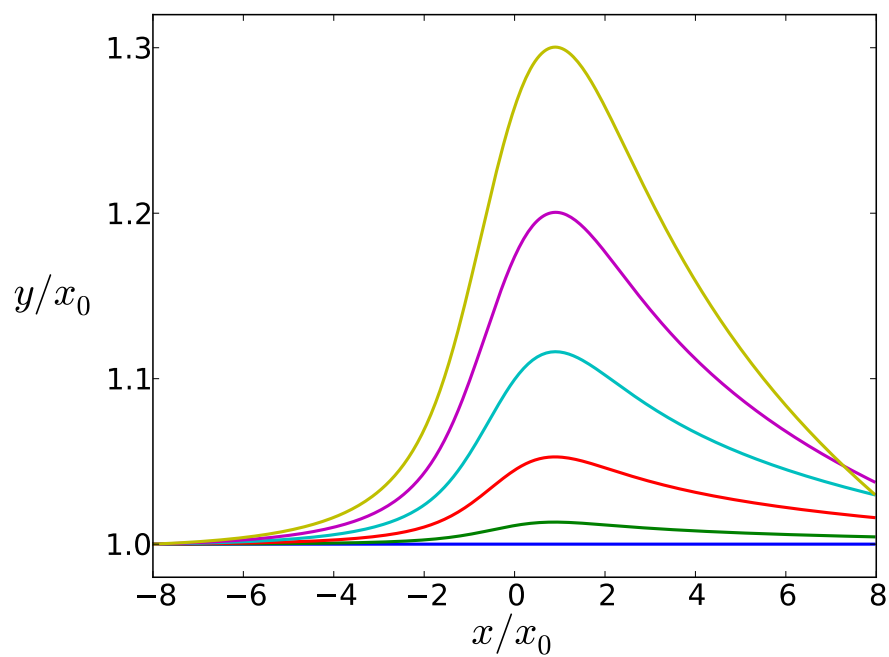

Figure 60: Crack paths for $y_{\text{off}} = x_0$, $\gamma = 1$, and $\alpha = 0$ (blue), $\alpha = 0.1$ (green), $\alpha = 0.2$ (red), $\alpha = 0.3$ (cyan), $\alpha = 0.4$ (magenta) and $\alpha = 0.5$ (yellow).

APPENDIX

ANSATZ FOR THE HOMOGENEOUS SHELL

In this appendix, we show how to arrive at eq. (110). The Euler-Lagrange equation for the angular field, $\mathbf{\Phi}$, defined as the angle of the director with a cartesian reference frame (u, v), is Laplace's equation, except at the defect cores. This equation obeys the superposition principle. Therefore, the planar director field can be written as the sum of the director fields of two individual defects, Φ_1 and Φ_2, positioned at $\mathbf{r}_1$ and $\mathbf{r}_2$. Thus we write,

$$\Phi\left(\mathbf{r}\right) = \Phi_1 + \Phi_2 = \alpha + \omega_1 + \omega_2, \tag{241}$$

where ω_i is the azimuthal angle in the reference frame that has $\mathbf{r}_i$ as its origin, as is shown in Fig. 23a. Here, α is again a global constant. If we take $\mathbf{r}_i = (u_i, 0)$ the defects lie on the u-axis. We have

$$\omega_i = \arctan\left(v, u - u_i\right), \tag{242}$$

where the two-argument $\arctan\left(y, x\right)$ is as the ordinary $\arctan\left(\frac{y}{x}\right)$, except that it takes into account in which quadrant the point (x, y) is. The resulting director field,

$$\mathbf{n} = \cos\Phi\ \hat{\mathbf{u}} + \sin\Phi\ \hat{\mathbf{v}}, \tag{243}$$

with

$$\Phi = \alpha + \sum_{i=1,2} \arctan\left(v, u - u_i\right), \tag{244}$$

is displayed in Fig. 23b for $\alpha = 0$. We rewrite this by substituting the following identities,

$$\hat{\mathbf{u}} = \cos\omega\ \hat{\boldsymbol{\rho}} - \sin\omega\ \hat{\boldsymbol{\omega}}, \tag{245}$$

$$\hat{\mathbf{v}} = \sin\omega\ \hat{\boldsymbol{\rho}} + \cos\omega\ \hat{\boldsymbol{\omega}}, \tag{246}$$

where ω and ρ are the azimuth angle and the radial distance in the uv-plane, respectively. The result reads

$$\mathbf{n} = \cos\left(\Phi - \omega\right)\hat{\boldsymbol{\rho}} + \sin\left(\Phi - \omega\right)\hat{\boldsymbol{\omega}}. \tag{247}$$

This field is projected onto a sphere by means of an inverse stereographic projection[57], illustrated in Fig. 22. Each point on the sphere is represented by a point in the plane by the following relation:

$$u + iv = 2\mathcal{R} \tan\left(\frac{\theta}{2}\right) e^{i\phi}. \tag{248}$$

Then, noting that the planar polar unit vectors, $(\hat{\boldsymbol{\rho}}, \hat{\boldsymbol{\omega}})$ are mapped to the spherical ones, $(\hat{\boldsymbol{\theta}}, \hat{\boldsymbol{\phi}})$, we find eq. (110).

CONFORMAL MAPPINGS AND THE CIRCLES OF APOLLONIUS

To obtain the director field on the sphere minimising the free energy we use the inverse stereographic projection, in eq. (248). Another example of a conformal mapping is $\psi(w)$ in eq. (115),

$$\psi(w) = \log\left(\frac{w-A}{w-B}\right), \tag{249}$$

with $-A = B = id$ and d real, to which we could associate electric potential to the real part, as this holomorphic function must obey Laplace's equation. (Note that the analogy with electrostatics made in section 3.2.2 is to aid the explanation and not unique; we could have made an analogy with two-dimensional fluid flow just as well.) This maps an 'inhomogeneous annulus', *i.e.* the area bounded by two non-concentric circles, in the complex w-plane to a vertical strip in the complex ψ-plane. Likewise, the non-concentric equipotential circles and electric field circles are mapped to vertical equipotential and horizontal electric fieldlines, as in a capacitor. It is the Möbius transformation

$$\tau(w) = \frac{w+id}{w-id}, \tag{250}$$

that maps the inhomogeneous annulus to a homogeneous one, *i.e.* the region bounded by two concentric circles. Consequently, this annulus in the complex τ plane is mapped to the vertical strip by the transformation

$$\psi = \log\tau. \tag{251}$$

The mapping is illustrated schematically in Fig. 61. The equipotential (solid black) and electric field (dashed green) lines in the w plane can thus be found by setting the real and imaginary parts of $\psi(w)$ constant:

$$\Re[\psi(w)] = \log\left|\frac{w-A}{w-B}\right| = \text{constant}, \tag{252}$$

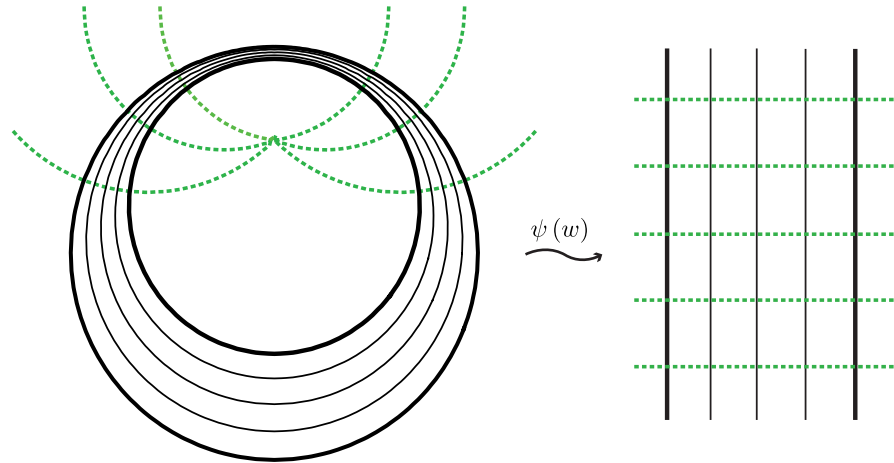$$\Im[\psi(w)] = \arg\left(\frac{w-A}{w-B}\right) = \text{constant}. \tag{253}$$

Figure 61: Schematic of the mapping of eq. (249).

Eq. (252) describes the circles of Apollonius characterised by inverse points A and B. Instead of the more familiar specification of a circle as all the points that are a radius away from a centre, eq. (252) defines a circle as the locus of points for which the ratio of the distance to A and the distance to B is constant. It is straightforward to show that eq. (252) indeed defines circles by rewriting it into

$$\frac{x^2 + (z+d)^2}{x^2 + (z-d)^2} = C, \tag{254}$$

where C is a constant. Some simple algebra now leads to the usual equation of a circle

$$x^2 + (z - \eta)^2 = \mathcal{R}^2, \tag{255}$$

with radius, $\mathcal{R}$, and displacement, η:

$$\mathcal{R} = \left[\left(\frac{1+C}{1-C} \right)^2 - 1 \right]^{\frac{1}{2}} d, \tag{256}$$

$$\eta = -\frac{1+C}{1-C} d. \tag{257}$$

A look at these eqs. yields the relation between the displacements and radii of the circles:

$$\mathcal{R}^2 = \eta^2 - d^2. \tag{258}$$

The electric field lines, which run perpendicular to the equipotential lines, are also circles. Since the argument of the product of

two complex numbers is the sum of the arguments of the individual complex numbers, we can rewrite eq. (253) as

$$\arg\left(w - A\right) - \arg\left(w - B\right) = \gamma, \tag{259}$$

In reference to Fig. 62, consider two fixed points A and B on a circle inscribing the triangle ABw, where w is a third point somewhere on the circular arc AB, then simple geometry tells us the angle AwB, called γ, is constant. Now, eq. (259) simply follows from the fact that the sum of the angles of any (Euclidean) triangle should be π. Alternatively, one can carry out the algebraic
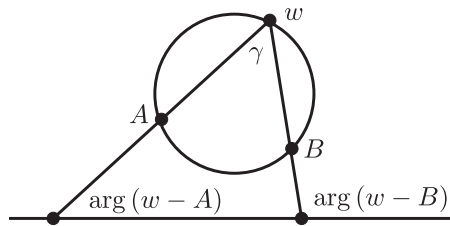
Figure 62: The electric field lines are circular arcs given by eq. (259), shown here for generic A and B.

manipulations to find that

$$\left(x - \epsilon\right)^2 + z^2 = S^2, \tag{260}$$

with radii, S, and displacements in the x-direction, ϵ, related in the following way:

$$S^2 = \epsilon^2 + d^2. \tag{261}$$

C

EXPERIMENTAL PATH THROUGH PHASE SPACE

In this appendix we derive the experimental trajectory through phase space, eq. (140), determined by a constant h_{min}. With a straightforward geometrical consideration we can relate h_{min} to Δ:

$$\frac{\Delta}{h} = 1 - \frac{h_{min}}{h}. \tag{262}$$

As mentioned in the main text, the thickness is modified by a flow of water with volume δV that passes through the shell. We take $\delta V > 0$ if the volume of the double emulsion droplet, V_{tot}, is increased and $\delta V < 0$ if it is decreased. Upon writing $\delta V = \frac{4}{3}\pi v^3$, we obtain for the radius of the double emulsion droplet

$$R^3 = R'^3 + v^3, \tag{263}$$

where R' is the radius of the double emulsion droplet before the flow of water. Since we assume that the volume of the shell, V_{shell}, is conserved, the inner radius changes similarly

$$a^3 = a'^3 + v^3. \tag{264}$$

By invoking eqs. (263) and (264) we can write for $\frac{v}{R'}$:

$$\left(\frac{v}{R'}\right)^3 = \frac{\left(1 - \frac{h}{R}\right)^3 - \left(\frac{a'}{R'}\right)^3}{1 - \left(1 - \frac{h}{R}\right)^3}. \tag{265}$$

We wish to find the path through phase space, that is, we want to write $\frac{\Delta}{h}$ as a function of $\frac{h}{R}$. We find for the displacement (eq. (262))

$$\frac{\Delta}{h} = 1 - \frac{h_{min}}{R'}\left(\frac{h}{R'}\right)^{-1}. \tag{266}$$

Now by using eqs. (263) and (264), note that

$$\frac{h}{R'} = \left[1 + \left(\frac{v}{R'}\right)^3\right]^{\frac{1}{3}} - \left[\left(\frac{a'}{R'}\right)^3 + \left(\frac{v}{R'}\right)^3\right]^{\frac{1}{3}}. \tag{267}$$

Substitution of eq. (265) into eq. (267), in turn substituted into eq. (266) yields

$$\frac{\Delta}{h} = 1 - \frac{u_0}{u} \sqrt[3]{\frac{1 - (1 - u)^3}{1 - (1 - u_0)^3}}, \tag{268}$$

where $u \equiv \frac{h}{R}$. In plotting Fig. 33, we have chosen $\frac{a'}{R'} = 1 - u_0$, with $u_0 = 0.0153$ the normalised thickness at which the shell becomes homogeneous. This is in agreement with experimental observations where the radius of the droplet is about $70 \, \mu m$ and the thickness of the order of μm then. If we draw this trajectory in the phase diagram (Fig. 32), we observe that, as we decrease thickness, it crosses from the bipolar regime to the non-bipolar regime via the regime of coexistence.

CRACK INCREMENT (IN)DEPENDENCE

In this appendix we show that $\Delta x = 0.05x_0$ is sufficiently small. The crack path does not change significantly upon reducing $\Delta x = 0.1x_0$ to $\Delta x = 0.05x_0$, as is shown in Fig. 63. This is also true for
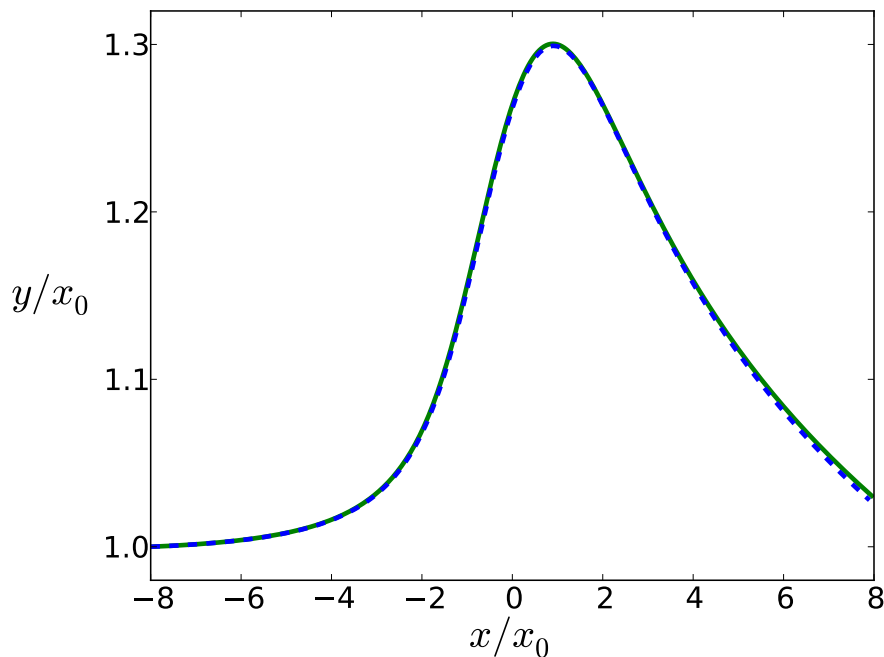

Figure 63: Crack paths for $\alpha = 0.5$, $\gamma = 1$, $y_{\text{off}} = x_0$ and $\Delta x = 0.1$ (dashed blue) and $\Delta x = 0.05$ (green).

the crack tip angle and the opening mode stress intensity factor as shown in Figs. 64 and 65 respectively. The kink angle, however, decreases upon reducing the stepsize, indicating that the crack path becomes smoother (Fig. 66). Indeed, in the limit that Δx goes to zero, θ_k should vanish. Only at the onset of growth of the pre-existing crack a kink is expected, since the loading is in mixed modes. Also K_{II} becomes smaller as we reduce Δx, and attains very small values compared to K_I (Fig. 67). Our approach is thus consistent with another criterion of smooth crack growth, namely the condition $K_{II} = 0$.
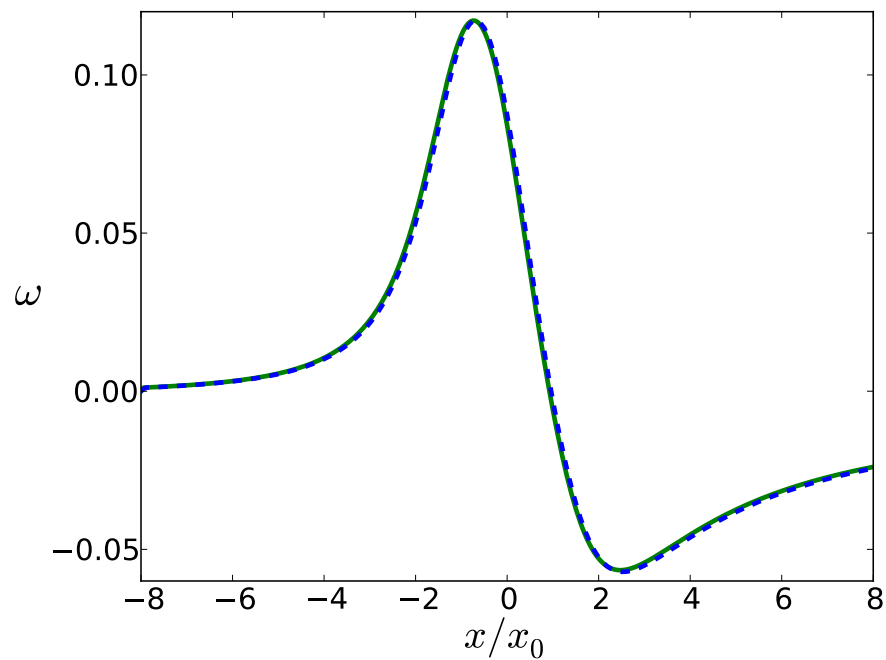
Figure 64: Crack tip angle for $\alpha = 0.5$, $\gamma = 1$, $y_{\text{off}} = x_0$ and $\Delta x = 0.1$ (dashed blue) and $\Delta x = 0.05$ (green).
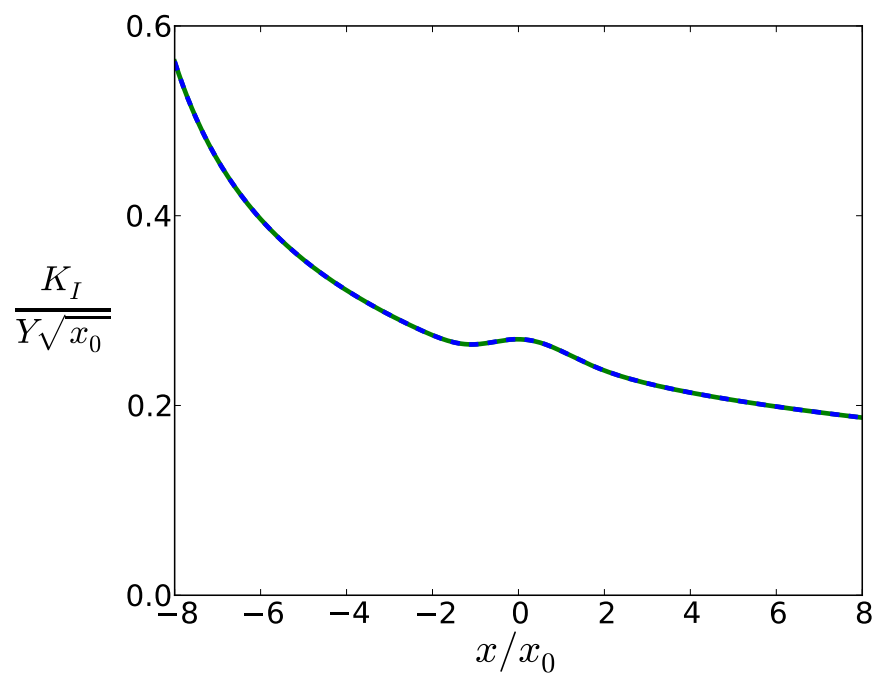

Figure 65: Opening mode stress intensity factor for $\alpha = 0.5$, $\gamma = 1$, $y_{\text{off}} = x_0$ and $\Delta x = 0.1$ (dashed blue) and $\Delta x = 0.05$ (green).
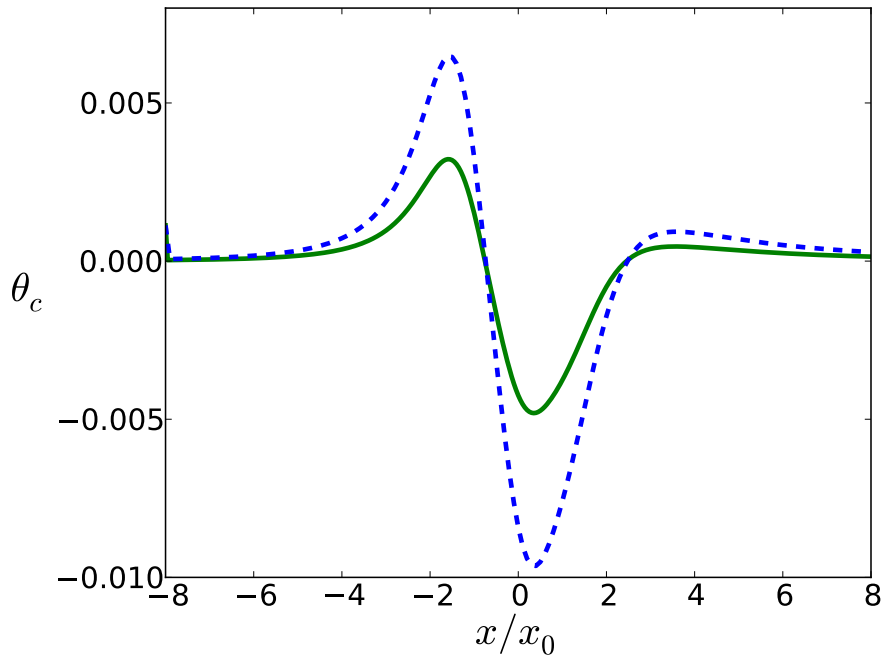
Figure 66: The kink angle for $\alpha = 0.5$, $\gamma = 1$, $y_{\text{off}} = x_0$ and $\Delta x = 0.1$ (dashed blue) and $\Delta x = 0.05$ (green).
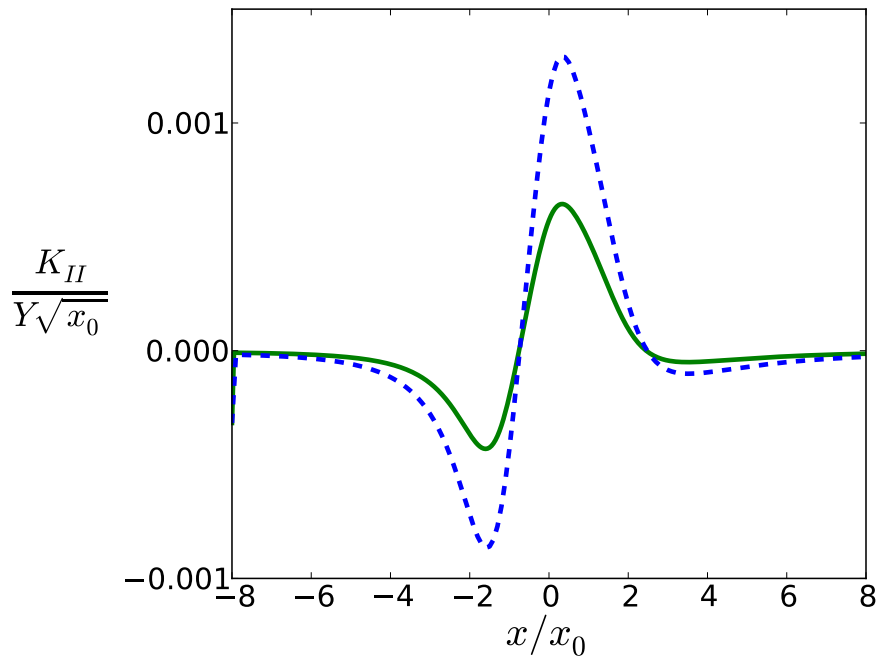

Figure 67: The mode II stress intensity factor for $\alpha = 0.5$, $\gamma = 1$, $y_{\text{off}} = x_0$ and $\Delta x = 0.1$ (dashed blue) and $\Delta x = 0.05$ (green).

BIBLIOGRAPHY

[1] http://commons.wikimedia.org/wiki/File:Latitude_lines.svg.

[2] D. W. Allender, G. P. Crawford, and J. W. Doane. Determination of the liquid-crystal surface elastic constant k_{24}. *Phys. Rev. Lett.*, 67:1442–1445, 1991.

[3] M. A. Bates. Nematic ordering and defects on the surface of a sphere: A Monte Carlo simulation study. *J. Chem. Phys.*, 128(10):104707, 2008.

[4] A. R. Bausch, M. J. Bowick, A. Cacciuto, A. D. Dinsmore, M. F. Hsu, D. R. Nelson, M. G. Nikolaides, A. Travesset, and D. A. Weitz. Grain Boundary Scars and Spherical Crystallography. *Science*, 299:1716–1718, 2003.

[5] V. A. Bloomfield. DNA condensation by multivalent cations. *Biopolymers*, 44(3):269–282, 1997.

[6] M. Bowick and L. Giomi. Two-dimensional matter: order, curvature and defects. *Advances in Physics*, 58:449–563, 2009.

[7] M. Bowick, D. R. Nelson, and A. Travesset. Curvature-induced defect unbinding in toroidal geometries. *Phys. Rev. E*, 69:041102, 2004.

[8] K. B. Broberg. *Cracks and Fracture.* Academic Press, 1999.

[9] D. L. D. Caspar and A. Klug. Physical principles in the construction of regular viruses. *Cold Spring Harbor Symposia on Quantitative Biology*, 27:1–24, 1962.

[10] M. Cavallaro Jr, M. A. Gharbi, D. A. Beller, S. Copar, Z. Shi, R. D. Kamien, S. Yang, T. Baumgart, and K. J. Stebe. Ring around the colloid. *Soft Matter*, 9:9099–9102, 2013.

[11] C. Chiccoli, I. Feruli, O. D. Lavrentovich, P. Pasini, S. V. Shiyanovskii, and C. Zannoni. Topological defects in

schlieren textures of biaxial and uniaxial nematics. *Phys. Rev. E*, 66(3):030701, 2002.

[12] P. E. Cladis and M. Kléman. Non-singular disclinations of strength s=+1 in nematics. *J. Phys. France*, 33:591–598, 1972.

[13] M. D. Contreras and R. Sanchez. Application of a factorial design to the study of the flow behavior, spreadability and transparency of a carbopol etd 2020 gel. part ii. *International Journal of Pharmaceutics*, 234(1–2):149 – 157, 2002.

[14] C. C. Conwell, I. D. Vilfan, and N. V. Hud. Controlling the size of nanoscale toroidal DNA condensates with static curvature and ionic strength. *Proceedings of the National Academy of Science*, 100:9296–9301, 2003.

[15] B. Cotterell and J. R. Rice. Slightly curved or kinked cracks. *International Journal of Fracture*, 16(2):155 –169, 1980.

[16] S. S. Datta, S.-H. Kim, J. Paulose, A. Abbaspourrad, D. R. Nelson, and D. A. Weitz. Delayed Buckling and Guided Folding of Inhomogeneous Capsules. *Phys. Rev. Lett.*, 109 (13):134302, 2012.

[17] F. David. *Statistical Mechanics of Membranes and Surfaces.* World Scientific, 2004.

[18] P. G. de Gennes and J. Prost. *The Physics of Liquid Crystals.* Oxford University Press, New York, 1993.

[19] J. Deschamps, J. P. M. Trusler, and G. Jackson. Vapor pressure and density of thermotropic liquid crystals: Mbba, 5cb, and novel fluorinated mesogens. *The Journal of Physical Chemistry B*, 112(13):3918–3926, 2008.

[20] G. A. DeVries, M. Brunnbauer, Y. Hu, A. M. Jackson, B. Long, B. T. Neltner, O. Uzun, B. H. Wunsch, and F. Stellacci. Divalent Metal Nanoparticles. *Science*, 315:358–361, 2007.

[21] A. D. Dinsmore, M. F. Hsu, M. G. Nikolaides, M. Marquez, A. R. Bausch, and D. A. Weitz. Colloidosomes: Selectively

Permeable Capsules Composed of Colloidal Particles. *Science*, 298:1006–1009, 2002.

[22] P. S. Drzaic. *Liquid crystal dispersions.* World Scientific, 1995.

[23] J. Dzubiella, M. Schmidt, and H. Löwen. Topological defects in nematic droplets of hard spherocylinders. *Phys. Rev. E*, 62:5081–5091, 2000.

[24] A. Fernández-Nieves, V. Vitelli, A. S. Utada, D. R. Link, M. Márquez, D. R. Nelson, and D. A. Weitz. Novel Defect Structures in Nematic Liquid Crystal Shells. *Phys. Rev. Lett.*, 99(15):157801, 2007.

[25] B. Fornberg. Generation of finite difference formulas on arbitrarily spaced grids. *Mathematics of Computation*, 51(184): 699–706, 1988.

[26] J. R. Frank and M. Kardar. Defects in nematic membranes can buckle into pseudospheres. *Phys. Rev. E*, 77:041705, 2008.

[27] L. Giomi and M. J. Bowick. Elastic Theory of Defects in Toroidal Crystals. *Eur. Phys. J. E*, 27:275–296, 2008.

[28] L. Giomi and M. J. Bowick. Defective ground states of toroidal crystals. *Phys. Rev. E*, 78:010601, 2008.

[29] S. C. Glotzer and M. J. Solomon. Anisotropy of building blocks and their assembly into complex structures. *Nat Mater*, 6(7):557–562, 2007.

[30] E. G. Guyon, J. Hulin, L. Petit, and C. D. Mitescu. *Physical Hydrodynamics.* Oxford University Press, New York, 2001.

[31] Y. Hatwalne and M. Muthukumar. Chiral symmetry breaking in crystals of achiral polymers. *Phys. Rev. Lett.*, 105: 107801, 2010.

[32] A. Hexemer, V. Vitelli, E. J. Kramer, and G. H. Fredrickson. Monte carlo study of crystalline order and defects on weakly curved surfaces. *Phys. Rev. E*, 76:051604, 2007.

[33] A. T. Hui, C.-Y. Zehnder and Y. K. Potdar. Williams meets von karman: Mode coupling and nonlinearity in the fracture of thin plates. *International Journal of Fracture*, 93(1-4): 409–429, 1998.

[34] W. T. M. Irvine, V. Vitelli, and P. M. Chaikin. Pleats in crystals on curved surfaces. *Nature*, 468:947–951, 2010.

[35] D. Jesenek, Š. Perutková, V. Kralj-Iglič, S. Kralj, and A. Iglič. Exocytotic fusion pore stability and topological defects in the membrane with orientational degree of ordering. *Cell Calcium*, 52(3–4):277 – 282, 2012.

[36] H. Jiang, G. Huber, R. A. Pelcovits, and T. R. Powers. Vesicle shape, molecular tilt, and the suppression of necks. *Phys. Rev. E*, 76:031908, 2007.

[37] R. D. Kamien. The geometry of soft materials: a primer. *Rev. Mod. Phys.*, 74:953–971, 2002.

[38] R. D. Kamien, D. R. Nelson, C. D. Santangelo, and V. Vitelli. Extrinsic curvature, geometric optics, and lamellar order on curved substrates. *Phys. Rev. E*, 80:051703, 2009.

[39] M. Kléman. *Points, Lines and Walls. In Liquid Crystals, Magnetic Systems and Various Ordered Media.* John Wiley & Sons Ltd., New York, 1983.

[40] M. Kléman and O. D. Lavrentovich. *Soft Matter Physics: An Introduction.* Springer-Verlag New York, Inc., 2003.

[41] V. Koning, T. Lopez-Leon, A. Fernandez-Nieves, and V. Vitelli. Bivalent defect configurations in inhomogeneous nematic shells. *Soft Matter*, 9:4993–5003, 2013.

[42] V. Koning, B. C. van Zuiden, R. D. Kamien, and V. Vitelli. Saddle-splay screening and chiral symmetry breaking in toroidal nematics. *Soft Matter*, 10:4192–4198, 2014.

[43] I. M. Kulić, D. Andrienko, and M. Deserno. Twist-bend instability for toroidal dna condensates. *EPL (Europhysics Letters)*, 67(3):418, 2004.

[44] L. D. Landau and E. M. Lifshitz. *Theory of Elasticity*, volume 7 (Course of Theoretical Physics). Reed Educational and Professional Publishing Ltd., third edition, 1986.

[45] O. D. Lavrentovich and V. M. Pergamenshchik. Stripe domain phase of a thin nematic film and the K_{13} divergence term. *Phys. Rev. Lett.*, 73:979–982, 1994.

[46] O.D. Lavrentovich and V.M. Pergamenshchik. Patterns in thin liquid crystal films and the divergence ("surfacelike") elasticity. *International Journal of Modern Physics B*, 09 (18n19):2389–2437, 1995.

[47] O.D. Lavrentovich and V.V. Sergan. Parity-breaking phase transition in tangentially anchored nematic drops. *Il Nuovo Cimento D*, 12(9):1219–1222, 1990.

[48] Amélie Leforestier and Françoise Livolant. Structure of toroidal dna collapsed inside the phage capsid. *Proceedings of the National Academy of Sciences*, 106(23):9157–9162, 2009.

[49] H.-L. Liang, S. Schymura, P. Rudquist, and J. Lagerwall. Nematic-Smectic Transition under Confinement in Liquid Crystalline Colloidal Shells. *Phys. Rev. Lett.*, 106(24): 247801, 2011.

[50] H.-L. Liang, R. Zentel, P. Rudquist, and J. Lagerwall. Towards tunable defect arrangements in smectic liquid crystal shells utilizing the nematic-smectic transition in hybrid-aligned geometries. *Soft Matter*, 8:5443–5450, 2012.

[51] H.-L. Liang, J. Noh, R. Zentel, P. Rudquist, and J. P. F. Lagerwall. Tuning the defect configurations in nematic and smectic liquid crystalline shells. *Philosophical Transactions of the Royal Society A: Mathematical, Physical and Engineering Sciences*, 371(1988), 2013.

[52] J. Lidmar, L. Mirny, and D. R. Nelson. Virus shapes and buckling transitions in spherical shells. *Phys. Rev. E*, 68: 051910, 2003.

[53] I. M. Lifshitz, A. Yu. Grosberg, and A. R. Khokhlov. Some problems of the statistical physics of polymer chains with volume interaction. *Rev. Mod. Phys.*, 50:683–713, 1978.

[54] T. Lopez-Leon and A. Fernandez-Nieves. Topological transformations in bipolar shells of nematic liquid crystals. *Phys. Rev. E*, 79:021707, 2009.

[55] T. Lopez-Leon, A. Fernandez-Nieves, M. Nobili, and C. Blanc. Nematic-Smectic Transition in Spherical Shells. *Phys. Rev. Lett.*, 106(24):247802, 2011.

[56] T. Lopez-Leon, V. Koning, K. B. S. Devaiah, V. Vitelli, and A. Fernandez-Nieves. Frustrated nematic order in spherical geometries. *Nature Physics*, 7:391–394, 2011.

[57] T. C. Lubensky and J. Prost. Orientational order and vesicle shape. *Journal de Physique II*, 2:371–382, 1992.

[58] F. C. MacKintosh and T. C. Lubensky. Orientational order, topology, and vesicle shapes. *Phys. Rev. Lett.*, 67:1169–1172, 1991.

[59] M. Marder and J. Fineberg. How things break. *Physics Today*, 49:24–29, 1996.

[60] D. Marenduzzo, E. Orlandini, A. Stasiak, D. W. Sumners, L. Tubiana, and C. Micheletti. Dna–dna interactions in bacteriophage capsids are responsible for the observed dna knotting. *Proceedings of the National Academy of Sciences*, 106 (52):22269–22274, 2009.

[61] D. Marenduzzo, C. Micheletti, E. Orlandini, and D. W. Sumners. Topological friction strongly affects viral dna ejection. *Proceedings of the National Academy of Sciences*, 110(50): 20081–20086, 2013.

[62] B. L. Mbanga, G. M. Grason, and C. D. Santangelo. Frustrated order on extrinsic geometries. *Phys. Rev. Lett.*, 108: 017801, 2012.

[63] R. Meyer. On the existence of even indexed disclinations in nematic liquid crystals. *Philosophical Magazine*, 27:405–424, 1973.

[64] R. B. Meyer. Piezoelectric effects in liquid crystals. *Phys. Rev. Lett.*, 22:918–921, 1969.

[65] M. Monastyrsky. *Riemann, Topology, and Physics*. Birkhäuser Boston, 1999.

[66] G. Napoli and L. Vergori. Surface free energies for nematic shells. *Phys. Rev. E*, 85:061701, 2012.

[67] G. Napoli and L. Vergori. Extrinsic curvature effects on nematic shells. *Phys. Rev. Lett.*, 108:207803, 2012.

[68] G. Napoli and L. Vergori. Curvature-induced ordering in cylindrical nematic shells. *International Journal of Non-Linear Mechanics*, 49(0):66 – 71, 2013.

[69] T. Needham. *Visual Complex Analysis*. Oxford University Press, 2000.

[70] D. R. Nelson. Toward a Tetravalent Chemistry of Colloids. *Nano Letters*, 2:1125–1129, 2002.

[71] D. R. Nelson and B. I. Halperin. Dislocation-mediated melting in two dimensions. *Phys. Rev. B*, 19:2457–2484, 1979.

[72] David. R. Nelson. *Defects and Geometry in Condensed Matter Physics*. Cambridge University Press, 2002.

[73] Nelson, D.R. and Peliti, L. Fluctuations in membranes with crystalline and hexatic order. *J. Phys. France*, 48(7):1085–1092, 1987.

[74] K. S. Novoselov, A. K. Geim, S. V. Morozov, D. Jiang, Y. Zhang, S. V. Dubonos, I. V. Grigorieva, and A. A. Firsov. Electric Field Effect in Atomically Thin Carbon Films. *Science*, 306:666–669, 2004.

[75] T. C. Lubensky P. M. Chaikin. *Principles of condensed matter physics*. Cambridge University Press, 1995.

[76] E. Pairam and A. Fernández-Nieves. Generation and stability of toroidal droplets in a viscous liquid. *Phys. Rev. Lett.*, 102:234501, 2009.

[77] E. Pairam, J. Vallamkondu, V. Koning, B. C. van Zuiden, P. W. Ellis, M. A. Bates, V. Vitelli, and A. Fernandez-Nieves. Stable nematic droplets with handles. *Proceedings of the National Academy of Sciences*, 110(23):9295–9300, 2013.

[78] J.-M. Park and T. C. Lubensky. Topological defects on fluctuating surfaces: General properties and the kosterlitz-thouless transition. *Phys. Rev. E*, 53:2648–2664, 1996.

[79] R. D. Polak, G. P. Crawford, B. C. Kostival, J. W. Doane, and S. Žumer. Optical determination of the saddle-splay elastic constant k_{24} in nematic liquid crystals. *Phys. Rev. E*, 49:R978–R981, 1994.

[80] P. Prinsen and P. van der Schoot. Parity breaking in nematic tactoids. *Journal of Physics: Condensed Matter*, 16(49):8835, 2004.

[81] J.-F. Sadoc and R. Mosseri. *Geometrical frustration*. Cambridge University Press, 2006.

[82] C. D. Santangelo, V. Vitelli, R. D. Kamien, and D. R. Nelson. Geometric theory of columnar phases on curved substrates. *Phys. Rev. Lett.*, 99:017801, 2007.

[83] L. I. Sedov. *Elastic and Plastic Solids and the Formation of Cracks (A Course in Continuum Mechanics, Volume 4).* Wolters-Noordhoff Publishing, 1972.

[84] R. L. Blumberg Selinger, A. Konya, A. Travesset, and J. V. Selinger. Monte carlo studies of the xy model on two-dimensional curved surfaces. *The Journal of Physical Chemistry B*, 115(48):13989–13993, 2011.

[85] H. S. Seung and D. R. Nelson. Defects in flexible membranes with crystalline order. *Phys. Rev. A*, 38:1005–1018, 1988.

[86] D. Seč, T. Lopez-Leon, M. Nobili, C. Blanc, A. Fernandez-Nieves, M. Ravnik, and S. Žumer. Defect trajectories in nematic shells: Role of elastic anisotropy and thickness heterogeneity. *Phys. Rev. E*, 86(2):020705, 2012.

[87] H. Shin and G. M. Grason. Filling the void in confined polymer nematics: Phase transitions in a minimal model of dsdna packing. *EPL (Europhysics Letters)*, 96(3):36007, 2011.

[88] H. Shin, M. J. Bowick, and X. Xing. Topological Defects in Spherical Nematics. *Phys. Rev. Lett.*, 101(3):037802, 2008.

[89] G. C. Sih, P. C. Paris, and F. Erdogan. Crack-tip, stress-intensity factors for plane extension and plate bending problems. *Journal of Applied Mechanics*, 29(2):306–312, 1962.

[90] G. Skačej and C. Zannoni. Controlling surface defect valence in colloids. *Phys. Rev. Lett.*, 100:197802, 2008.

[91] V. I. Smirnov. *A Course of Higher Mathematics*, volume III. Pergamon Press, 1964.

[92] A. Sparavigna, O. D. Lavrentovich, and A. Strigazzi. Periodic stripe domains and hybrid-alignment regime in nematic liquid crystals: Threshold analysis. *Phys. Rev. E*, 49:1344–1352, 1994.

[93] H. Stark, J. Stelzer, and R. Bernhard. Water droplets in a spherically confined nematic solvent: A numerical investigation. *European Physical Journal B*, 10:515–523, 1999.

[94] J. Stelzer and R. Bernhard. Director configurations of a nematic liquid crystal confined in a toroidal geometry. a finite element study. *arXiv:cond-mat/0012394*, 2000.

[95] M. J. Stephen and J. P. Straley. Physics of liquid crystals. *Rev. Mod. Phys.*, 46:617–704, 1974.

[96] M. Stevens. Simple Simulations of DNA Condensation. *Biophysical Journal*, 80:130–139, 2001.

[97] D. J. Struik. *Lectures on Classical Differential Geometry*. Addison Wesley Publishing Company, 1988.

[98] M. R. Stukan, V. A. Ivanov, A. Y. Grosberg, W. Paul, and K. Binder. Chain length dependence of the state diagram of a single stiff-chain macromolecule: Theory and Monte Carlo simulation. *J. Chem. Phys.*, 118:3392–3400, 2003.

[99] D. Svenšek and R. Podgornik. Confined chiral polymer nematics: Ordering and spontaneous condensation. *EPL (Europhysics Letters)*, 100:66005, 2012.

[100] S. Tie-Yan and D. Yi-Shi. Distribution of topological defects on axisymmetric surface. *Communications in Theoretical Physics*, 46(2):319, 2006.

[101] L. Tortora and O. D. Lavrentovich. Chiral symmetry breaking by spatial confinement in tactoidal droplets of lyotropic chromonic liquid crystals. *Proceedings of the National Academy of Sciences*, 108(13):5163–5168, 2011.

[102] A. M. Turner, V. Vitelli, and D. R. Nelson. Vortices on curved surfaces. *Rev. Mod. Phys.*, 82:1301–1348, 2010.

[103] A. S. Utada, E. Lorenceau, D. R. Link, P. D. Kaplan, H. A. Stone, and D. A. Weitz. Monodisperse double emulsions generated from a microcapillary device. *Science*, 308(5721): 537–541, 2005.

[104] V. Vitelli and D. R. Nelson. Defect generation and deconfinement on corrugated topographies. *Phys. Rev. E*, 70:051105, 2004.

[105] V. Vitelli and D. R. Nelson. Nematic textures in spherical shells. *Phys. Rev. E*, 74(2):021711, 2006.

[106] V. Vitelli and A. M. Turner. Anomalous coupling between topological defects and curvature. *Phys. Rev. Lett.*, 93: 215301, 2004.

[107] V. Vitelli, J. B. Lucks, and D. R. Nelson. Crystallography on curved surfaces. *Proceedings of the National Academy of Sciences*, 103(33):12323–12328, 2006.

[108] M. J. Viz, A. T. Zehnder, and J. Bamford. Fatigue fracture of thin plates under tensile and transverse shear stresses. *ASTM special technical publication*, 26(1256):631–651, 1995.

[109] G. E. Volovik and O. D. Lavrentovich. Topological dynamics of defects: boojums in nematic drops. *Sov. Phys. JETP*, 58 (6):1159–1166, 1983.

[110] M. L. Williams. On the stress distribution at the base of a stationary crack. *Journal of Applied Mechanics*, 24:109–114, 1957.

[111] M. L. Williams. The bending stress distribution at the base of a stationary crack. *Journal of Applied Mechanics*, 28(1): 78–82, 1961.

[112] R. D. Williams. Two transitions in tangentially anchored nematic droplets. *Journal of Physics A: Mathematical and General*, 19(16):3211, 1986.

[113] X. Xing, H. Shin, M. J. Bowick, Z. Yao, L. Jia, and M.-H. Li. Morphology of nematic and smectic vesicles. *Proceedings of the National Academy of Sciences*, 109(14):5202–5206, 2012.

[114] Z. Yao and M. O. de la Cruz. Packing of charged chains on toroidal geometries. *Phys. Rev. E*, 87:012603, 2013.

[115] P. Yeh and C. Gu. *Optics of Liquid Crystal Displays*. Wiley, New York, 1999.

[116] A. Zehnder. *Fracture Mechanics*. Springer, 2012.

[117] A. T. Zehnder and M. J. Viz. Fracture Mechanics of Thin Plates and Shells Under Combined Membrane, Bending, and Twisting Loads. *Applied Mechanics Reviews*, 58:37, 2005.

Dit proefschrift gaat over geometrische frustratie. Geometrische frustratie treedt op wanneer lokale orde niet door de gehele ruimte kan worden gehandhaafd. Een vaak voorkomend gevolg zijn defecten. Een vertrouwd voorbeeld van dit verschijnsel is de voetbal. Het oppervlak van de voetbal is zowel bedekt met zeshoeken, traditioneel wit gekleurd, en vijfhoeken, doorgaans zwart. Een betegeling van zeshoeken - een voorbeeld van orde - is onmogelijk op een boloppervlak - de ruimte - en andere veelhoeken - de defecten - zijn noodzakelijk. Een ander voorbeeld zijn de breedtecirkels op de aarde, die tot een punt krimpen bij de noord- en zuidpool. Die twee punten vormen de defecten en hebben elk een windingsgetal van 1. De totale som van het windingsgetal wordt bepaald door de topologie van het oppervlak.

Figuur 68: Twee vertrouwde voorbeelden van geometrische frustratie. *Links:* Geometrische frustratie in een voetbal. Een perfecte betegeling van witte zeshoeken is onmogelijk, resulterend in twaalf zwarte vijfhoeken (de defecten). *Rechts:* Geometrische frustratie op de aardbol. De breedtecirkels krimpen tot een punt bij de noord- en zuidpool (defecten). Aangepast van ref. [1].

Geometrische frustratie treedt ook op in materialen, bijvoorbeeld vloeibare kristallen. In een nematisch vloeibaar kristal wijzen de staafvormige moleculen in eenzelfde richting, **n**. Die richting

wordt de director genoemd. Idealiter wijst **n** overal dezelfde kant op. Echter, dit is soms onmogelijk als het nematisch vloeibaar kristal in een bepaalde geometrie wordt opgesloten. Zoals de naam al suggereert, is een nematisch vloeibaar kristal niet alleen geordend, maar ook vloeibaar en dus kunnen druppels van nematisch vloeibaar kristal gecreëerd worden. Ook nematische bolschillen kunnen gemaakt worden door een druppel water in te kapselen door een grotere druppel van nematisch vloeibaar kristal. De randvoorwaarden zijn zodanig dat de director zich parallel aan de grensoppervlakken wil richten.

In deel I kijken we naar de verschillende schikkingen van defecten in zulke nematische bolschillen. Dit is interessant, omdat defecten deze druppels een valentie kunnen geven en zo wellicht nieuwe structuren en materialen kunnen worden ontworpen. De defecten vormen aparte plekken op de bol, die in potentie gebruikt kunnen worden om gerichte verbindingen te bewerkstelligen, zoals dat in de natuur op atomaire schaal gebeurt. Een van de mogelijke director veldenlijnen is als de breedtecirkels, dus met twee defecten. Soortgelijke bipolaire systemen zijn al via de defecten tot een ketting aaneengeregen. Aangezien er geen onderscheid is te maken tussen **n** en −**n**, zijn defecten met een half windingsgetal ook mogelijk. In eenzelfde emulsie kunnen zowel bolschillen met een valentie van twee, drie en vier voorkomen, zodanig dat het totale windingsgetal twee bedraagt.

In hoofdstuk 2 berekenen we de energetisch meest optimale positionering van de drie afstotende defecten: dit is een gelijkbenige driehoek. De trivalente dunne bolschil is energetisch onvoordeliger dan de tetravalente dunne bolschil. De trivalente toestand is echter toch stabiel in bolschillen met een eindige dikte, door een zogenaamde 'ontsnapping in de derde dimensie' van de director veldlijnen. We berekenen deze energetische barriere en de robuustheid tegen thermische fluctuaties.

In hoofdstuk 3 concentreren we ons op de divalente bolschil. Als het gevolg van een dichtheidsverschil tussen water en het nematisch vloeibaar kristal wordt de binnenste druppel naar boven verplaatst en is de dikte van de nematische bolschil inhomogeen. De dikte en de inhomogeniteit van de dikte van de schil beïnvloeden de locatie van de defecten. We onderscheiden twee toestanden. In één van de twee toestanden zitten de defecten gevangen in het

dunste halfrond, terwijl in de andere toestand de defecten zich juist
zo ver mogelijk van elkaar vandaan bevinden. We vinden dat er
zowel continue als abrupte overgangen kunnen plaatsvinden tus-
sen deze twee toestanden als de dikte van de bolschil en diens
inhomogeniteit veranderen.

In hoofdstuk 4 (deel II) beschouwen we nematische druppels in
de vorm van een torus in plaats van een bol. De druppel kan deze
ongebruikelijke vorm behouden door speciale eigenschappen van
het dispersiemiddel. De topologie van het grensoppervlak vereist
geen defecten. We ontdekken echter wel een twist in het director-
veld ten gevolge van de opsluiting van het nematisch vloeibaar
kristal in deze vorm boven een kritische waarde van de dikte van
de torus. Dit directorveld is bovendien chiraal. Er zijn twee energe-
tische minima die elkanders spiegelbeeld zijn. Deze spontane chi-
raliteit wordt verklaard door twee elastische effecten. Ten eerste is
twist voordeliger dan buiging van de director. Ten tweede ontdek-
ten we dat een andere elastische vervorming, namelijk een elasti-
sche vervorming op de rand genaamd zadelspreiding, de director
koppelt aan de excentrieke kromming van het grensvlak en daar-
mee bijdraagt aan een chirale toestand mits de corresponderende
elastische constante positief is. Een extern veld breekt de spiegel-
symmetrie niet expliciet, maar verschuift de kritische waarde van
de dikte waarop de overgang plaatsvindt tussen de chirale and
symmetrische toestand. Een moleculaire chiraliteit breekt de sym-
metrie wel expliciet.

In deel III beschouwen we de invloed van geometrische frustra-
tie op scheurgroei. Als een elastische film wordt geforceerd een
bepaalde vorm aan te nemen, zoals bijvoorbeeld een (Gaussische)
bult, dan leidt de kromming van de film tot rek in het materiaal.
Deze spanning heeft effect op de scheurgroei. Rondom de scheurtip
is er een verhoogde spanning, die gekarakteriseerd wordt door twee
spanningsintensiteitsfactoren. Als de spanningsintensiteitsfactor in
de richting van maximale trekspanning boven een kritische waarde,
de scheurgroeiweerstand, uitkomt begint de scheur te groeien, met
mogelijk gevolg dat het materiaal breekt. De richting van scheur-
groei hangt ook van de twee spanningsintensiteitsfactoren af. Aan-
gezien de spanningsintensiteitsfactoren toenemen met de lengte
van de scheur, is er een kritische lengte waarop de scheur begint
met groeien. In hoofdstuk 5 berekenen we die kritische lengte voor

scheuren in gekromde platen. Deze lengte is een functie van de loca-
tie en oriëntatie van de scheur. Voor scheuren in de richting van de
azimut leidt de kromming tot een verlaging van de kritische lengte
ongeacht de locatie. Voor radieel (ten opzichte van de bump) georiën-
teerde scheuren leidt de kromming ook tot een verlaging van de
kritische lengte als de scheur zich binnen een bepaalde straal tot
de top van de bump begeeft, maar een verhoging van de kritische
lengte als de scheur zich daarbuiten bevindt. De grootte van de
straal is grofweg de breedte van de bump. Ook de hoek tussen de
oriëntatie van de scheur en de richting waarin deze groeit is afhan-
kelijk van de locatie en orientatie van de scheur. In hoofdstuk 6
berekenen we numeriek het gehele pad dat een aanvankelijk rechte
semi-oneindige scheur aflegt. Dit doen we met behulp van storings-
rekening voor licht gekromde scheuren ontwikkeld door Cotterell
en Rice. Deze afbuiging is het grootst als de scheur aankomt ter
hoogte van de breedte van de bump.

CURRICULUM VITAE

I was born on 4 March 1988 in Lisserbroek. After graduating from Het Rijnlands Lyceum Sassenheim, I started my BSc studies in Physics in Leiden at the age of seventeen. I obtained my degree three years later in 2008. Besides the regular courses I completed an interdisciplinary honours programme on solar biofuels. I spent half a year on experimental and computational research on light harvesting complexes in photosynthetic bacteria under the guidance of prof. dr. S. Völker and the late prof. dr. R. Silbey (MIT).

In the next two years, I concentrated on theoretical physics. This included a one-year research project on liquid crystal emulsions at the Instituut Lorentz with dr. Vitelli and in close collaboration with the experimental group of prof. dr. A. Fernandez-Nieves at the Georgia Institute of Technology. In 2010, I obtained my MSc degree in physics cum laude, also from Leiden University.

In November 2010, I continued working with dr. Vitelli as a PhD researcher. A large part of the results are collected in this thesis. I stayed twice at the University of Chicago (in March 2011 and August 2013) as part of a collaboration with prof. dr. W. T. M. Irvine. I have presented my work on fourteen occasions at national and international conferences, schools and seminars in France (Les Houches), England (Cambridge), Belgium (Leuven), Portugal (Lisbon), the USA (Chicago, Dallas, Biddeford) and the Netherlands. At FYSICA 2014, the annual conference of the Nederlandse Natuurkundige Vereniging, I was elected as best plenary young speaker by an audience of over 500 people. In this year, I also won the Belgian equivalent of this young speaker contest.

Throughout my PhD and MSc studies I have assisted in teaching the courses Statistical physics (fall 2011, 2012 and 2013), Quantum Mechanica II (spring 2010 and 2011), Klassieke mechanica II (fall 2009), Klassieke mechanica I (spring 2009) and Wiskunde Aansluiting (fall 2008). During my BSc studies I have also been employed as a tutor to a group of first-year students in the academic years 2006-2007 and 2007-2008.

PUBLICATIONS

- T. Lopez-Leon, **V. Koning**, K. B. S. Devaiah, V. Vitelli, A. Fernandez-Nieves
  Frustrated nematic order in spherical geometries,
  Nature Physics 7, 391-394 (2011) [Chapters 2 and 3]

- **V. Koning**, T. Lopez-Leon, A. Fernandez-Nieves, V. Vitelli
  Bivalent defect configurations in inhomogeneous nematic shells,
  Soft matter 9, 4993-5003 (2013); arXiv:1211.4622
  [Chapter 3]

- E. Pairam, J. Vallamkondu, **V. Koning**, B.C. van Zuiden,
  P.W. Ellis, M.A. Bates, V. Vitelli, A. Fernandez-Nieves
  Stable nematic droplets with handles,
  Proceedings of the National Academy of Sciences 110, 9295-9300 (2013); arXiv:1212.1771 [Chapter 4]

- **V. Koning**, B.C. van Zuiden, R.D. Kamien, V. Vitelli
  Saddle-splay screening and chiral symmetry breaking in toroidal nematics,
  Soft Matter 10, 4192-4198 (2014); arXiv:1312.5092
  [Chapter 4]

- **V. Koning**, V. Vitelli
  Crystals and liquid crystals confined to curved geometries,
  Accepted as chapter in *Fluids, colloids and soft materials: An introduction to soft matter physics*, edited by A. Fernandez-Nieves; arXiv:1401.4957 [Chapter 1]

- **V. Koning**
  Spontaneous chirality in liquid crystal droplets,
  Submitted

ACKNOWLEDGEMENTS

vriendschap, alle liedjes die je mij hebt laten beluisteren en alle tennislessen die je me hebt gegeven. Papa, mama, dank jullie wel voor alle aanmoedigingen om te (blijven) leren. Zonder dat zou ik nooit in staat zijn geweest om zelfs maar aan dit boekje te beginnen. Lil one, you have transformed my life by taking me on adventures through the tallest mountains, to new cities, and to other places previously unknown to me. I admire your courage and your strength, and I treasure the love that you give me every day.